ON-THE-GO SOIL PHYSICAL PROPERTIES CHARACTERIZATION USING ACOUSTIC EMISSION DETECTION

BY

BRENDAN MATTHEW KUHNS

THESIS

Submitted in partial fulfillment of the requirements
for the degree of Master of Science in Technical Systems Management
in the Graduate College of the
University of Illinois at Urbana-Champaign, 2019

Urbana, Illinois

Adviser:

Associate Professor Tony E. Grift

Abstract

Soil physical properties are a foundational classification of measurements with direct relation to the productivity of agricultural soils. Currently, measurements of these properties are either crudely taken in field or low volumes are meticulously characterized in laboratory settings at high costs. This work outlines the development of a novel system for on-the-go characterization of soil physical properties. The system utilizes a piezoelectric acoustic emission sensor with a voltage output, embedded in a wedge which measures the interaction at the soil-wedge interface. Experiments took place in the field and in indoor and outdoor soil bins. Effects of the speed of the implement, compaction, and texture were analyzed using voltage vs. time series and frequency spectra. A linear relationship was found between the speed of the implement and the sensor output with a coefficient of determination R^2 of 0.79. Measurements taken in a high compaction soil were compared to those taken in a soil with low compaction. A difference in the population median signal energy was found at an α of 0.01. Four soil textures were sampled and their frequency spectra analyzed to determine a correlation between the soil texture and its corresponding frequency spectrum. Analytical techniques included the Welch's power spectral density estimate, wavelet analysis, and moving average Fourier transforms. Principal component analysis using the z-score normalization of the Welch distribution allowed for separation of the frequency spectra given the texture. High levels of self-similarity between replications were seen in sands and moderate levels in loam. An analysis of variance using the Welch correction was performed and subsequent post-hoc evaluation using the Games-Howell method was completed. The results show that at an α of 0.05 all textures are separable with respect to each other texture. Future work should investigate effects of other soil properties on the acoustic signature and include development of machine learning approaches to classify soils based on these data.

Acknowledgements

First I would like to thank my parents, Terry and Meegan, my Grandparents, Gerry, Mary, Gary, and Karen, and fiancé Jordan for their unwavering support of my educational journey which resulted in this thesis. I would like to thank my advisor Dr. Tony Grift for his complete support and technical guidance. Dr. Henrique Reis, Dr. Carmen Ugarte, Mr. Timothy Lecher, and Mr. Jacob Niehaus also deserve my gratitude for acting as amazing resources during this work. This research was funded in part by a USDA National Institute of Food and Agriculture Food Security Program grant, award number 2016-68004-24769. This publication also contains data produced under an Energy-Biosciences-Institute funded award.

Table of Contents

List of Abbreviations

AE – Acoustic emission

AECI – Acoustic emission counts index

AESW – Acoustic emission sensing wedge

ASABE – American Society of Agricultural and Biological Engineers

ANN – Artificial neural network

ANOVA – Analysis of variance

ASTM – American Society for Testing and Materials

BF – Brown and Forsythe

CI – Cone index

CP – Cone penetrometer

DAQ – Data acquisition unit

dB – Decibel

FFT – Fast Fourier transform

GPS – Global Positioning System

GUI – Graphical user interface

HHT – Hilbert Huang transform

HRI – Horizontal resistance index

LVDT – Linear variable differential transformer

mph – Miles per hour

NRCS – Natural Resource Conservation Service

PC – Principal component

PCA – Principal component analysis

PSD – Power spectral density

PSI – Pounds per square inch

RMS – Root mean square

SNR – Signal-to-noise ratio

SOM – Soil organic matter

TDR – Time domain reflectometry

USDA – United States Department of Agriculture

UNFAO – United Nations Food and Agriculture Organization

VWC – Volumetric water content

VDC – Volts direct current

Chapter 1 : Introduction

1.1 Overview

According to the United Nations Food and Agriculture Organization (UNFAO), to meet the growing world's demand for food farmers will need to increase cereal grain production by 3 billion tonnes by 2050 (United Nations Food and Agriculture Organization, 2009). Along with the need for increased production, the UNFAO report on the world's soil resources concludes that the world's food production capacity is severely threatened by soil degradation. The degradation is linked to many specific threats such as erosion, organic matter decline, and compaction. However, despite previous mismanagement, some soils may have their production capacity regenerated through restorative and sustainable management practices. Increased understanding of the chemical, biological, and physical properties of the soil are imperative to further develop these management practices and achieve sustainability (UNFAO, 2015).

Although there are many important soil physical properties, soil compaction and texture are key factors in agronomic decision making. Soil texture refers to the quantity of soil separates which comprise the mineral component of the soil. These separates are denoted in three size classes: sand, silt, and clay. The percent composition of the particle size is commonly referred to as the classification of the soil and is graphically displayed in the texture triangle (García-gaines & Frankenstein, 2015). Soil compaction is a process by which air is removed from the soil during the application of mechanical energy. The degree of compaction is commonly expressed as the proportion of the mass of the soil to its relative volume (Das & Sobhan, 2009). Soil texture and compaction have a direct impact on water holding capacity, water mobility, tilth, and overall fertility (Brady & Weil, 2004). Soil texture and compaction can be measured in the field (often manually) and in a laboratory setting. Both measurement types are costly and labor intensive. The

in-field measurements are also inaccurate and it is impractical to collect large samples sizes for laboratory measurements. Most importantly however, neither measurement techniques provide a truly site-specific map of a given field. Samples are generally taken on an acre scale and maps are made through extrapolation (Dinkins et al., 2017). Management decisions derived from these maps do not provide enough information to recommend a truly optimal management plan.

To alleviate the current lack of site-specific measurement and promote intergenerational sustainability of our soils, a sensing system was developed allowing in-field site-specific measurement of soil compaction and texture. The system was comprised of a tillage tool-like implement which housed an acoustic emission sensor. The sensor takes readings of waveforms caused by the interaction of soil against the submerged working surface of the tillage implement. This thesis describes the design, development, and validation/testing of the device.

1.2 Justification of Research

Inscribed in stone at Davenport Hall on the University of Illinois Campus reads the quote "The wealth of Illinois is in her soil and her strength lies in its intelligent development. - Draper". To further the intelligent development, there must not only be research related to maximizing the productivity of our soils but, to finding sustainable methods for productivity maximization. The literature shows that a small but promising framework for use of acoustic measurements to examine soil physical properties has been developed in lab settings. Based on these acoustic methods, on-the-go sensors capable of high spatial resolution measurements of soil physical properties may be developed. From the data, models for crop growth may be advanced allowing for more efficient use of input resources such as soil and fertilizer. Efficient use of these resources will decrease overall nutrient run-off levels, enable lower operating costs for farmers, and, most importantly, promote intergenerational sustainability of our soils.

Chapter 2 : Review of the Literature

The field of acoustics, applied to the measurement of soil physical properties, is relatively small, especially in agriculture. Acoustic soil measurement has been researched more holistically in mechanical and geotechnical engineering. However, little of said research has applications to agriculture due to differences in the measurand and overall scale. The use of acoustics in agriculture has targeted soil texture, compaction, and moisture, with emphasis on compaction and moisture.

2.1 Determination of Soil Texture Using Acoustic Methods

Brandon Tate (2016) at the University of Illinois developed a vertical acoustic cone penetrometer outfitted with an audible-range acoustic and a force measurement system. Although the system was mounted on a 3-point hitch and driven from a tractor's hydraulic system, tests were conducted in a laboratory-like setting using soils with well-defined textures. After taking a measurement in air with the tractor running, the cone penetrometer was pressed into the soil samples in a rotating fashion using a hydraulic motor. Throughout the insertion, acoustic and insertion force data were gathered. A stepwise regression model was fit to the frequency domain data using a selection of frequencies which appeared to vary in magnitude against the calibration run. The results showed the best correlation between the acoustic data and clay content with a coefficient of determination (R^2) value of 0.95. In contrast, the correlation between the silt and sand were both below an R^2 of 0.66. To continue this work, other soil characteristics should be measured in conjunction with acoustics to determine what effect soil characteristics have on the acoustic signature (Tate, 2016).

After developing a soil moisture and soil organic matter (SOM) sensor, Lui et al. (1993) began development of an acoustic method for soil texture determination. The method used the soil cutting

tool itself for the creation of acoustic waves. These waves were measured in real time in the audible frequency range. The tine was drawn at a depth of 12 cm through a soil bin (Fig. 2.1) at a constant speed in sandy loam, clay loam, sandy clay loam, and loam soils. These soils represent different classifications based on their particle size. Nomenclature of the classifications may be found using the soil texture triangle (Fig. 2.2). Tests were performed at two soil moistures (1/10 bar & 1 bar) and two levels of bulk density (1.3 g/cm^3 & 1.5 g/cm^3). The tests concluded that there could be certain correlations made between certain frequency bands of different soils and their textures. The authors note the need for better methods to filter out environmental noise (Lui, Gaulteny, & Morgan, 1993).

Figure 2.1: An indoor soil bin as shown is used for representing field conditions in a controlled environment. In operation the tine on the cart is drawn through the wooden box filled with soil while data is collected.

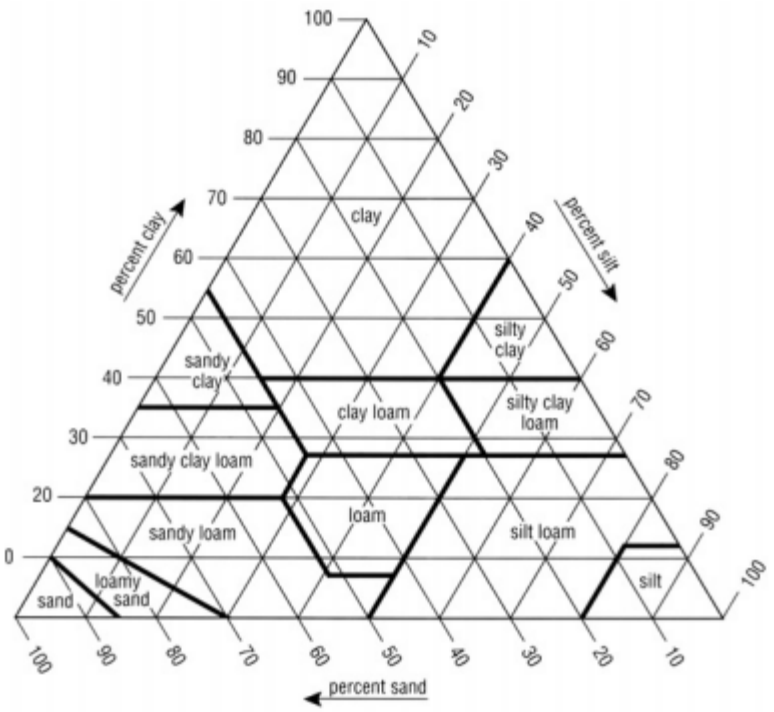

Figure 2.2: USDA soil texture triangle for classifying soils based on particle size.

In 1983 Philip Tringale developed an acoustic cone penetrometer for use in agricultural soils. Testing took place both in laboratory settings as well as in field. The amplitude of the acoustic signal was shown to increase with increasing average grain size and increasing speed. An inverse relationship was shown with amplitude when compared to both penetration resistance and moisture content. The predominant frequencies shown in sand were from 2 kHz to 12 kHz given the level of penetration resistance. Investigation of additional soil properties such as mineralogical composition, hardness, and angularity were suggested for future work (Tringale, 1983).

2.2 Determination of Soil Compaction Using Acoustic and Mechanical Methods

Houlsby and Ruck (1998) built a chamber in which sands were packed to a measured bulk density. Readings from a microphone fitted into a cone penetrometer were taken while the penetrometer was pressed through the soils. The data were analyzed using the Fast Fourier Transform (FFT) and an Artificial Neural Network (ANN). They concluded that 1) ANNs are an

efficient data analysis method for the acoustic data, 2) the acoustic signal was not strongly dependent upon the bulk density, and 3) the strongest correlation between the acoustic data and soil characteristics was found in the range of 13 kHz to 25 kHz. (Houlsby & Ruck, 1998).

Grift et al. (2005) created an on-the-go arrangement for capturing acoustic data from soil, comprising an audible range microphone embedded in a wedge located at the bottom of a steel tine. Measurements were conducted under ambient conditions to account for the noise of the tractor and surroundings. Subsequently, the tine was drawn through a bin of prepared soil at varying compaction levels and depths. Analyses indicated that soil depth and density had a notable relationship with the level of sound produced. The authors recommended further research into the effects of different soil types and varying moisture levels (Grift, Tekeste, & Raper, 2005).

Hemmat et al. (2014) conducted their research using an on-the-go design of a horizontal penetrometer similar to that of Grift et al., the main difference being that the former used three prismatic tips embedded in the wedge, each outfitted with microphones and load cells. They drew the wedge through a clay loam soil taking measurements at 10 cm, 20 cm, and 30 cm depth. Readings were also taken with a vertical cone penetrometer for reference. When processing the data, acoustic signals were filtered using a wavelet transform and then analyzed using a Fast Fourier Transform and the Welch Method. This research concluded that when the tips were below the critical depth (20 cm and 30 cm), where soil failure changes from brittle to compressive, there was a significant correlation between the horizontal resistance index (HRI) and the cone index (CI). However, there was no such correlation between the HRI and CI at 10 cm (Hemmat, Rahnama, & Vahabi, 2014).

Shin et al. (2017) researched the depth profile strength of soil using acoustic to seismic coupling in place of the classic cone penetrometer. This technique uses an acoustic source,

microphones, and a Laser Doppler Vibrometer to obtain acoustic to seismic transfer functions. The shear moduli were then deduced through numerical optimization based on Biot's theory and a wave propagation model. In their final form, the moduli were displayed as a soil strength equivalent. In this experiment, the frequencies of the acoustic waves were low: in the range of 300 Hz to 4 kHz. Shin et al. stated that the acoustic to seismic method was effective in measuring the soil depth profile, although no correlation factors were given between the acoustic-seismic coupling and cone penetrometer measurements (Shin, Watts, Whalley, Attenborough, & Taherzadeh, 2017).

Towner et al. (2000) used a penetrometer outfitted with acoustic instrumentation on the Huygens space probe which was sent to Jupiter's moon Titan. Before the space probe left Earth, the penetrometer was calibrated in the lab to obtain baseline readings from dried common sand and small glass balls which were deemed "ideal matter" because of their spherical nature. Towner et al.'s analysis revealed that the "ideal" glass was characterized by sharp peaks in amplitude around 1 kHz. This was in stark contrast to the shorter peaks in the amplitude spectrum produced along a broader frequency spectrum of around 50 Hz to 1 kHz produced by the dry sand. The discussion of future research was limited to suggesting further study into material cohesion (Towner, Zarnecki, & Marcou, 2000).

Villet et al. (1981) performed research into the acoustic waves generated during the cone penetration of soils. The penetrometer was outfitted with an electric guitar pickup microphone and pressed into cylinders containing various sands. These cylinders were subjected to horizontal pressures, causing stress in the soil. The cylinders were also meticulously prepared to assure uniformity of particle size and vertical distribution. Tests revealed that despite the rate of penetration changing, the major peaks in amplitude associated with a certain frequency occurred

around the same frequency range (10 kHz). The researchers also claim that the peak amplitude was linearly correlated with penetration speed. In addition, when the horizontal and vertical pressures which act upon the soil are changed, the peaks in amplitude were present at different frequencies. This led to a testing constraint where penetration speed and soil pressures must be held constant, to discern any amplitude changes (Villet, Mitchell, & Tringale, 1981).

Chang et al. (2010) used an acoustic cone penetrometer to find an effective means to locate soil strata. The first notable aspect of this work is its deviation from the standard Fourier transform used in similar research projects due to the transient, aperiodic, and non-stationary aspects of the mathematical process. Instead, Chang et al. proposed the use of the Hilbert Huang transform (HHT), which was developed to analyze sound waves, and calculation of the Root Mean Square (RMS) sound pressure. The test was conducted by first placing two known soil types on top of each other in a pit. Then the acoustic cone penetrometer was pushed into the soil until it had penetrated both layers (135 cm). After the data was collected and analyzed, the researchers determined that both the HHT and the RMS analysis showed a difference in the profile layers. However, since the simple RMS analysis in itself highlighted the change in profile layers, the HHT was deemed unnecessary (Chang, Chang, Nguyen, & Wang, 2010).

Lu et al. (2004) investigated the effects of soil compaction on wave velocity in the lab in three types of dry soil. The base of the test was a tri-axial cell filled with soil where two ends were capped with piezoelectric discs. On top of this tube, a load cell was mounted, while a hydraulic cylinder and linear variable differential transformer (LVDT) for displacement recording were attached to the bottom. The soil was packed to a preset pressure, and a pulse was generated with a function generator from one disc and measured with another disc. These waves were generated at 6.5 kHz and repeated at 20 Hz increments. The soil was packed to pressures of 34.5 kPa (5 psi),

68.9 kPa (10 psi), and 103.4 kPa (15 psi) while at each discrete pressure the axial strain was increased from 0% to 15%. The results indicated that for each pressure the velocity of the wave increased linearly with respect to axial strain at the beginning of the test. The velocity would then begin to exhibit a nonlinear increase before plateauing. Due to the predictable change in velocity of acoustic waves caused by increased pressure, the authors recommend acoustic measurement techniques to measure soil compaction (Lu, Hickey, & Sabatier, 2004).

Hall et al. (2005) tested the feasibility of detecting a plow pan during the tillage process using a horizontally oscillating shank. Another target of the research was to find the optimal tip design such that the measurements could be compared to that of a vertical cone penetrometer. Their method used a force transducer coupled with a tip mounted on a large shank. The sensing tip was crafted in three designs. The bottom of the shank was cut at a 45° angle to prevent soil being pushed upward during forward motion. The system was drawn through a soil bin containing a well-defined soil. The testing revealed that at depths of less than 150 mm the horizontal sensor was incapable of obtaining accurate readings. At depths below 150 mm, the horizontal sensor measured the maximum strength within 5 mm of the vertical method yielding an R^2 of 0.95. The last observation of the authors was that the wedge index (horizontal method) more closely correlated with the bulk density than the cone index (vertical method). In conclusion, the authors state that the horizontal method may be better suited for compaction measurements due to a decreased influence of moisture during the test. The type of tip used played a factor in the measurements, although all tips used yielded similar final results (Hall & Raper, 2005).

Adamchuk et al. (2004) developed an on-the-go method to determine mechanical resistance of soil similar to the non-acoustic approach previously mentioned. The main difference is the use of strain gages, in addition to load cells on the sensing unit. The combination of these measurement

systems allowed for a model of mechanical resistance and depth for both the tine and the tip. The model for the tine was treated as the predicted pressure while the value at the tip was considered the measured pressure. Tests showed that a difference between the tine pressure and tip pressure could be used to detect a plow pan. According to the authors, the ability to detect the plow pan in this method coupled with a closed loop control algorithm will allow for automated on-the-go tillage depth adjustments (Adamchuk, Skotnikov, Speichinger, & Kocher, 2004).

Andrade et al. (2004) performed field testing of a soil compaction sensor developed at the University of California at Davis. The compaction measuring device included a tine outfitted with five load cells spanning the entire working length. These load cells allowed for measurement of the entire soil profile. Using a modeling technique taking into account depth, moisture content, bulk density, and width of the shank, the cone index data were graphed against these terms. When the force data from the horizontal measurements were graphed against the model predicted values there existed a correlation with an unspecified coefficient of determination. These data were then coupled with global positioning system (GPS) data, demonstrating that the data could be used to generate soil compaction maps (Andrade, Upadhyaya, Jenkins, Plouffe, & Poutre, 2004).

2.3 Determination of Soil Moisture Content Using Acoustic Methods

Sharma et al. (2010) performed laboratory testing to verify Brutsaert's model (Brutsaert, 1964) of sound wave propagation in agricultural soils. Previously, this model was applied to well compacted soils and the loosely packed agricultural soils were theorized to affect the model relationships. Through the authors' summation of prior literature it was stated that sound wave propagation could be predicted through a system of two compressional waves at low frequencies and a shear wave at high frequencies. In the literature, the speed of sound was found proportional to the degree of saturation, but these findings could not be directly applied to agricultural soils due

to the low compaction level. To test the model assumptions for the new conditions the researchers applied a low frequency (<900 Hz) continuous wave sound to the soil. It was also theorized that the lower limit of this frequency spectrum was estimated to be 150 Hz in conjunction with a minimum distance of 50 cm between the transmitter and receiver. To perform their test, Sharma et al. carefully aligned a transmitter and receiver on opposite ends of a box filled with soil, initially on dry soil. The results showed that in dry soil the speed of sound was inversely proportional to the amount of sand in the box. The soil was then saturated with water in steps. Subsequent tests showed that when the soil reached its maximum saturation point, the speed of sound became constant, and that as the soil dried, the speed of sound began to increase. In summation, Sharma et al. stated that the speed of sound in soil can be calibrated in terms of the degree of saturation (Sharma & Gupta, 2010).

Meisami-asl et al. (2013) examined the feasibility of using acoustics to determine soil moisture. They used frequency sweeping (10-300 Hz) and multiple tone waves in a laboratory testing environment similar to that of Sharma et al., and compared the values to model predicted values. After the data was collected the researchers investigated the effect of soil moisture on peak amplitude, total power, total harmonic distortion, and signal-to-noise ratio (SNR). When peak amplitude was analyzed, there was an R^2 of .999 shown between the soil moisture and peak amplitude when using the frequency sweeping method. Total power was examined next and yielded a 0.999 R^2 when using multiple tone waves. Total harmonic distortion was examined in relation to moisture content using the sweeping frequency method and revealed an 0.998 R^2. Lastly, the SNR was analyzed with the frequency sweeping method and showed a relation to water content of the soil with an .966 R^2. In summary, the researchers found many extremely strong correlations with moisture content in soil and the acoustic properties mentioned above. These

findings lend evidence toward the ability to determine soil moisture content acoustically. (Meisami-asl, Sharifi, Mobli, Eyvani, & Alimardani, 2013)

Adamo et al. (2004) created an inexpensive and accurate moisture sensor for field use. They first modeled acoustic propagation in soils according to Brutsaert's theory of acoustic pulses in soil under a certain series of restrictions. These restrictions concern an upward limit on the inertia-viscosity factor and the wave propagation being approximately plane. Given these restrictions, the model may then be applied to measurements. From the theoretical framework, it has been made clear that the maximum usable signal frequency is around 1 kHz for sand, 2 kHz for loamy sand, and 6 kHz for sandy loam. However, the authors note that when running the model for all soil textures, a safe low limit for frequency is 900 Hz. Adamo et al. also used modeling to determine the distance at which the sensors need to be separated to capture the entire usable frequency spectrum. This distance was determined to be 50 cm. Both the modeling techniques and results portrayed here were very similar to Sharma et al.'s method adding validity to the proposed practical application. A working prototype based on this theoretical framework was developed (Adamo, Andria, Attivissimo, & Giaquinto, 2004).

Although there are many studies covering acoustic and mechanical soil physical property characterization techniques reviewed in this thesis, little has been shown past the proof of concept. In addition, no studies were performed using an acoustic test in a field setting or were on-the-go. The closest study to the work detailed in this thesis was done by Tate (2016) at the University of Illinois, who showed a relationship between clay content of the soil and frequency of acoustic waves generated during penetrometer measurements. However, his work was not on-the-go, showed little correlation in the sand and silt models, and used a very small frequency range. It was

determined after this review that research should be conducted into on-the-go methods using a wider frequency range.

Chapter 3 : Theory and Measurement

Soil physical properties greatly influence the management and productivity of land used both for civil engineering projects and agriculture. These physical properties influence how water and nutrients move throughout the soil. In terms of agricultural productivity the properties are tremendously impactful variables and are considered to be “limiting factors”. Under the Justus von Liebig concept of the limiting factor, it is said that “plant production can be no greater than that level allowed by the growth factor present in the lowest amount relative to the optimum level.” (Brady & Weil, 2004). This principle provides insight into the potential impact of soil physical properties limiting the amount of water or nutrients available to the plant. A non-optimal amount of either will result in loss of potential yield. The key components that make up a soils physical properties are: texture, moisture, strength, density, aggregate structure, and color (Das & Sobhan, 2009).

Soil texture generally describes the range of sizes of the mineral soil particles. These ranges are commonly referred to as sand, silt, and clay. Although there are a handful of classification systems described by standardization organizations and associations of engineers, the United States Department of Agriculture (USDA) standard is the commonly accepted standard for measurements pertaining to agricultural soils (Das & Sobhan, 2009). Most other systems are developed for non-agricultural applications (García-gaines & Frankenstein, 2015). The USDA classification system states that particles from 2.0 mm to .05 mm are classified as sand, from .05 mm to .002 mm as silt, and less than .002 mm as clay. Using the USDA triangle shown in Fig. 2.1 one can use the textural percent composition to determine the texture class; of which there are 12 (García-gaines & Frankenstein, 2015).

Sand is usually made up of primary silicates such as quartz. The particles are large, spherical, have low porosity and hence, a low specific surface area. These properties promote movement of water and air throughout the soil. The particles are also considered non-cohesive, meaning they do not clump together. Silt, the middle size classification of particles, is also primarily made up of silicates. Due to the smaller size, these particles are prone to faster weathering than sand, which provides a significant amount of plant nutrients. The higher specific surface area results in more numerous but smaller pores in silt. In silty soils water is trapped among the pores preventing draining. Lastly, silt particles themselves exhibit very poor cohesion. However, most silt particles are surrounded by a thin film of clay. Clay exhibits very high levels of cohesion due to the electromagnetic charge of the particles. Clay is the smallest size of the distribution and has properties very different from those of sand and silt. Due to the small particle size, the specific surface area is very large, allowing for high levels of water absorption. As the water content of clay progresses from low to high, the physical properties shift from brittle to malleable. These particles behave like colloids and do not settle out of water well. Another important characteristic of clay is the type of clay mineral plays a large role in overall function. This makes the type of clay as important as the amount (Brady & Weil, 2004).

There are three main methods for determining the particle size distribution of the soil. The first, known as the ribbon method, is only used for estimations and therefore not used in this thesis. The second and third methods will be used in unison to determine the full spectrum of the particle size distribution. After air drying of the sample, sieving is the first method used. This consists of passing the soil through a set of sieves with progressively smaller grates. If only the large aggregate distribution is desired, analysis may cease here. If the fine particle distribution is sought, the third method, hydrometer analysis, is used. This method uses the soil remaining in the finest grate from

sieving (0.075 mm) to determine distribution of the small diameter particles. In hydrometer analysis, measurements of ambient temperature and moisture are taken before dispersion of the soil sample using sodium hexametaphosphate. The fine particles are left suspended in solution for a standard time duration with periodic measurements of the hydrometer being recorded. The settling velocity can be determined by Stokes Law shown in Equation 3.1 (Das & Sobhan, 2009). Using this equation, the particle diameter can be solved for through rearrangement of the equation given the settling velocity.

$$v = \frac{\rho_s - \rho_w}{18\eta} * D^2 \qquad (3.1)$$

where v equals the settling velocity of the soil particles in m/s, and ρ_s & ρ_w represent the density of soil and water respectively in $\mathrm{g/cm^3}$, η is the viscosity of water in g∗sec/cm and D represents the particle diameter in cm. In application of this law to soil particle analysis ρ_w = 1 and $\rho_s = \rho_w * G_s$ is assumed where G_s is the specific gravity which is a function of soil particles present per unit volume. The hydrometers are calibrated such that G_s is assumed to be 2.65 $\mathrm{g/cm^3}$ (Liu & Evett, 1997).

Soil moisture describes the volumetric water content of the soil. Changes in this characteristic can cause major fluctuations in the physical structure of the soil, such as shrinkage, swelling, changes in adhesion, and, ultimately, shifts in aggregate structure. The moisture level also affects most chemical measures such as salinity and acidity (Brady & Weil, 2004). In a lab setting, along with a bulk density measurement, soil moisture is calculated by weighing a sample of soil, baking it in an oven at 105°C, and then weighing it again. For in-field measurements, the current common practice is to use Time Domain Reflectometry (TDR) (Topp & Davis, 1985). This technique uses the dielectric constant of water, ε, to determine volumetric water content (VWC). Using a regression equation, an approximate relationship of VWC and ε was established for most soils

(Kirham, 2014). In practice, a basic set up consists of a pair of electrodes of a length between 0.1 m and 1 m, connected to a coaxial cable. This shielded cable is connected to a cable impedance matching device (balun) which leads to the TDR instrument. Measurements are taken by pulsing a voltage signal in the gigahertz frequency spectrum through the soil and capturing the signal reflected by the soil. A timing device is used to synchronize the pulse generator and receiver. After superimposing the pulse on the reflected signal one may use time domain analysis to correlate the measurement with moisture. A drawing of this basic set up is show in Fig. 3.1 (Topp & Davis, 1985).

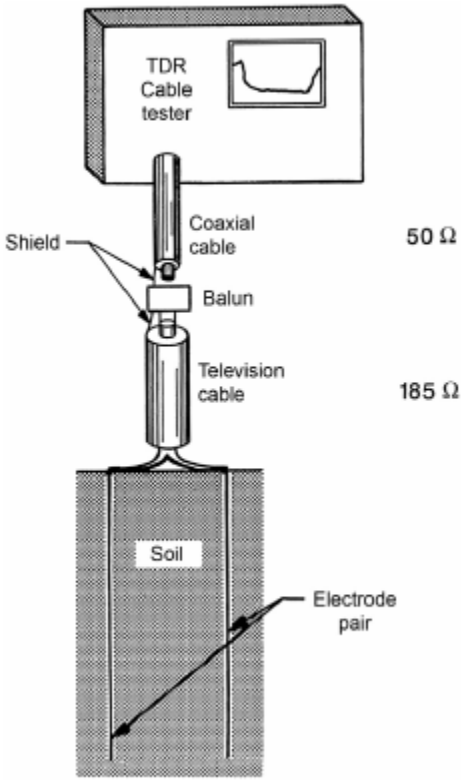

Figure 3.1 TDR Device Setup

Soil shear strength, or the capacity to resist shear failure, is another important factor that affects physical structure. Changes in shear strength can affect compaction, root penetration, and water

movement. Two main factors that play a role in soil strength are cohesive forces among particles and static friction. Shear strength is nearly universally characterized by the Mohr-Coulomb Equation 3.2 (Wesley, 2010):

$$s = c' + (\sigma - u) * tan\,\phi \qquad (3.2)$$

where s represents the shear strength ($\mathrm{kN/m^2}$), c' ($\mathrm{kN/m^2}$) is the cohesion intercept derived from the bonding between particles, and σ & u represent the normal stress ($\mathrm{kN/m^2}$) on the shear plane and the pore pressure on the shear plane respectively ($\mathrm{kN/m^2}$). Lastly, $\tan\phi$ represents the angle of shearing resistance in degrees. The shear angle is found by finding the vector from the Mohr-Coulomb Failure Line on the Shear vs. Normal Stress plot (Wesley, 2010). Soil shear strength is measured in a lab setting using either the unconfined compression test, the tri-axial compression test, or the direct shear test. The unconfined compression test is used to investigate cohesive, undisturbed, or dried soil specimens. The test first requires placing an extracted soil core between two load bearing plates. The soil is then compressed until failure. The tri-axial test is essentially the same test, with the addition of lateral pressure to the sample. The sample is placed inside a rubber membrane fitted inside a chamber that may be pressurized with air or water. An axial load is then applied until failure. The tests are differentiated in that the tri-axial compression test may be run on cohesionless particles where the unconsolidated compression test may not.

The last laboratory test is the direct shear test. This test measures the angle of shearing resistance and cohesion level with σ & u held constant. The test is carried out by placing soil into two stacked metal squares with the centers removed. The specimen is then packed to a constant normal force and the boxes are separated vertically by approximately 0.6 mm. The boxes are placed in the test apparatus and the top half is fixed while the bottom half is attached to the horizontal displacement arm. The arm will then begin to apply a shear force to the soil. The force

and displacement are measured in increments of 2% of the specimen diameter until failure. A diagram of this apparatus is show in Fig. 3.2 (Olson & Lai, 2004). These data allow for the creation of a shear vs. normal force plot with Mohr's circles for the prediction of soil failure as seen in Fig. 3.3 (Wesley, 2010).

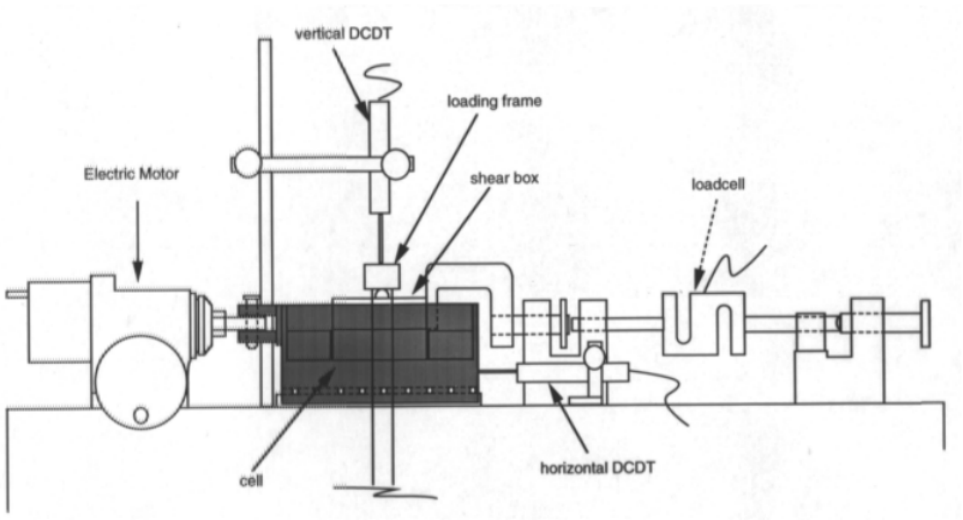

Figure 3.2: Direct shear test apparatus for determination of soil shear strength.

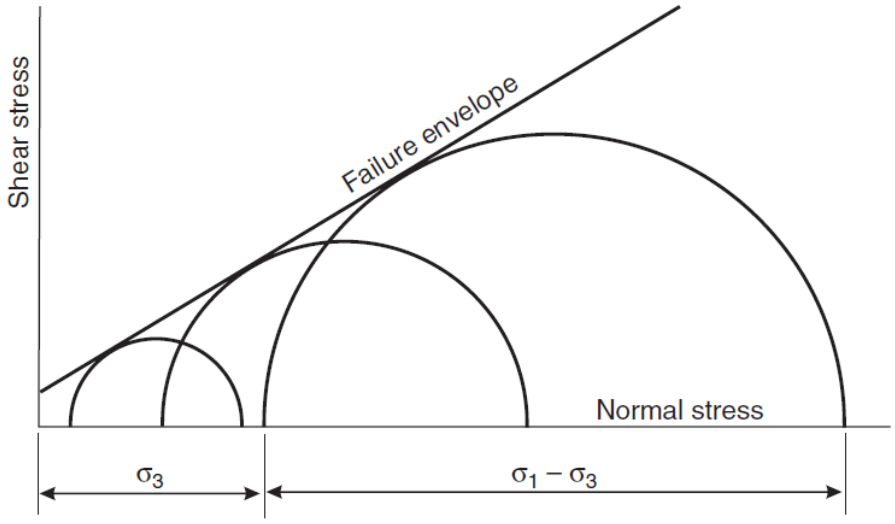

Figure 3.3: Shear stress vs. normal stress plot as shown is used for prediction of soil failure.

In the field there are two main ways to measure shear strength. The first and less commonly used for agricultural purposes is the vane shear test. The shear strength of the soil is found using Eqn. 3.3 (Das & Sobhan, 2009).

$$S_u = \frac{T}{2\pi R^2 \left[1+\frac{2R}{3H}\right]} \tag{3.3}$$

where T is the torque applied in (Nm), and the denominator is determined by the dimensions of the testing apparatus (m). The test is conducted through insertion of the vane show in Fig. 3.4 into a soil with high clay content (Wesley, 2010). The vane is then torqued until failure of the soil.

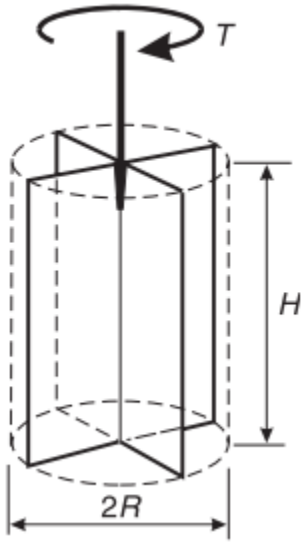

Figure 3.4: Vane shear test apparatus used for in-situ determination of soil shear strength.

The second method for in-field testing is known as the cone penetrometer (CP) method. The American Society of Agriculture and Biological Engineers (ASABE), as well as many other Engineering Associations, have set standards for this method of testing. The ASABE standard will be the standard for this thesis (American Society of Agricultural and Biological Engineers, 2013a). Detailed explanation of this standard is found in the National Engineering Handbook published by the National Resource Conservation Service, which gives proper testing procedures and

interpretation of data for end users of cone penetrometers (National Resource Conservation Service, 2012). The ASABE standard details proper design for the cone (tip) of the CP as show in Fig. 3.5. The design is specified because the size of the cone will impact the sensitivity of the device. There are two accepted cone diameters with 12.83 mm being the default.

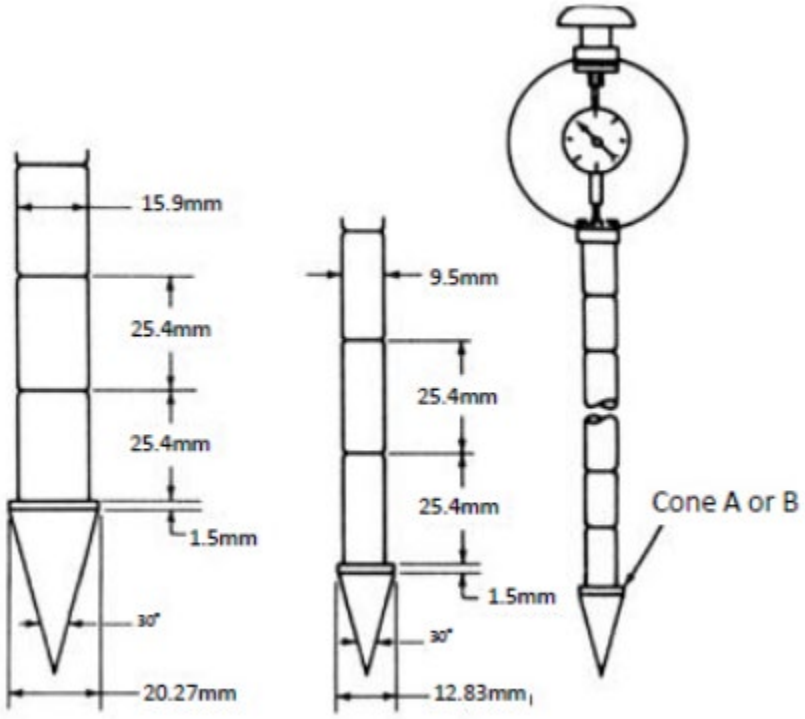

Figure 3.5: ASABE standard cone penetrometer dimensions.

Performing the field test is relatively simple and specified in ASABE EP542 Standard (American Society of Agricultural and Biological Engineers, 2013b). In the desired location, the user places the tip against the soil and inserts the CP at a rate of approximately 30 mm/s. Data should be taken at depth increments of 50 mm or less. On digital systems, the CI or cone index, which is an expression of exertion force over area (MPa), is output at the corresponding depth. These data can be used to represent compaction levels and also correlate to undrained shear strength (National Resource Conservation Service, 2012). There has been a theoretical correlation

between undrained shear strength and CI characterized by Eqn. 3.4 however due to a multitude of variables, there is no one constant for an adjustment term rendering application difficult (American Society of Agricultural and Biological Engineers, 2013b). In the equation, S_u represents undrained shear strength (MPa), q_t & σ_t represent total cone resistance (MPa) and vertical stress respectively (MPa), and N_{kt} the empirical cone factor. The empirical cone factor is based on empirical data and ranges from 12-20. For practical purposes, a value of 15 is accepted. The number of samples needed to provide a reliable estimate of shear strength is characterized in the standard by Eqn. 3.5 where n represents sample size, s the standard deviation, d the acceptable error in decimal form, and t, the value from the student's t distribution.

$$S_u = \frac{q_t - \sigma_t}{N_{kt}} \tag{3.4}$$

$$n = \frac{{t_\alpha}^2 * s^2}{d^2} \tag{3.5}$$

Chapter 4 : Experimental Methods

Initially this chapter discusses the design of the testing apparatus (5.1), sensor design (5.2), and data collection system (5.3) used for on-the-go testing. The next sections discuss the construction of outdoor (5.4) and indoor (5.5) soil bins used for controlled testing. Lastly the experimental methods (5.6) are described along with results from laboratory particle size analysis.

4.1 On-the-go Testing Apparatus Design

To conduct on-the-go testing in field environments a testing apparatus was designed and assembled. The main mounting structure of the testing apparatus was constructed out of 10.16 cm (4") tube steel and 1.27 cm (0.5") steel plate. It was built to fit the standard dimensions of the class four three-point hitch receiver as specified by the ASABE (American Society of Agricultural and Biological Engineers, 2014). The tine was machined by Wagner Machine Company in Champaign, IL based on drawings generated in SolidWorks®. The tine is 19 mm (0.75") in depth and 15.24 cm (6") by 0.91 m (36") in width and length. Two 6.35 mm (0.25") steel plates were cut and welded onto the main mounting structure. The tine was then bolted onto the plates using 25.4 mm (1") grade 8 bolts. 12.7 mm (0.5") rubber pads were placed in between the tine and steel plates to aid in dampening any machine induced vibrations. The testing apparatus was designed in SOLIDWORKS 2017 Student Edition (SOLIDWORKS 2017®: Dassault Systems: Waltham, Massachusetts). A 3D model of the testing apparatus is shown in Fig. 4.1. A TYE (The TYE Co., model 304-413, Lockney, TX) implement was used to connect the testing apparatus to the tractor (Deere and Company, model 6115R, Moline, IL). It also served the function of providing accurate depth control from the surface of the soil to a 0.40 m (16") depth and for leveling of the testing apparatus. Two instrumentation boxes were mounted on the testing apparatus. One box, measuring 0.35 m (14") x 0.254 m (10") x 0.15 m (6"), was attached to the mounting structure to protect the

preamplifier. The second box which measured 0.61 m (2’) x 0.61 m (2’) x 0.20 m (8”) was mounted atop the TYE machine to house the data acquisition components. Figure 4.2 shows the testing apparatus as mounted on the TYE implement and hitched to the tractor. Figure 4.3 shows the testing apparatus connected to the TYE machine.

Figure 4.1: This drawing represents a 3D model of the testing apparatus. The testing apparatus is comprised of the three-point hitch, mounting plates, rubber insulation, and tine.

Figure 4.2: This image shows the tractor, TYE implement, and testing apparatus used for in field testing.

Figure 4.3: This photograph shows the combined TYE implement & testing apparatus.

4.2 Acoustic Emission Sensing Wedge Design

An acoustic emission sensing wedge (AESW, Fig. 4.4) was designed to house the sensor used for data collection. The wedge was machined out of a 15.24 (6”) x 10.16 cm (4”) steel block with cavities added allowing for insertion of the sensor housing (Fig. 4.5). The wedge mounted to the tine through a pin allowing for minor rotational movement. The rotational movement of the wedge was added to allow a load cell to be mounted vertically as opposed to horizontally. As the AESW is drawn through the soil, minor rotation will occur resulting in a measurable strain on the load cell. The AESW tip is a triangular wedge converging at a 53° angle toward the soil engaging end. The base of the triangular tip measured 5.10 cm (2”) in width with a height of 3.81 cm (1.5”) and 5.10 cm (2”) from the point of convergence to the base. This resulted in a total surface area contacting the soil of 43.22 cm^2 (6.7 in^2). The dimensions were not replicated from previous literature. Instead they were determined by the geometry of the tine.

Figure 4.4: The picture shows the AESW which houses the acoustic emission sensor.

Figure 4.5: This picture represents the bottom view of the AESW. From the bottom view the cavity where the sensor is inserted can be seen.

Inside the cavity machined out of the AESW a 3D printed sensor capsule (Fig. 4.6) was inserted to protect the sensor. This also ensured adequate levels of surface contact with the AESW. In order for the sensor to be fitted into the capsule, the sensor must be dropped into the slot and then a tab inserted between the sensor and capsule (Fig. 4.6). A threaded rod was inserted in the back of the AESW which may be hand tightened against the sensor capsule tab, pressing the sensor against the AESW. A proper level of contact at the sensor-AESW interface was deemed critical by the manufacturer to obtain reliable measurements. According to the selection criteria stated in the ASTM standard for mounting acoustic emission sensors, any petroleum based gel may be used as a bonding agent for testing at frequencies below 500 kHz (American Soceity for Testing and Materials, 2018). For practicality the coupling medium chosen was petroleum jelly. This bonding agent was applied at the initial installation of the sensor to the AESW and reapplied periodically. A hole was drilled and tapped on top of the AESW above the sensor capsule to allow for the sensor wire to exit. For protection of the wire during field testing, a 12.7 mm (0.5”) steel tube was threaded into the tapped hole. This tube extended into the tine which had holes bored for wire routing.

Finally, a cover plate was inserted into the bottom of the AESW to prevent the buildup of soil and the sensor from falling out. Dimensional drawings of the AESW, cover plate, and sensor capsule are available in appendix A.

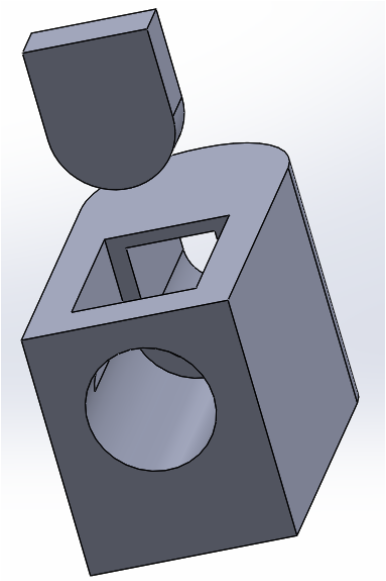

Figure 4.6: This drawing shows the sensor capsule and tab used to secure the acoustic emission sensor.

4.3 Data Collection System Design

When the AESW is drawn through the soil, high frequency excitations will be created at the wedge-soil interface. These high frequency excitation were stored and processed to determine if a relationship exists between physical properties of the soil and the collected data. The sensor being used to capture these vibrations is a Digital Wave Broadband Acoustic Emission Sensor (Digital Wave, model B1025). The sensor was connected to a pre-amplifier (Physical Acoustics Corp., model 1220A) using a 10-32 microdot to BNC shielded cable. The pre-amplifier was used to provide 40 dB amplification to the signal before reaching the main amplifier (Physical Acoustics Corp., model 08648). The main amplifier was powered by a DC to AC inverter (Westward, model 26W998) in line with the tractor battery (Fig. 4.7). It provided an additional 6 dB gain to the signal before broadcasting to the data acquisition unit (DAQ). The gain was selected so that

measurements fell in the [-10, 10] VDC range of the DAQ (Measurement Computing, model USB-1208HS). The physical selection process took place by starting with the lowest gain possible and running the machine through soil. The gain was then adjusted one increment and the machine was run again through soil. This procedure was done until measurements laid outside the capabilities of the DAQ. Then the gain was decreased one decrement and five replications were completed to ensure a proper set point. Data was recorded from the acoustic emission (AE) sensor and the load cell using a DAQ with a sampling rate of 1 MS/s. Signals from the AE sensor were initially sampled at 500 kHz to prevent aliasing in the high frequency application according to the Shannon Nyquist Sampling Theorem (Marks II, 1993).

The AESW was also fitted against an S-type load cell (Omega Engineering, model LC101-100) to collect reference force data during operation. The load cell was connected to a load cell amplifier (Omega Engineering, model DRF-LC-VDC-30MV-0/10) for power, calibration, and signal conditioning. The load cell amplifier was connected to a 12 VDC to 24 VDC step up convertor (Electronix Express, model 78DCCON12V) powered by a DC power supply (Global Specialties, model 1310). The DC power supply was powered by the same inverter used in the acoustics system powered by the tractor battery (Figure 4.7). This system was enacted to condition the supply of power coming from the tractor and subsequently decrease the noise of the signal from the load cell. Due to the equal sampling parameters of each channel for the data acquisition unit, the load cell was also sampled at 500 kHz. It was found during initial testing that the load cell used did not provide the proper load range for this testing. After the purchase of a second load cell (Omega Engineering, model LC101-200) with twice the rating, it was found that soil became wedged into the space between the AESW and tine. This caused readings from the load cell to

spike to the peak load until cleaning. As a result, load cell data was not collected. Since only the AE sensor was being sampled by the DAQ the sampling rate was changed to 1 MS/s.

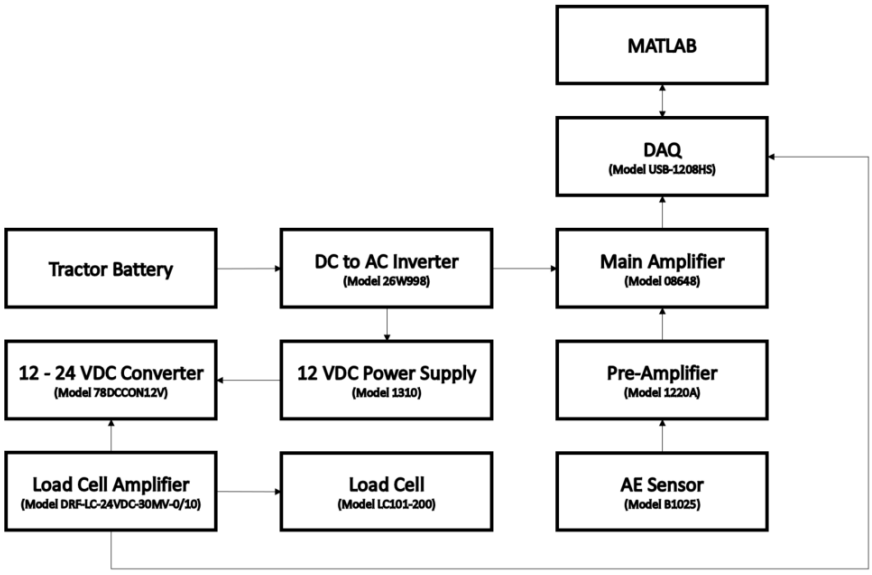

Figure 4.7: This diagram represents the electronic system used for on-the-go data collection.

Software controlling the data acquisition was developed using Matlab R2017b (Matlab, ver. 9.3: Natick, Mass: The Math Works, Inc.). An example of the graphical user interface (GUI) is shown in Fig. 4.8. Through this GUI, the user can enter the sampling rate, sampling duration, and file name. After use of the load cell ceased, the GUI was changed to operate only the AE sensor (Fig. 4.9). This included changing the auto populated rate to 1 MS/s for the AE sensor and deleting load cell related sampling and data representation.

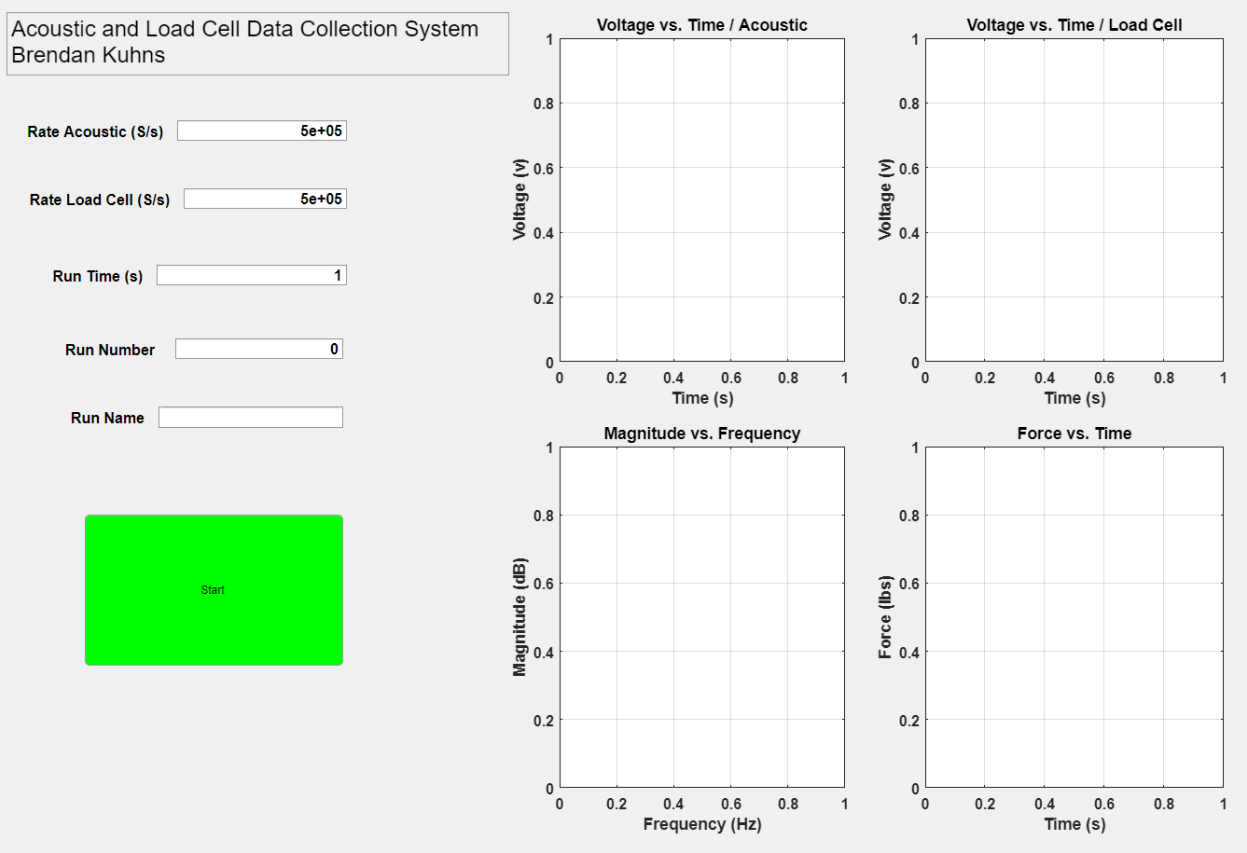

Figure 4.8: This picture represents the GUI used for data collection from the AE sensor & load cell.

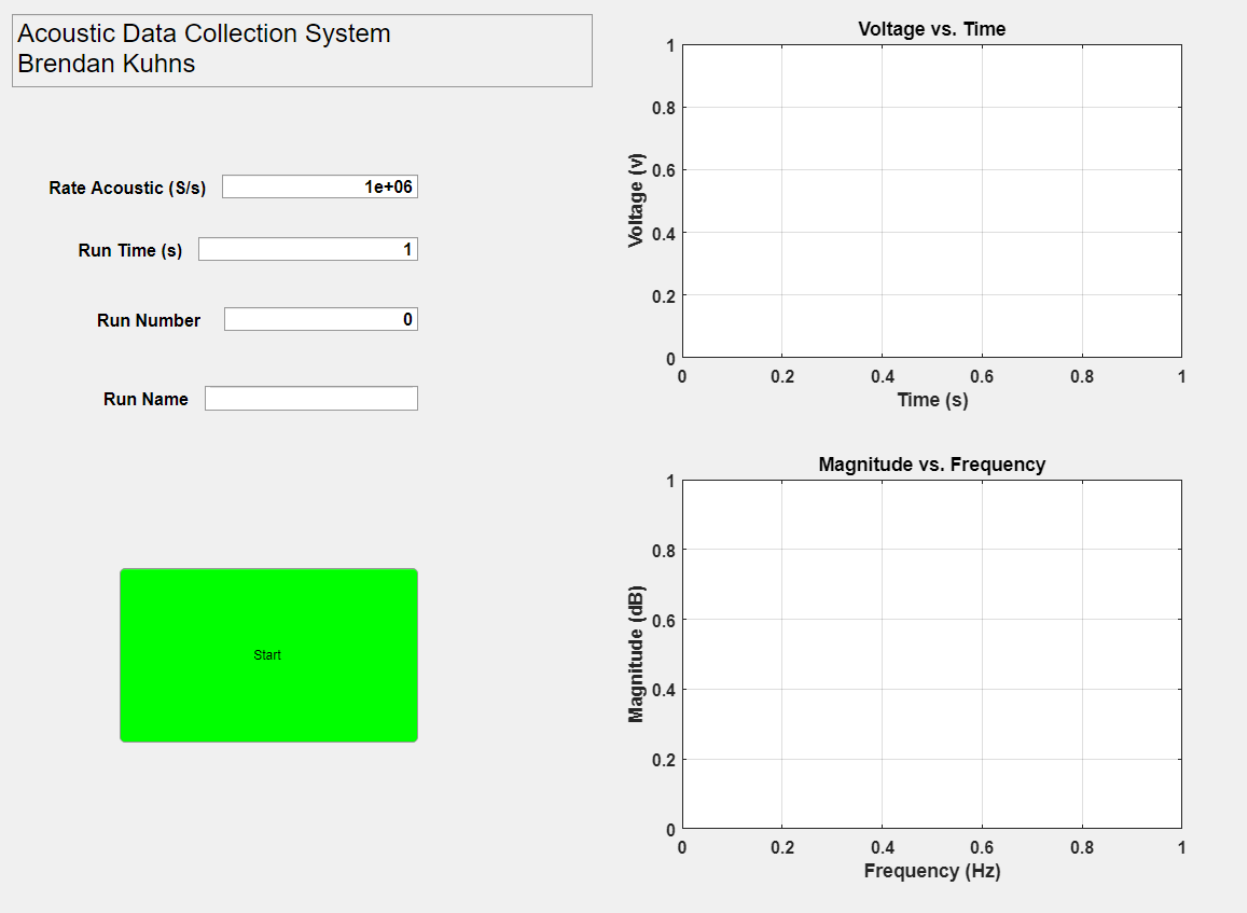

Figure 4.9: This picture represents the GUI used for data collection from only the AE sensor.

4.4 Outdoor Soil Bin Design

Given the short sampling window for field trials and lack of available soil textures, an outdoor soil bin was installed at the Agricultural Engineering Research Farm at the University of Illinois (Urbana, IL). A physical bin was built from pressure treated lumber, screws, and lag bolts. The bin was 4.87 m (16') long, 0.762 m (30") wide with a 0.56 m (22") usable height. The height of the bin was selected based on the maximum depth capabilities of the testing apparatus plus a large cushion to prevent any boundary affects. The width was chosen based on the size of the bucket available for the mini-excavator to dig up the soil. A 1.0 m (40") deep by 1.27 m (50") wide hole was dug so that the top of the bin sat level with the natural soil surface after installation. Before

the physical structure was installed, a 10.16 cm (4”) plastic tile line was laid in the ground and covered with construction sand. The tile outlet was capped at 30.48 cm (1’) underground near the end of the bin allowing for water to be pumped out if the need arose. Atop the construction sand the bin was seated and steel rebar was driven into the ground through holes on the bin for stability. Reinforcements at the top of the structure were used while lowering the bin to prevent the walls from caving in; before testing these were removed. After backfilling the hole around the bin, it was filled with construction sand purchased at Mid-America Sand and Gravel (Mahomet, IL). This bin was used for outdoor on-the-go testing in sand and can be seen in Fig. 4.10. Originally, it was intended for the sand to be replaced with a clay soil in the bin after testing. However, due to early onset of winter weather conditions in fall of 2018, construction sand was the only texture observed in the outdoor bin.

Figure 4.10: This picture shows the outdoor soil bin after it was lowered into the trench.

4.5 Indoor Soil Bin Design

After initial characterization of the sensor was performed in a field setting, an indoor soil testing system was developed so that testing could continue through the winter months (Fig. 4.11). The framework for this system was built from dimensional lumber and various sizes of tube steel. A steel fixture with wheels was fabricated to house the same tine and AESW used in the outdoor tests. This fixture containing the wedge was pulled along a wooden track system above a wooden bin containing soil. The bin stood .762 m (30”) off the ground and was 1.82 m (6’) in length and 0.27 m (11”) in width. The steel fixture was pulled along the track using a hydraulic cylinder connected to a pulley system shown in Fig. 4.12. The hydraulic power unit used to drive the cylinder was repurposed from other research. The pulley system was chosen to provide the speed necessary to compare measurements from field tests to the indoor tests. Based on a measured retraction rate of .045 m/s (0.1 mph) for the hydraulic cylinder, the drive was outfitted with a pulley arrangement allowing for a 10 to 1 mechanical advantage which would then pull the tine at 0.44 m/s (1 mph). The power needed to move the tine through the soil will change based on soil compaction and type. For repeatability, the system must be able to maintain a constant speed regardless of the load. Therefore, a hydraulic cylinder was chosen as the drive mechanism because it will maintain a constant speed up to the maximum load regardless of the load. On the opposite side of the steel fixture, a weighted pulley system was added to dampen accelerations caused by cable elasticity and to automatically retract the steel fixture after the test (Fig. 4.13). Since this test system was indoors and only contained the acoustic data collection system, the instrumentation need was significantly decreased. The pre-amplifier was attached with Velcro on the side of the tine above the greatest height of possible soil contact. The data acquisition unit and main amplifier

were attached to a plastic plate using DIN rail. This plate was bolted on top of the tine using angle brackets.

Figure 4.11: This picture shows the indoor soil bin used for simulating field use of the AESW in an indoor environment.

Figure 4.12: The picture shows the indoor soil bin pulley drive system. This pulley system was chosen in conjunction with the hydraulic piston to provide a constant speed regardless of the load on the AESW.

Figure 4.13: The dampening and retraction system shown in this picture was used to maintain tension on the cable which prevented speed fluctuations. The system also automatically retracted the tine after a test.

4.6 Test Methodology

Before field data were taken, tests with the AESW out of the soil with the tractor at an idle and at a velocity of .045 m/s (1 mph) were completed. Testing of the AESW began in field conditions. A previous study which regulated the trafficking and tillage methods on research plots was

leveraged for the field testing in this research. The protocols of this study maintained a detailed record of machinery paths and tillage treatments at the row level. Based on these practices experiments were developed to investigate the sensitivity of the AESW to compaction, speed, and soil texture.

The first test that was performed aimed to quantify the impact of speed on the acoustic measurements. Moisture data were taken in six rows that had been treated earlier with identical practices in a separate project where the impact of low-pressure tires on field soil was studied ("Michelin" study). A TDR meter (Field Scout, model TDR300) was used to gather moisture data before the test began. Ten samples were taken per row and the moisture data was analyzed in the field. The row with the most uniform moisture distribution was chosen for the test. The moisture reading in the chosen row ranged from 36% VWC to 41 %VWC with no clear gradient. The treatment type used in the Michelin study for the selected rows was low ground pressure tires on all equipment and a fall deep tillage with a spring secondary tillage pass. Measurements were taken after harvest in between rows zero & one where no direct machinery traffic had been seen since the start of the three-year study. Sampling was not taken in the sprayer tracks that ran perpendicular to the rows. Four replications of sampling took place at intervals of 0.89 m/s (.2 mph) beginning at 0.89 m/s (.2 mph) spanning to 0.98 m/s (2.2 mph) with each test lasting 0.5 seconds.

The next experiment aimed to gain a basic understanding of the effect of compaction on the acoustic measurements. Data was collected first between rows zero and one which were under the previously mentioned treatment type. Between these rows no direct machinery traffic had been seen since the start of the study. Eight measurements were collected at a tractor speed of 0.44 m/s (1 mph) at a depth of 10.16 cm (4") for 0.5 seconds. Under the same parameters, the next eight measurements were collected in between rows three and four of the same replication where ample

machinery traffic had occurred for the duration of the Michelin study. Moisture data and compaction data were taken along each of the measurement zones. The moisture was sampled until two areas with a similar five measurement average were found. These areas marked the specific test location along the row. Seven data points of compaction were taken per row location using a cone penetrometer (Field Scout, model SC900). Additionally, five measurements were performed for a duration of one second of run time between rows zero and one. These data would be used for textural analysis.

The outdoor soil bin was utilized for the next stage of experimentation. The 16' bin was filled with construction sand purchased at Mid-America Sand and Gravel. Immediately before testing, data was gathered with a cone penetrometer and moisture meter. The penetrometer data revealed 0 psi for the cone index at all depths where data would be recorded. The TDR moisture meter indicated between 0% and 1% VWC spanning an 20.32 cm (8") depth for ten measurements. Ten replications of one second measurements were taken at a speed of .44 m/s and a depth of 10 cm. After each replication, the top 15 cm of sand was shoveled off and re-poured into the bin. The sand was then leveled with the top of the bin to ensure a uniform depth. Due to poor weather conditions all further experimentation was held indoors using the indoor soil bin.

Two more textures, river sand and Fairmount sand, were tested using the indoor soil bin. Data were recorded at a depth of 10 cm at a travel speed of .44 m/s. Ten measurements were taken of each texture for 0.5 seconds and ten were taken for a duration of 1 second. Before each experiment, data was taken using the cone penetrometer and TDR moisture meter. Similar results were seen with respect to CI and VWC compared to the outdoor bin. After each replication, the top 15 cm of soil was shoveled off and re-poured into the soil bin. The surface was smoothed to a standard height after re-pouring based on markings inside the bin.

Particle size analysis was performed on the four soil textures using a combination of the hydrometer and sieve methods. Laboratory procedures were performed according to the methods specified in the text *Soil Mechanics Laboratory Manual* (Das, 2002). Only the sieve method was used for the sand textures and the loam texture utilized both the sieve and hydrometer method. Based on availability of laboratory equipment, the sieve sizes between the number 10 and 200 reflect slightly different openings than called for in the text's methods. A summary of the percent compositions according to the USDA classification is shown in Fig. 4.14 (García-gaines & Frankenstein, 2015).

Table 4.1: The table displays results from the particle size analysis for construction sand (CS), Fairmount sand (FS), river sand (RS), and loam (L).

Soil Separate	Particle Diameter Range (mm)	Percent Composition			
		CS	FS	RS	L
Very Coarse Sand	1.00 - 2.00	5.22%	0.36%	25.71%	5.68%
Coarse Sand	0.50 - 1.00	21.03%	92.84%	30.42%	3.05%
Medium Sand	0.25 - 0.50	38.60%	6.34%	26.34%	9.36%
Fine Sand	0.10 - 0.25	33.30%	0.45%	14.76%	25.88%
Very Fine Sand	0.05 - 0.10	1.86%	0.01%	2.75%	7.83%
Silt	0.002 - 0.05	0.00%	0.00%	0.02%	31.10%
Clay	<0.002	0.00%	0.00%	0.00%	17.10%

Chapter 5 : Results

This chapter details analysis of various aspects of the signal with relation to soil physical properties and other testing parameters. Section 5.1 examines the effect of tractor speed and section 5.2 examines the effect of compaction. Section 5.3 analyzes the signal to noise ratio between the data collected and calibration data. Sections 5.4 and 5.5 explore the possibility of additional dimensionality and the variability of the time series respectively. The frequency spectra and principal component analysis of said spectra are discussed in sections 5.6 and 5.7.

5.1 Speed Model

Results from the speed test were analyzed to access the possible impact of speed on future tests. All data used in this thesis, aside from signal to noise calculations, were run through a 50 kHz to 250 kHz band pass filter using Matlab's Signal Processing Toolbox. Initially, the energy of the signal in the time domain was hypothesized to have a correlation with the speed of the tractor. The energy was calculated using a trapezoidal Riemann approximation substituted for the voltage into a derived version of Ohms Law (Eqn. 5.1) (Lathi, 1998).

$$E_s = \frac{1}{Z} \sum_{i=1}^{M} \frac{f(x_{i-1}{}^2)+f(x_i{}^2)}{2} \Delta x \tag{5.1}$$

In this equation Z represents the characteristic impedance of the DAQ input line which was assumed at 1 ohm since the data collection system was identical for all runs. The impedance of the DAQ input line is different from the transmission lines used to connect the amplification system. These transmission lines were 50 ohm cables for maximization of power throughput. The function $f(x_i)$ represents the voltage measurement as a function of time. M denotes the total number of samples which is found by multiplying the sampling time by the sampling rate in S/s. Δx is the distance in seconds between the measurements.

From these data, a regression model was created to calculate the correlation between signal energy and tractor speed. The model was developed using Matlab and the Statistics and Machine Learning Toolbox. Signal energy will serve as the dependent variable with tractor speed as the independent. The data were best fitted to a quadratic polynomial curve and resulted in a coefficient of determination R^2 of 0.3 and an adjusted R^2 of 0.266 (Fig. 5.1). The residuals vs. fitted values plot is shown in Fig. 5.2, and indicates, along with the low R^2, a very poor fit.

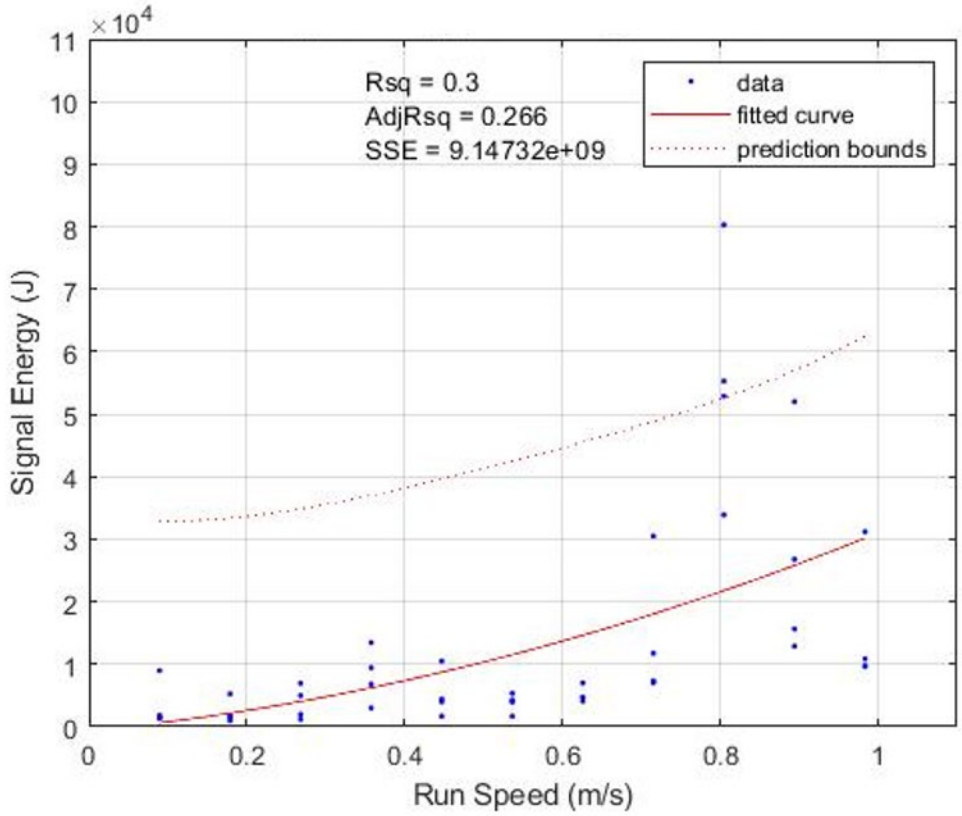

Figure 5.1: This graph shows the signal energy vs. run speed model of the full speed range fit to a quadratic polynomial curve.

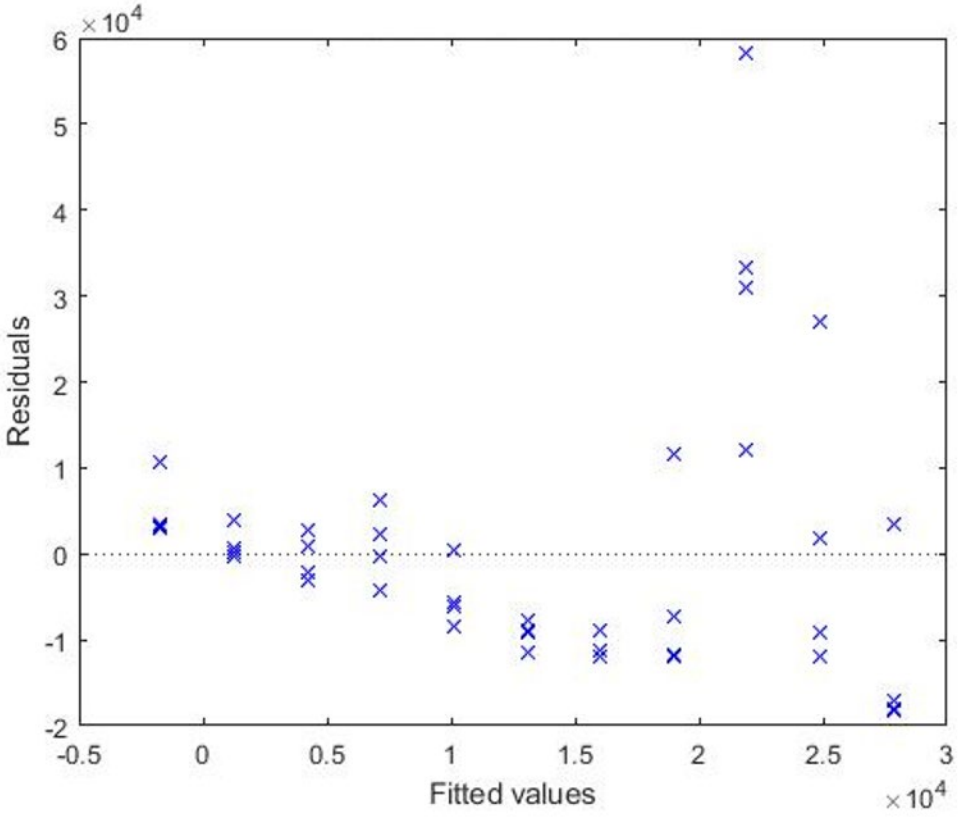

Figure 5.2: This plot shows the residuals vs. fitted values of the signal energy vs. speed model shown in Fig. 5.1. The plot indicates a poor fitment of the model.

Due to the poor regression fit, the time series data were re-analyzed to determine any possible experimental errors. From this analysis, it was concluded that runs past 0.72 m/s should not be counted, as many of the readings were outside the bounds of the data acquisition unit (Fig. 5.3). This problem could be alleviated by tuning the gain of the main amplifier, however, the gain cannot be adjusted on-the-go. A partial goal of this model is to demonstrate what speed range is acceptable at a set gain. Using the reduced maximum speed, a new model was created using the speed range of 0.089 m/s (0.2 mph) to 0.72 m/s (1.6 mph). The same regression analysis was performed on the filtered data. A quadratic fit showed to have the best correlation with an R^2 and adjusted R^2 of 0.224 and 0.171 respectively (Fig. 5.4). Like the previous model, the residuals vs. fitted values

plot (Fig 5.5) with the low R^2 show there is little correlation between the signal energy and tractor speed.

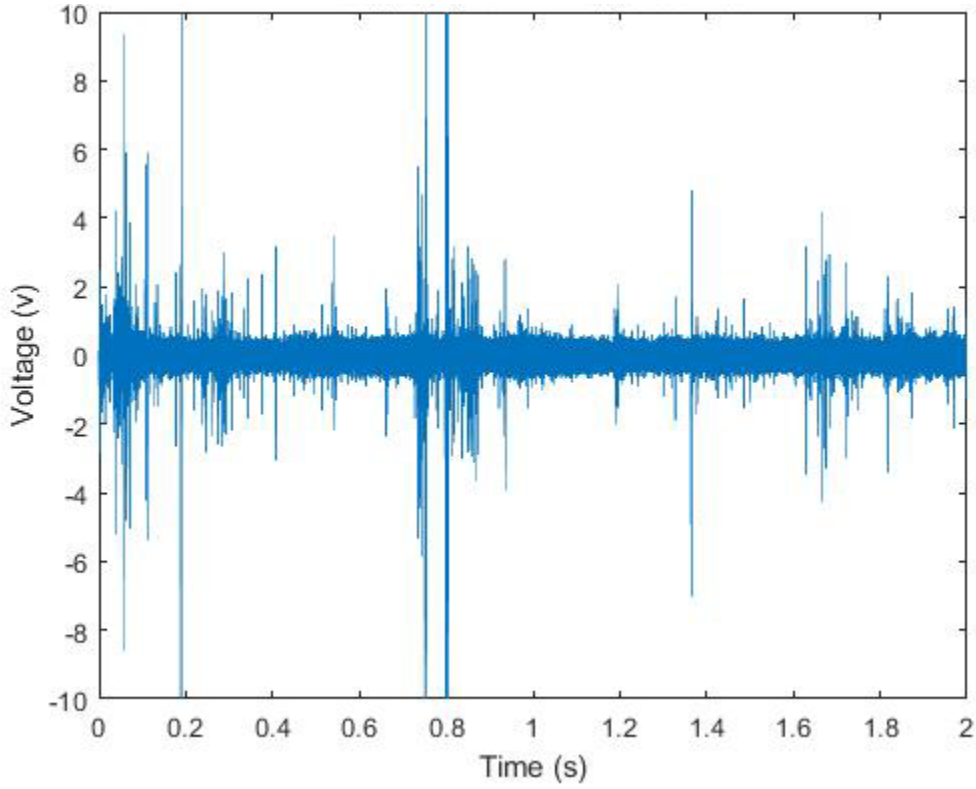

Figure 5.3: This graph shows the voltage vs. time from data collected while traveling at 0.98 m/s. Near times 0.2 s, 0.7 s, and 0.8 s clipping of the signal occurs which may result in incorrect signal energy measurements.

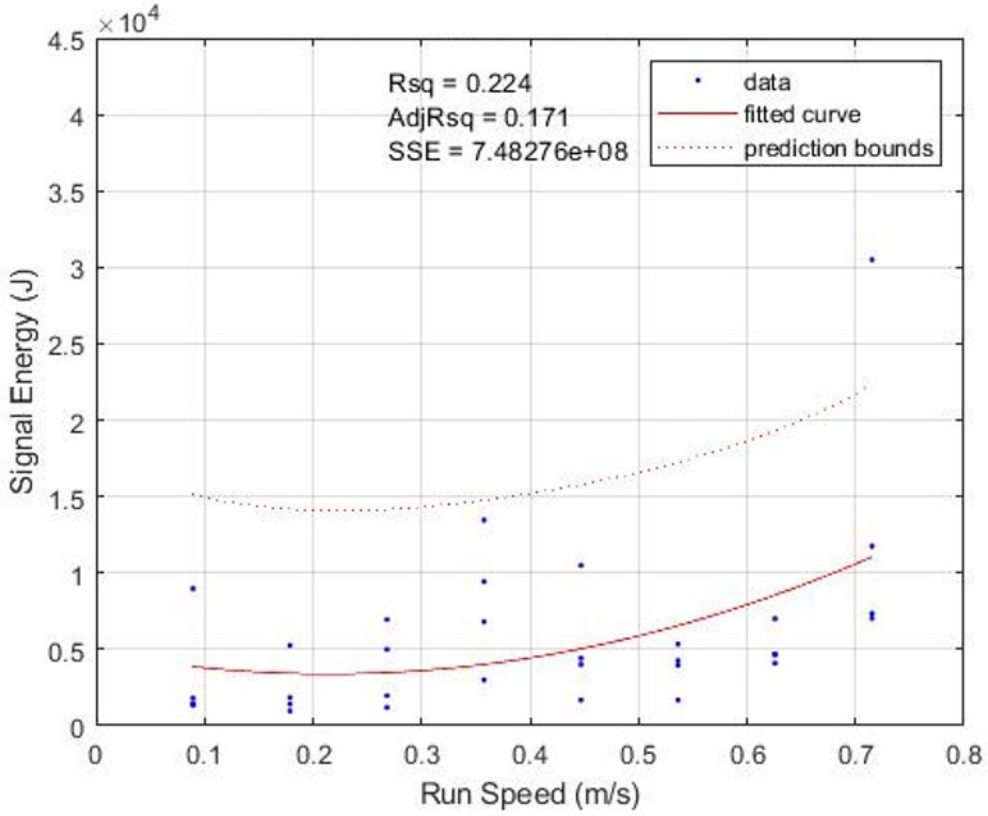

Figure 5.4: This graph shows the signal energy vs. run speed model with a filtered speed range of 0.089 m/s to 0.72 m/s. The data were best fit to a quadratic polynomial curve with a very low R^2.

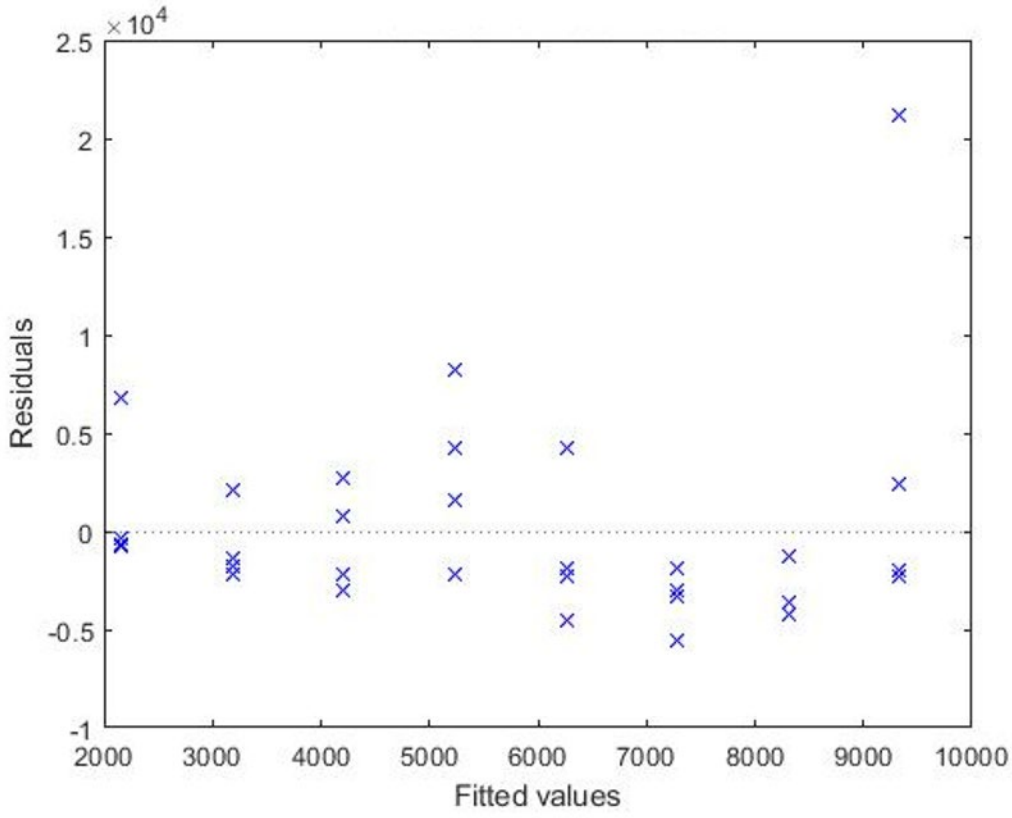

Figure 5.5: The figure shows the residuals vs. fitted values plot for the signal energy vs. run speed model show in Fig. 5.4. The plot indicates a poor fitment of the model.

This poor regression fit led to a re-valuation of the initial hypotheses. After close inspection of the time series, it appeared that the amplitude and quantity of peaks in voltage did not correlate with the speed of the tractor. The general band of the signal however, seemed to grow as the speed increased. To better capture this growth, it was decided that the average of the absolute value of the voltage should be evaluated as opposed to the signal energy. The new function is described in Eqn. 5.2 where M is the total number of measurements calculated by multiplication of the sampling time in seconds by the sampling rate (S/s). x_i represents the i^{th} voltage measurement of the sample. The average value is less sensitive to large peaks than the signal energy. The offset in average from a large peak can be quickly diminished by a few smaller measurements which better represent

the overall band of the voltage. In the signal energy the addition from the large peak is not averaged, therefore if it creates a large offset the total energy will retain said offset.

$$V_a = \frac{\sum_{i=1}^{i=M} |x_i|}{M} \tag{5.2}$$

With the average voltage data, a new regression model was fit where the average voltage served as the dependent variable and the tractor speed as the independent. Using Tukey's ladder of powers (Church, 1979) various transformations were applied to the data. The best transformation was found to be the square transform of the x axis. This transform was applied to the speed data so that the model's quadratic relationship could be evaluated using a linear fitment. A linear regression model was fit to this curve with an R^2 of 0.797, an adjusted R^2 of 0.791, and sum square error of .0028 (Fig. 5.6). The degree of fitment can be seen in the residuals vs. fitted values plot (Fig. 5.7) and the normal probability plot of residuals (Fig. 5.8). An *F* test was also run to access the overall significance of the model. The null hypothesis of this test states the fit of an intercept only model and the model under consideration are equal. The alternative hypothesis states the fit of an intercept-only model is significantly lower than the model under consideration. Then *t* statistics were calculated for all model terms. This test determines if the value of the terms are significantly different from zero and rejects the null hypothesis in the case said terms are found significant. The corresponding p values associated with the *F* and *t* statistics indicate the overall model and all terms are significant. The sum square errors were evaluated for normality using the Kolmogorov-Smirnov test (K-S test) which resulted in statistical confirmation of a normal distribution with a p-value of .997. These values and other summary statistics of this model are found in table 5.1. The results of this model show a correlation between average voltage and tractor speed.

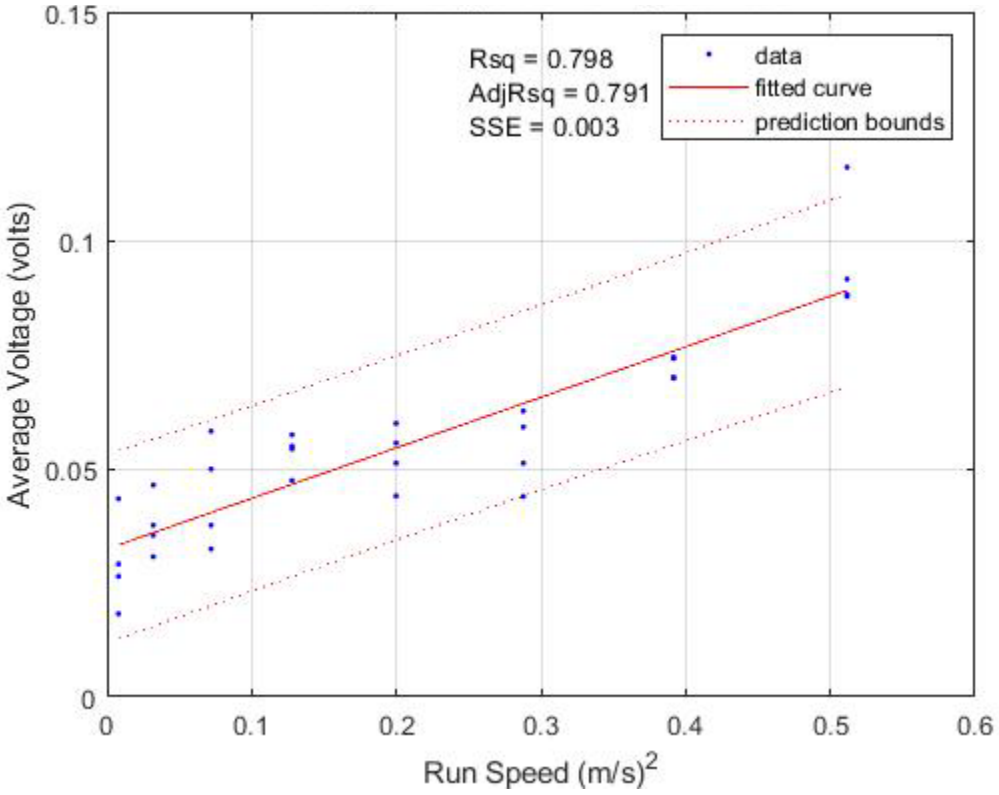

Figure 5.6: This plot shows the average voltage vs. run speed model with a square transform applied to the x axis. The transform allows the model to be analyzed in a linear fashion which results in more robust conclusions.

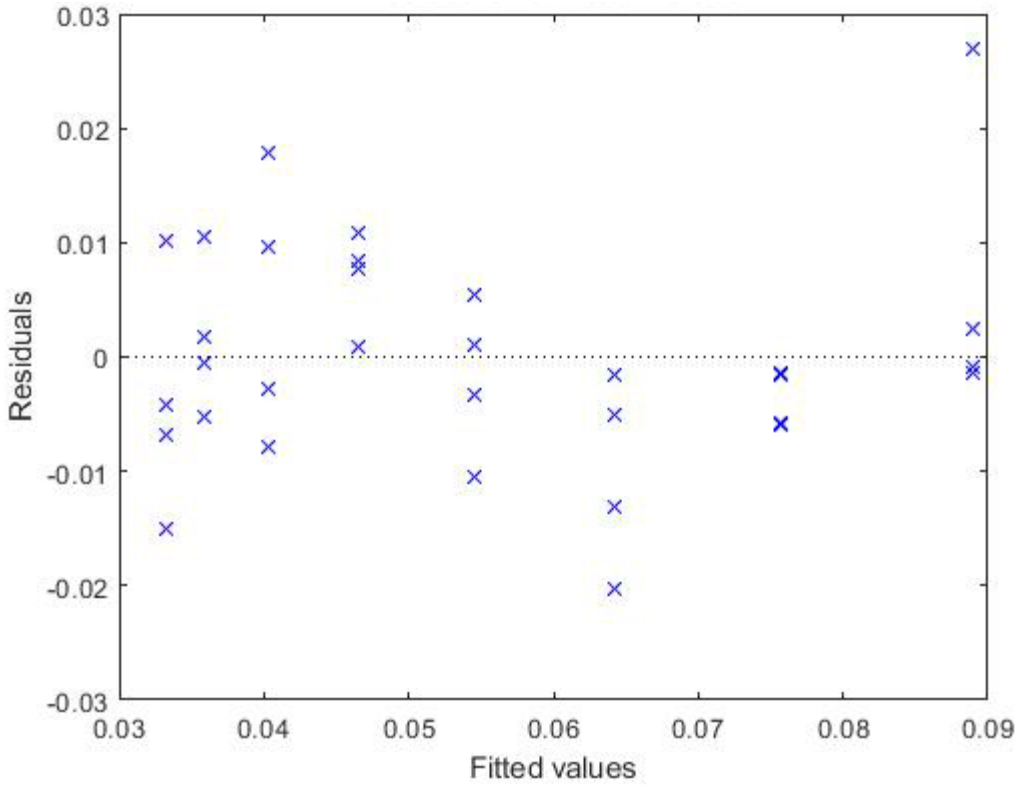

Figure 5.7: This plot shows the residuals vs. fitted values for the average voltage vs. run speed model shown in Fig. 5.6. This plot indicates a reduction in outliers compared to the models of signal energy and run speed.

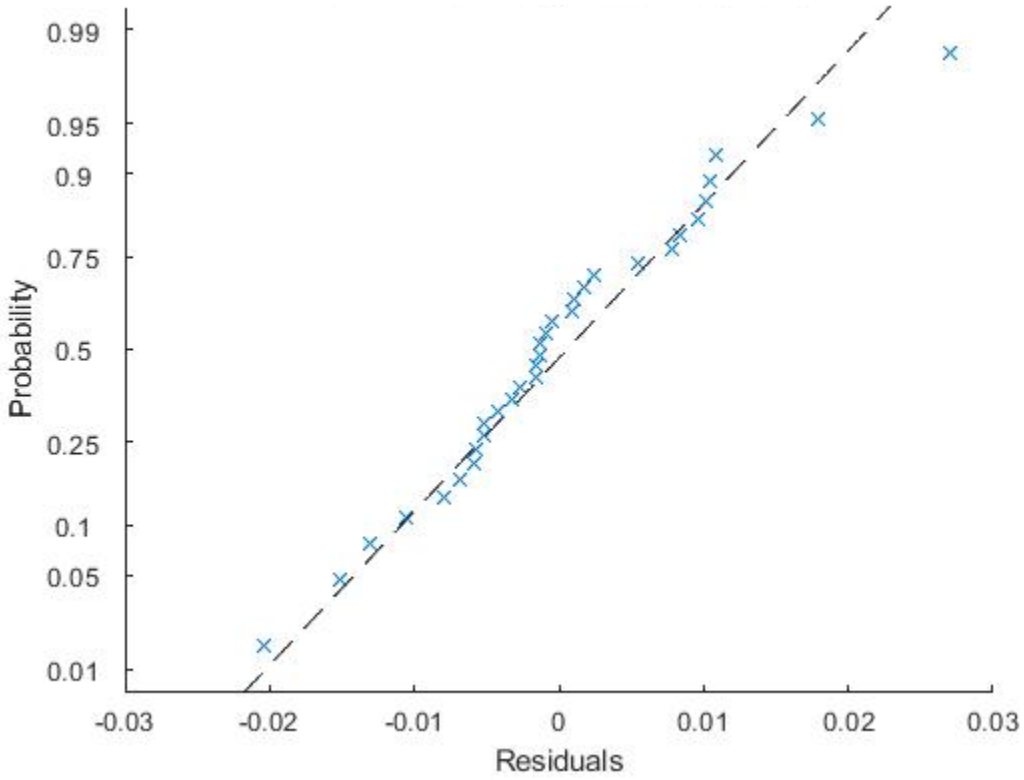

Figure 5.8: The normal probability plot of residuals show for the average voltage vs. run speed model in Fig. 5.6 indicates normally distributed residuals.

Table 5.1: This table shows a statistical summary of the average voltage vs. run speed model. The summary indicates a robust model relationship between average voltage and run speed.

Equation of regression	$y = .0221x + .0323$
Transform	$y = x^2$
Coefficient of determination	0.798
Adjusted coefficient of determination	0.791
Sum of squares error	0.003
Root mean square error	0.0097
F statistic *p*- value	6.30E-12
Intercept *t* statistic *p*- value	5.38E-13
x term t statistic *p*- value	6.31E-12
SSE K-S test *p*- value	0.997
Degrees of freedom	30

5.2 Compaction Test

Evaluation of the compaction data took place by first calculating the signal energy of the measurements (Eqn. 5.1). Then the measurements taken under high compaction were separated from those taken under low compaction, and a Kruskal-Wallis test was run to access the difference between the medians. The analysis was done using the Matlab Statistics and Machine Learning toolbox. The Kruskal-Wallis test was chosen because it does not require normality to produce a statistically significant result, since it is a nonparametric test dependent upon the Chi-square distribution. This characteristic was necessary because as no measurements of passive acoustic vibrations in the desired frequency and given application have been taken at a population level, it would have been difficult to assume normality of the population distribution. The signal energies served as the ordinal variable and the compaction level (high, low) served as the categorical variable. Since, in this scenario, the Kruskal-Wallis test was only ran with two groups no post-hoc evaluation was necessary (Kruskal & Wallis, 1952). Seven cone penetrometer measurements were taken adjacent to the acoustic measurement sites for each compaction group. The data for the first .15 m (6”) of measurement were averaged per group. The high compaction group averaged 706

kPa while the low compaction group averaged 426 kPa. Due to the large range of the constant magnitude adjustment to convert the cone index to undrained shear strength (Eqn. 3.4), the CI was used only as general figure to stratify the two groups. Five moisture measurements were taken in each groups' test area. The high compaction group averaged 33.6 % VWC and the low compaction group averaged 33.0% VWC. These results are summarized in table 5.2.

Table 5.2: This table shows the averaged cone penetrometer and moisture data for the two compaction groups.

	CI (kPa)	Moisture (%VWC)
High Compaction (G1)	706	33.6
Low Compaction (G2)	426	33.0

The null hypothesis of the Kruskal-Wallis test states that the data in each column originates from the same distribution. The alternative hypothesis states that not all groups originate from the same distribution. The results conclude that the null hypothesis is rejected at an α of 0.01 and there is sufficient evidence to suggest a difference in population distribution between the signal energy of the high compaction soil and low compaction soil. Summary statistics for the Kruskal-Wallis test are shown in Table 5.3.

Table 5.3: This table represents the summary statistics from the Kruskal-Wallis test. The test concludes a statistically significant difference in distribution of the signal energy between the two compaction levels.

Source	SS	df	MS	Chi-sq	Prob>Chi-sq
Columns	240.25	1	240.25	10.6	0.0011
Error	99.75	14	7.125		
Total	340	15			

5.3 Signal-to-noise Ratio

To confirm the validity of the sensor readings, the signal-to-noise ratio (SNR) was calculated. The data utilized were from the previously mentioned compaction study and calibration runs taken

before testing began. Each dataset represents one second of sampling. The SNR for signal energy in the time domain was calculated according to Eqn. 5.3 (Horowitz & Winfield, 2015). x_i and x_j represent the i^{th} and j^{th} measurement of signal voltage as a function of time for the test in the compaction environment and calibration respectively. Here, Z represents the impedance of the DAQ input line which was parameterized to 1 ohm for all analyses. M is the total number of samples found by multiplication of the sampling time in seconds by the sampling rate (S/s). Δx represents the interval in seconds between the measurements.

$$SNR_e = 10 * log_{10}\left(\frac{\frac{1}{Z}\sum_{i=1}^{M}\frac{f\left(x_{(i-1)}{}^2\right)+f(x_i{}^2)}{2}\Delta x}{\frac{1}{Z}\sum_{j=1}^{M}\frac{f\left(x_{[j-1)]}{}^2\right)+f\left(x_j{}^2\right)}{2}\Delta x}\right) \qquad (5.3)$$

The data in table 5.4 details the total energy across the entire signal calculated using Eqn. 5.1. Table 5.5 provides the signal-to-noise ratios in dB of the signal energy when comparing various calibrations and compaction states (Eqn. 5.3). For the static and dynamic calibration in the low compaction environment the signal-to-noise ratio was 17.50 dB and 17.62 dB respectively. In the high compaction environment, the SNR was 25.08 dB for static and 25.19 dB for dynamic calibration. Figures 5.9 and 5.10 show the signal-to-noise ratio of the power spectral density estimate across the selected frequency spectrum of 5 kHz to 250 kHz. The SNR for a given frequency was calculated using Eqn. 5.4 (Chan, 2017). In this equation the SNR is derived using the power spectrum calculated during a Welch's power spectral density estimate. P_i and P_j represent the power of the signal in the frequency domain for the signal and noise respectively. Equation 5.4 was applied to all frequencies in the spectrum to create plots for the SNR representing the gain in dB given the frequency. Figures 5.9 and 5.10 compare the static calibrations with the low and high compaction data respectively. Figures for the dynamic calibrations and two compaction states are found in appendix B and show nearly identical results. The data from both

the SNR of the signal energy from the time series and the SNR in the frequency domain indicate an acceptable SNR for data analysis and that there is no effect from tractor operation.

$$SNR_f = 10 * log_{10}\left(\frac{P_i}{P_j}\right) \quad (5.4)$$

Table 5.4: Signal energy data for assessment of the signal to noise ratio.

Static Calibration Energy (J)	Dynamic Calibration Energy (J)	Low Compaction Energy (J)	High Compaction Energy (J)
3.86E+02	3.64E+02	2.13E+04	1.22E+05
3.77E+02	3.66E+02		
3.71E+02	3.74E+02		

Table 5.5: This table represents the signal-to-noise ratios of the time series signal energy for varying calibration methods and compaction states.

Run Number	Static Calibration vs. Low Compaction (dB)	Static Calibration vs. High Compaction (dB)	Dynamic Calibration vs. Low Compaction (dB)	Dynamic Calibration vs. High Compaction (dB)
R1	17.41	24.99	17.66	25.24
R2	17.51	25.09	17.64	25.22
R3	17.58	25.15	17.54	25.11
Average	17.5	25.08	17.62	25.19

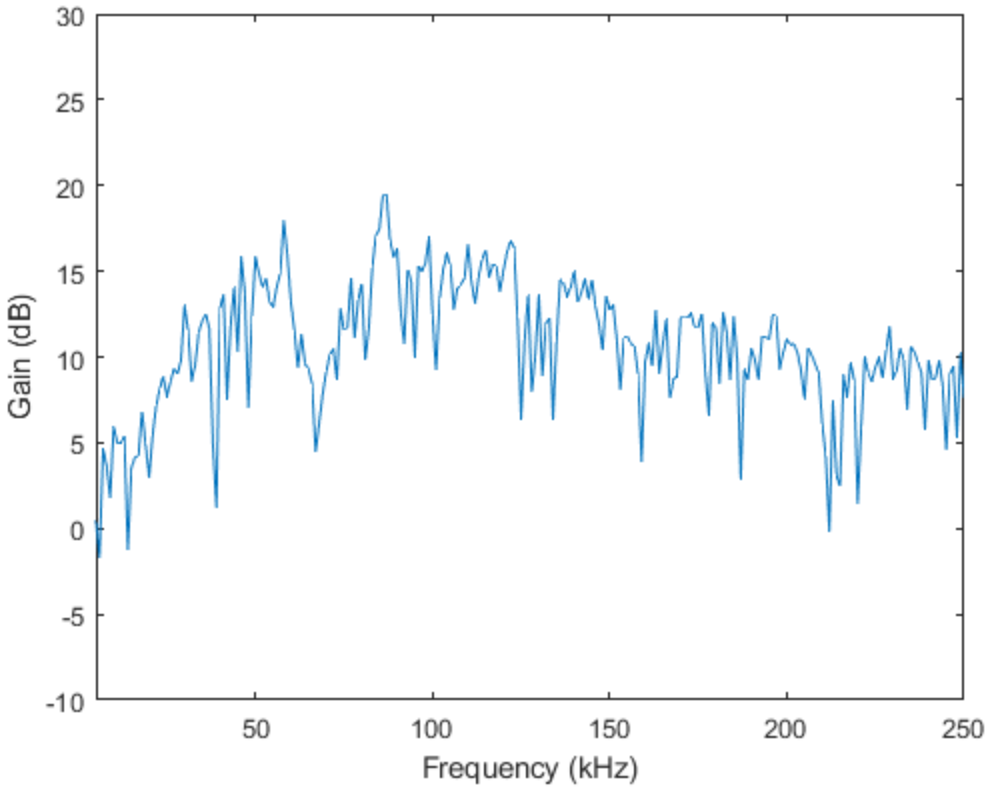

Figure 5.9: This figure shows the power spectrum signal-to-noise ratio across the frequency domain between the low compaction run and the static calibration.

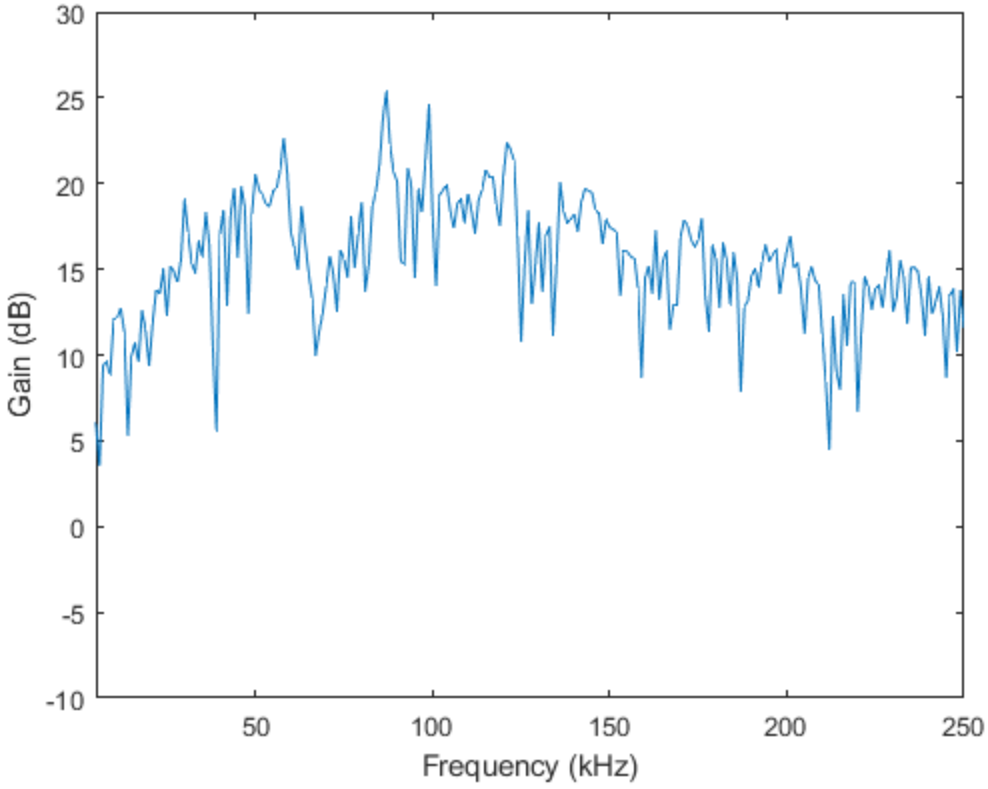

Figure 5.10: This figure shows the power spectrum signal-to-noise ratio across the frequency domain between the high compaction run and the static calibration.

5.4 Fractal Dimension

The fractal nature of the time series was investigated to determine a possible relationship between the fractal dimension of the signal and the soil texture. A fractal is defined as a mathematical object that exhibits similar features on various scales, a phenomenon known as self-similarity (Gonzato, Mulargia, & Marzocchi, 1998). The fractal dimension is a statistical index representing the complexity of a signal (or image), given the scale of measurement. Mathematically the fractal dimension (D) is described in Eqn 5.5. In this equation S represents the increase in scale and ϵ signifies the magnification factor. The units for the increase in scale in this

case are in μs. For a one-dimensional signal, the fractal dimension is a real number between 0 and 1.

$$D = \frac{ln(S)}{ln(\epsilon)} \tag{5.5}$$

This analysis depicts the voltage vs. time series in a 1 dimensional representation. The box counting method was used in Matlab to find the fractal dimension of acoustic data gathered in construction sand. The output shown in Fig. 5.11 represents a plot of how the fractal dimension changes given the magnification factor (box size). Aside from a small dip at a box size of around 10^4 μs the fractal dimension remains constant at 1. Since the fractal dimension of a straight line is 1, this analysis indicates that the time series possesses no additional dimensionality. Therefore no comparisons may be made between signals.

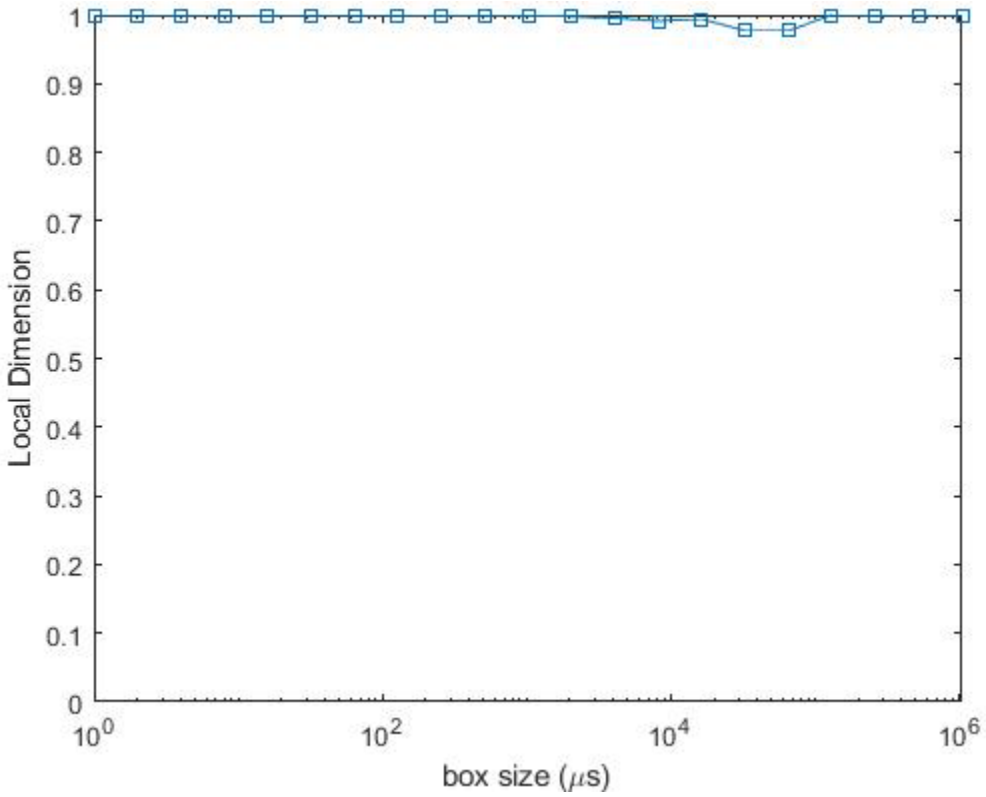

Figure 5.11: This plot shows the local dimension vs. box size plot for 1 second of run time in construction sand.

5.5 Time Series Variability Analysis

Comparisons were made between the voltage vs. time data taken in a loam soil and data recorded in the construction sand from the outdoor soil bin. Data were recorded at the same depth (0.1 m) and same speed (0.44 m/s). This revealed a drastic difference between the time series data among the different textures. In the data taken in the loam soil (Fig. 5.12) it appeared there was considerably more variability in the signal than in the construction sand signal (Fig. 5.13). Commonly in acoustic emission testing, a point of large variability is deemed an acoustic emission count (AE count(s)),(Villet et al., 1981).

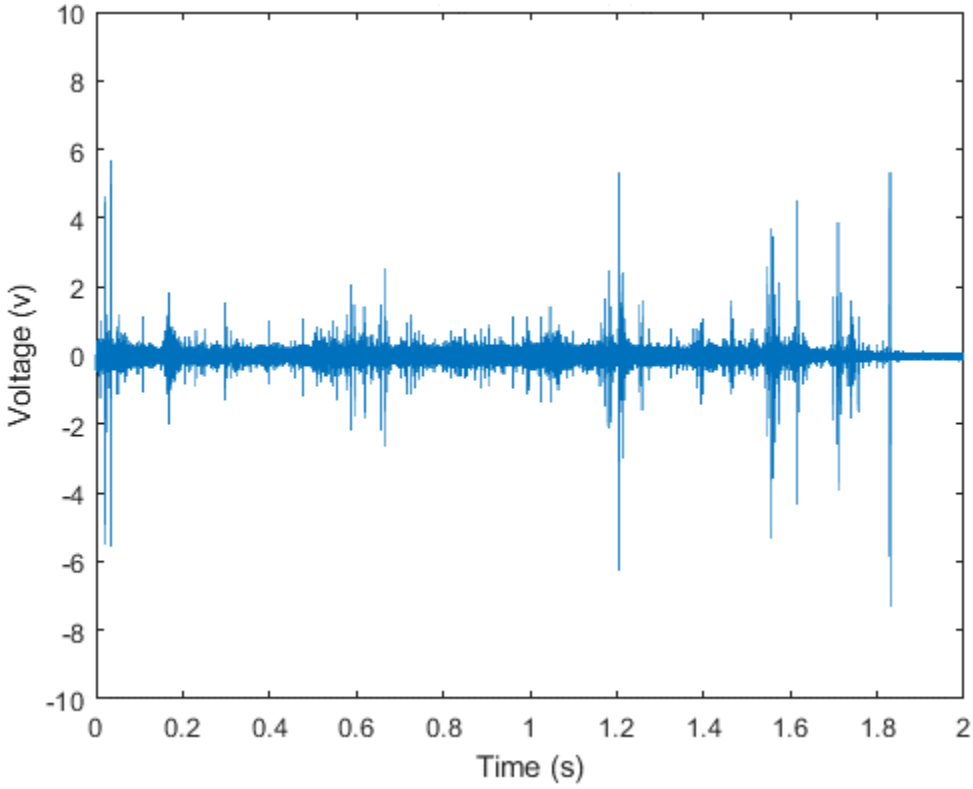

Figure 5.12: This figure shows the voltage vs. time plot of data collected in a loam soil traveling 0.44 m/s at a depth of 0.1 m.

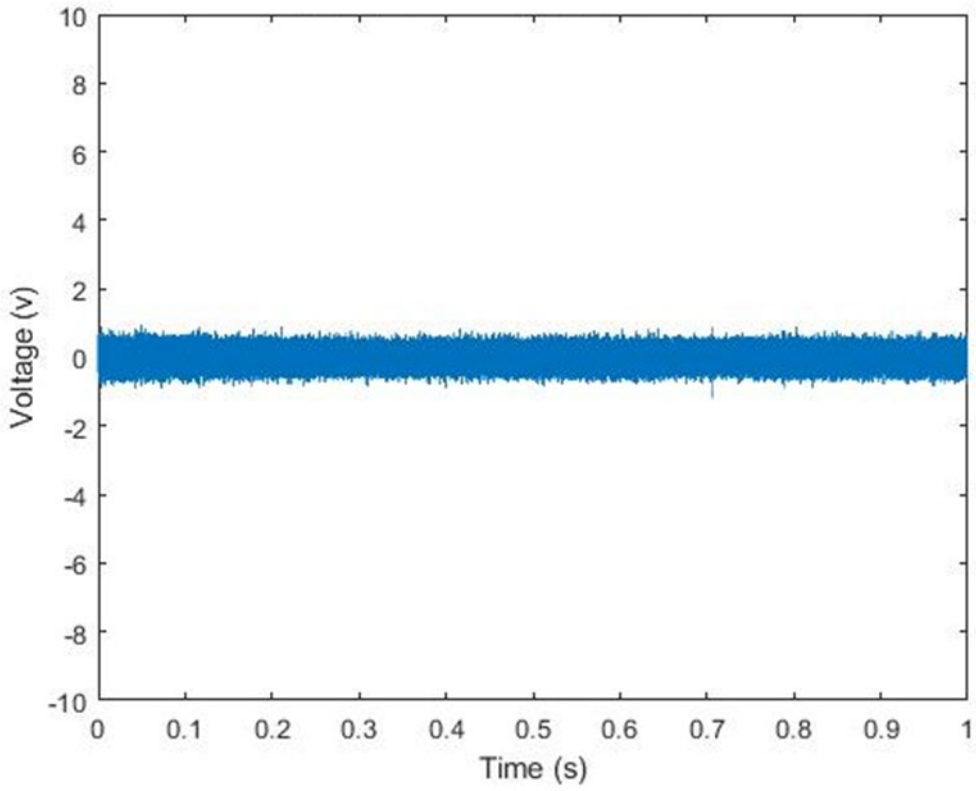

Figure 5.13: This figure shows the voltage vs. time plot of data collected in construction sand traveling 0.44 m/s at a depth of 0.1 m.

It is standard practice to determine a threshold voltage at which an AE count is differentiated from the background signal (Villet et al., 1981). However, in this application, this method would have caused unnecessary information loss. It was demonstrated with the average voltage vs. speed model that there was a correlation between the average voltage, which represents the background signal, and the testing parameters. Due to this correlation, if the threshold was parameterized for all experiments it may not properly reveal the number of counts based on a different run speed. To prevent this information loss, a new analysis method is proposed which aims to characterize the variability given different trial parameters.

This method first calculates the mean and standard deviation of the absolute value of the voltage. Then the number of points that lie between each positive standard deviation are calculated. Only positive values are used because the information stored in the negative standard deviations

are always part of background signal. This is deduced because the mean value in all measurements is very small ($\sim 0.2\ v$) and all values of voltage are positive. Therefore, only voltage values less than around 0.2 volts are represented in the negative standard deviations. Since these values are so small, no meaningful information is added to the distribution of the counts. From these data a plot is generated where the total number of measurements in a given standard deviation are graphed against their corresponding standard deviation from the mean of the signal.

In the full view of the plots, the data seem to follow a similar distribution as seen in Fig. 5.14. However, if only the peak variations are examined, these distributions appear very different (Fig. 5.15). The loam replications demonstrated considerably higher peak levels of variation than the construction sand counterparts. To quantify this difference, an index was created which will be referred to as the acoustic emission counts index (AECI). The AECI score for each replication was calculated by taking the average standard deviation level of the 10 AE counts furthest from the mean, where 10 is an arbitrary number. The AECI scores for three replications in loam and three in construction sand are represented in table 5.6. The Matlab script used to calculate the AECI is located in appendix C.

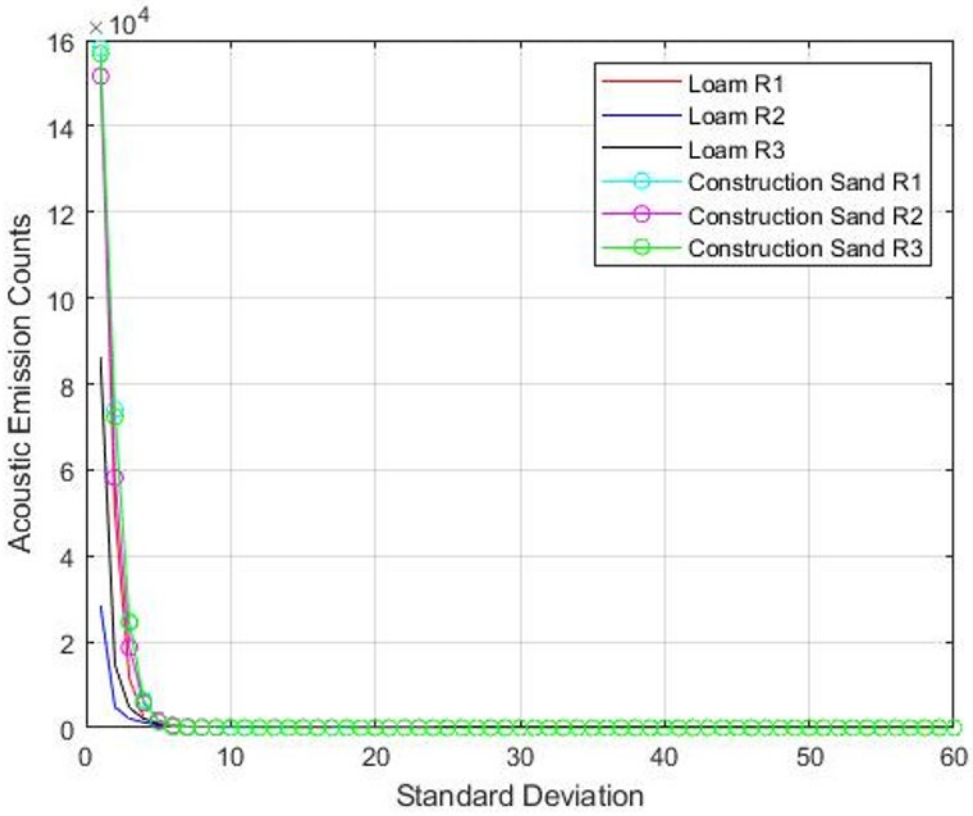

Figure 5.14: This graph shows the full range of the AE counts vs. the corresponding standard deviation for three replications in loam and three replications in construction sand.

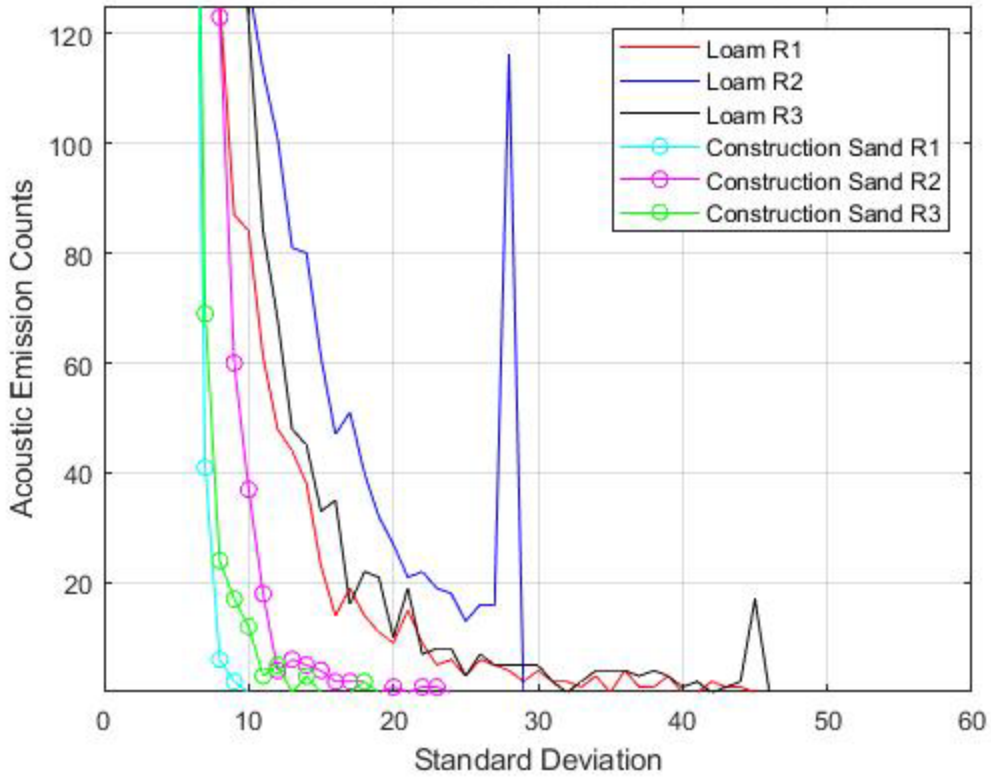

Figure 5.15: This graph shows a limited range of the number of AE counts vs. the corresponding standard deviation for three replications in loam and three replications in construction sand. This limited range provides insight to the peak variability of the measurements. Note: The peak in loam R2 only signifies many large AE counts had the same standard deviation.

Table 5.6: This table shows the AECI score per soil texture and replication of data taken in loam and construction sand.

Measurement	AECI Score
Loam R1	45.8
Loam R2	28.02
Loam R3	40.49
Construction Sand R1	13.8
Construction Sand R2	7.45
Construction Sand R3	11.23

Based on the large difference in average AECI score, it was decided that investigation into the root cause of the apparent difference was necessary. It was hypothesized that both texture and

compaction had an effect on the count index. To validate this hypothesis, two further tests were completed, one test to differentiate texture and another differentiate compaction.

For the texture differentiation samples gathered in the indoor soil bin from Fairmount sand and river sand, which measured similar compaction levels, were assessed for their AECI score (Table 5.7). The population distribution of these indices were then tested for similarity using the Kruskal-Wallace test. The test was chosen for the same reasons specified in chapter 5.2 related to the few assumptions necessary to carry out the test. The null hypothesis of the test, being that all groups tested come from the same distribution, was tested against the alternative that the groups are not from the same distribution. At an α of 0.01, the null hypothesis was rejected leading to the conclusion that there exists a different population distribution of AECI scores between the river sand and the Fairmount sand (Table 5.8).

Table 5.7 This table shows the AECI score per soil texture and replication of data taken in river sand and Fairmount sand.

Measurement	AECI Score
River Sand R1	8.2
River Sand R2	17.47
River Sand R3	13.23
River Sand R4	16.2
River Sand R5	26.3
River Sand R6	10.7
River Sand R7	12.15
River Sand R8	8.77
River Sand R9	9.5
River Sand R10	18.4
Fairmount Sand R1	8.05
Fairmount Sand R2	8.2
Fairmount Sand R3	8.1
Fairmount Sand R4	7.6
Fairmount Sand R5	7.4
Fairmount Sand R6	8
Fairmount Sand R7	7.2
Fairmount Sand R8	7.9
Fairmount Sand R9	7.8
Fairmount Sand R10	7.8

Table 5.8: This table shows the statistical summary of the Kruskal Wallis test for a difference in population distribution of the AECI score between Fairmount sand and river sand.

Source	SS	df	MS	Chi-sq	Prob>Chi-sq
Columns	490.05	1	490.06	14.02	0.0002
Error	173.95	18	9.664		
Total	664	19			

The effect of compaction was now analyzed using the compaction data discussed in section 5.2. The AECI score was calculated for the eight runs in high compaction and the 8 runs in low compaction (Table 5.9). The K-W test was again used for reasons previously stated to access the possible difference in population distribution (Table. 5.10). An α of 0.05 fails to reject the null

hypothesis indicating there is no difference among the population distribution AECI scores of the highly compacted loam and the loam with little compaction. These results are consistent with the results of Naderi-Boldaji et al. who showed little correlation between the AE counts and the bulk density of loam using the threshold approach for determining the AE counts (Naderi-Boldaji, Tekeste, Nordstorm, Barnard, & Birrell, 2018).

Table 5.9: This table shows the AECI score per replication of the two soil compaction groups from data taken in a loam soil.

Measurement	AECI Score
High Compaction Loam R1	29.15
High Compaction Loam R2	34
High Compaction Loam R3	42.19
High Compaction Loam R4	61
High Compaction Loam R5	45.8
High Compaction Loam R6	28
High Compaction Loam R7	42.67
High Compaction Loam R8	52
Low Compaction Loam R1	53
Low Compaction Loam R2	31
Low Compaction Loam R3	48
Low Compaction Loam R4	55
Low Compaction Loam R5	46
Low Compaction Loam R6	47
Low Compaction Loam R7	40.1
Low Compaction Loam R8	42.588

Table 5.10: This table shows the statistical summary of the Kruskal Wallis test for differences in population distribution of the AECI score between highly compacted loam and loam with little compaction.

Source	SS	df	MS	Chi-sq	Prob>Chi-sq
Columns	20.25	1	490.06	20.05	0.3446
Error	319.75	14	9.664	22.83	
Total	340	15			

5.6 Frequency Domain Analysis

All data for use in frequency domain analysis was ran through a band pass filter in Matlab prior to analysis retaining the range of 50 kHz to 250 kHz. Using the Welch's power spectral density (PSD) estimate initial frequency distributions were created for visual inspection. The Welch's PSD computes a frequency spectrum through first segmenting the time series into blocks. Then a windowed discrete Fourier transform is computed followed by calculation of the modified periodogram value. The periodogram values are then averaged to obtain the PSD estimate (Solomon, 1991). This estimate used a segment length of 1000 measurements and 100 points of overlap. The initial hypothesis related to the frequency spectra stated that, if the soil texture was varied, there would be a response seen in the frequency spectrum. After initial visual inspection, the frequency distributions appeared remarkably similar (Fig 5.16, 5.17, 5.18, 5.19). These spectra represent data from 4 different soil textures recorded at identical depths and speeds.

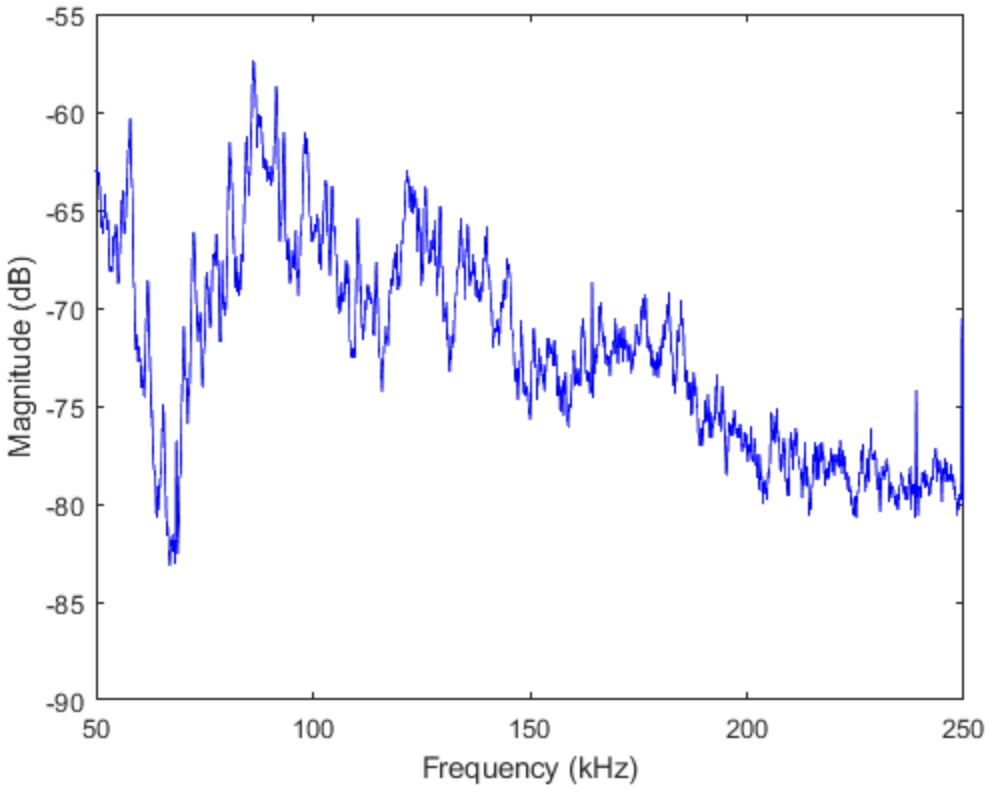

Figure 5.16: Welch's PSD estimate of data taken in construction sand.

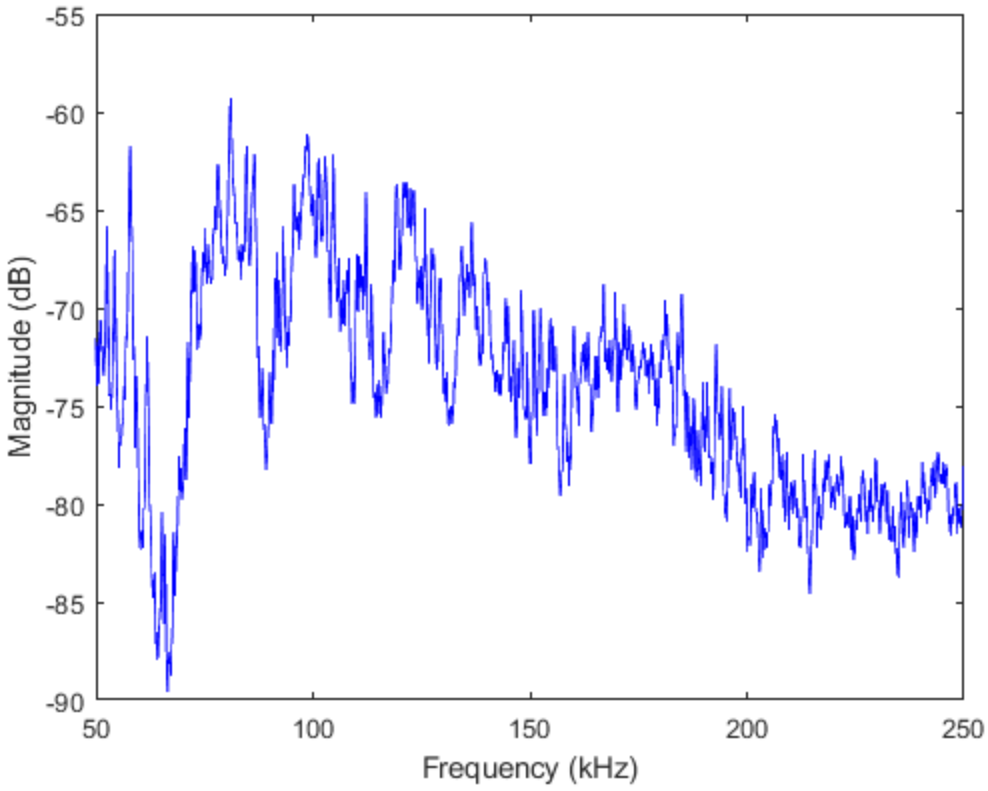

Figure 5.17: Welch's PSD estimate of data taken in Fairmount sand.

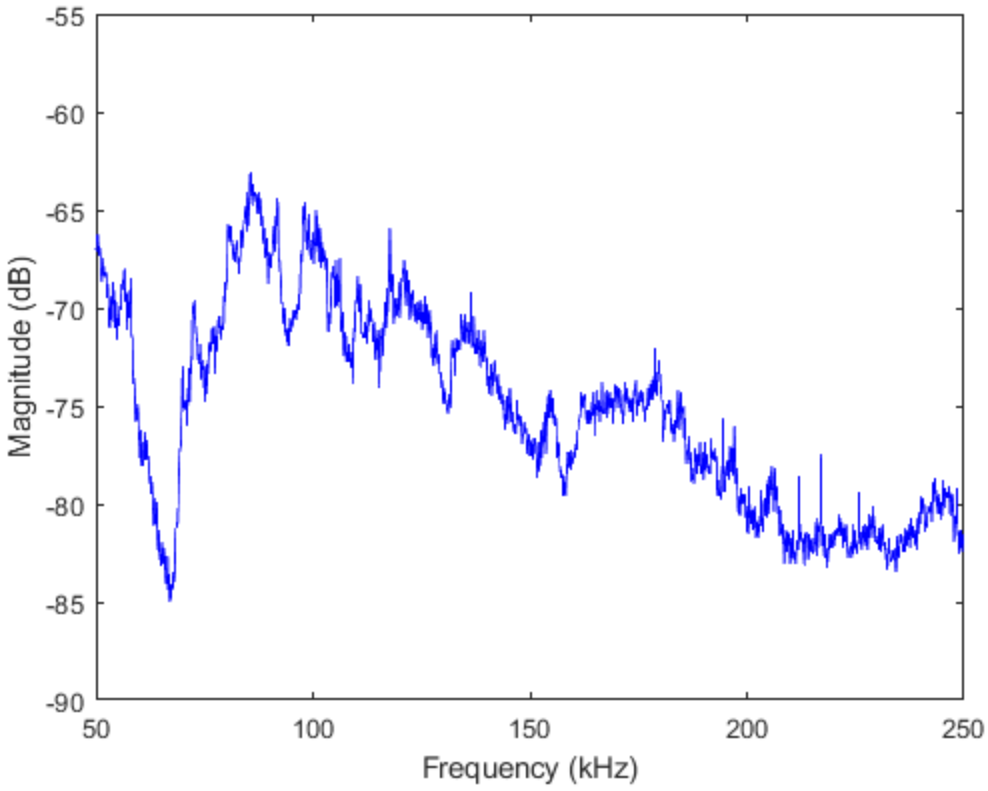

Figure 5.18: Welch's PSD estimate of data taken in loam soil.

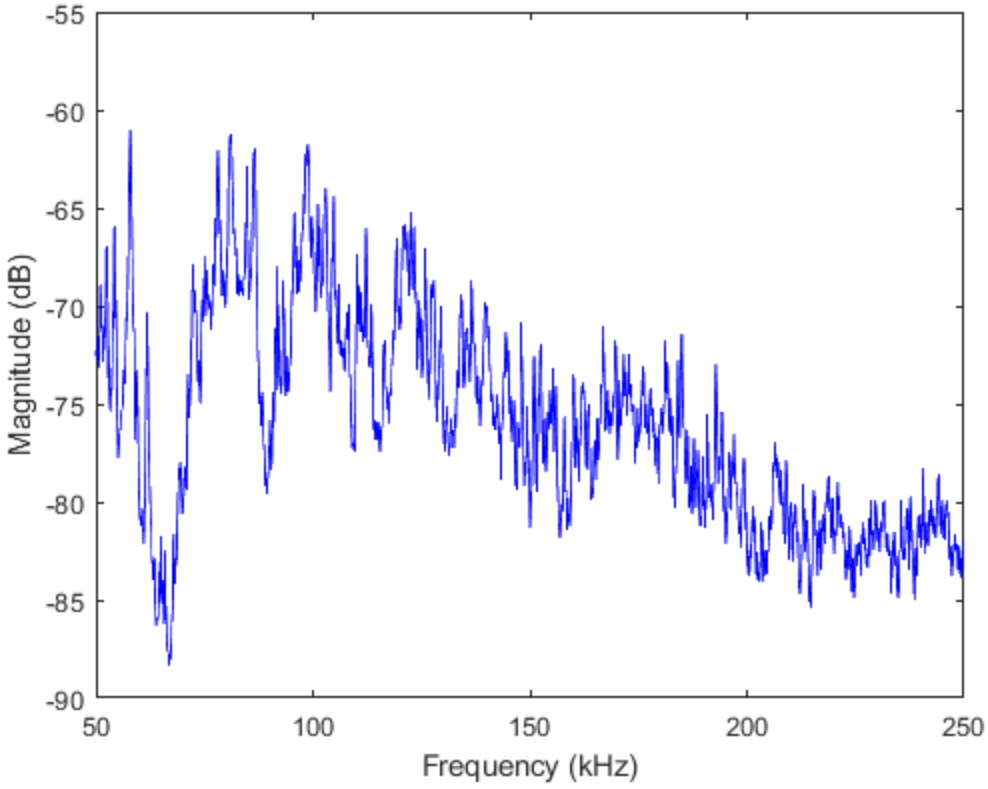

Figure 5.19: Welch's PSD estimate of data taken in river sand.

Due to little visual difference between the spectra a conjecture is made that the AESW geometry plays a large role in the distribution of the frequency spectra while the wedge-soil interaction has an additional lesser effect. Since resources were only available for one AESW this conjecture was not tested. To capture these minor differences many analysis techniques were explored. The first technique utilized Matlab's wavelet toolbox. Wavelet analysis differs from the classic Fourier analysis in the method used to characterize the waveform. In Fourier analysis a periodic waveform is defined in terms of trigonometric functions which are continuous (Davis, 1989). Alternatively, in wavelet analysis waveforms are defined as a load of wavelets which are rapidly decaying wave-like oscillations with zero mean (Chiann & Morettin, 1998) (Chui, 1992). Wavelets are discrete in time and frequency and take on many different functional forms such as

Morlet, Symlets, Coiflets, etc. A select functional form may then be shifted and scaled across the time series to determine the wavelet coefficients that best represent the waveform. Wavelets are a better tool for analysis of real world data because, due to their discrete nature, the basis functions better depict abrupt changes in the time series. They also allow for the spectra to be easily analyzed when representing the frequency, magnitude, and time simultaneously compared to its Fourier domain counterpart. The functional form of the wavelet is chosen based on the time series under analysis. The analysis depicted in this thesis explored the three standard wavelet functional forms applied to the voltage vs. time signal from the acoustic emission sensor. These functional forms are named bump, Morse, and Morlet. The bump and Morse functional forms are used to create magnitude scaleograms for a single sample. The Morlet functional form is used in the creation of wavelet coherence plots which are comparisons of two similar samples. Figures 5.20 and 5.21 represent a magnitude scaleogram for data taken in loam soil using the bump and Morse wavelets respectively.

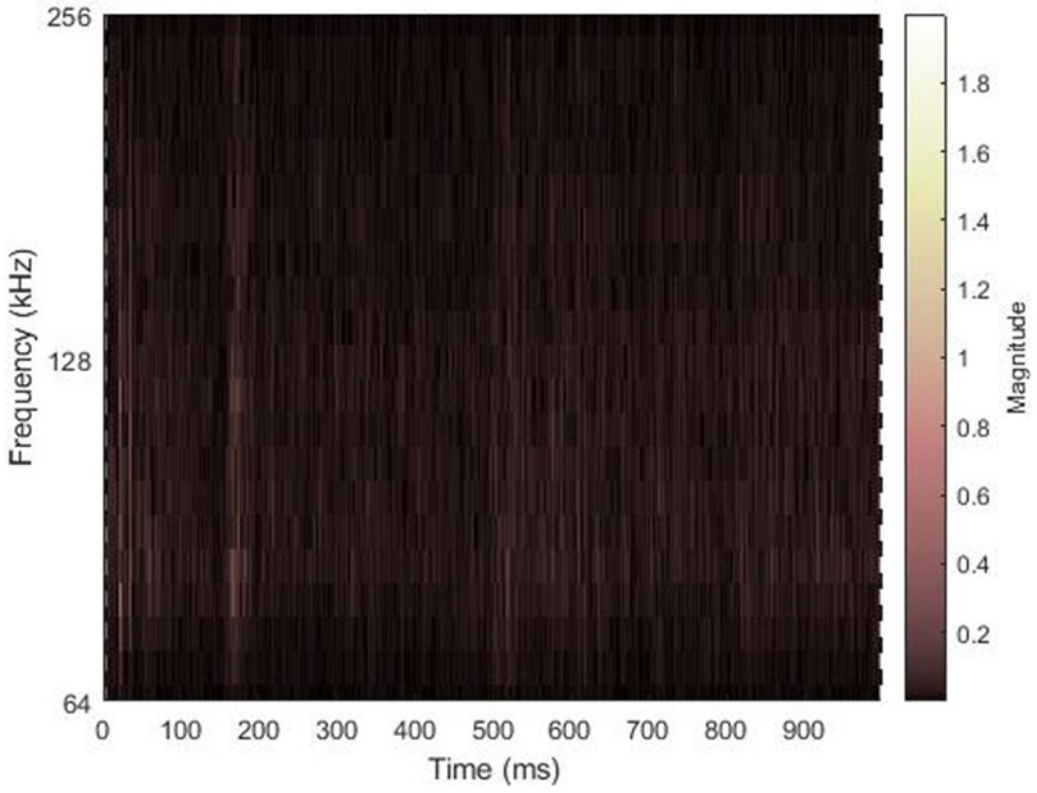

Figure 5.20: The magnitude scaleogram shown used bump wavelets to characterize the frequency spectrum as a function of time for data collected in loam soil. This allows for investigation into how changes in the time series data affect the frequency distribution.

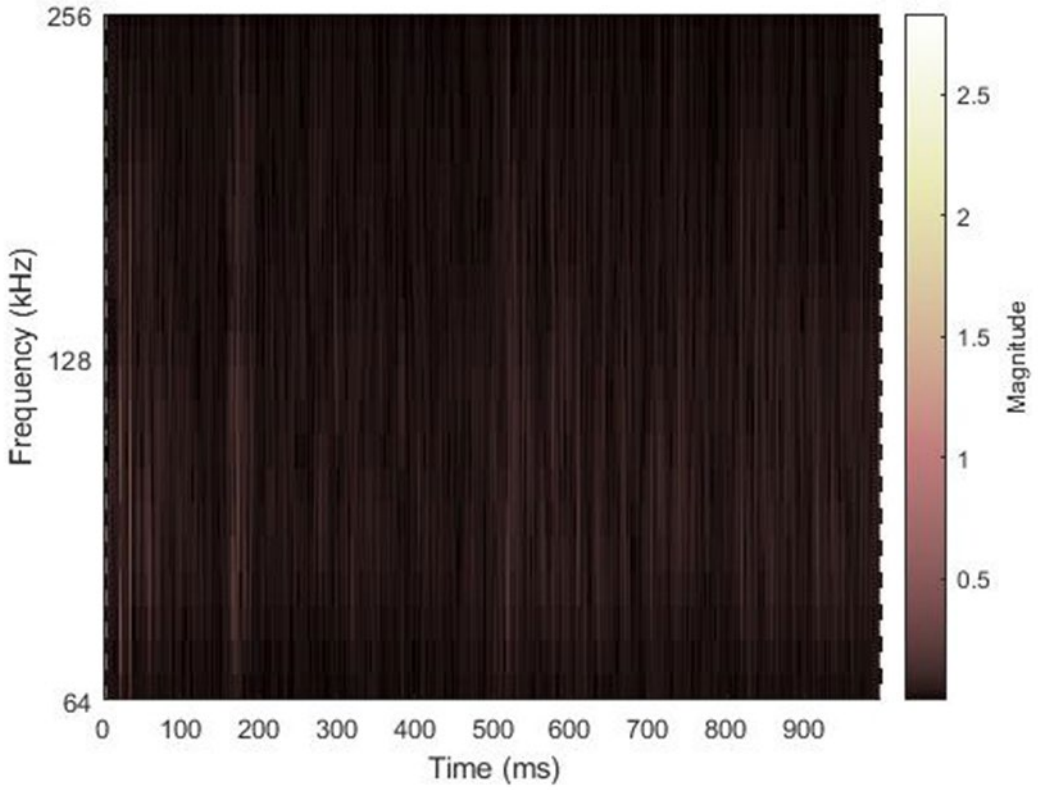

Figure 5.21: The magnitude scaleogram shown used Morse wavelets to characterize the frequency spectrum as a function of time for data collected in loam soil. The peaks in the frequency spectrum are poorly displayed compared to Fig. 5.20.

Comparing these figures with their corresponding Welch's PSD it was decided that the bump wavelet best characterizes the sample. This justification is intuitive as the bump wavelet is designed to characterize signals showing a wider level of variance in the time series compared to the frequency spectrum. Also the bump wavelet more clearly characterized the spikes seen around 60 kHz and 90 kHz than did the Morse wavelet. Comparing the magnitude scaleogram and time series (Fig. 5.22) it can be seen that the acoustic emission counts in the time series are causing a magnitude increase in the frequency domain. These increases appear to lift the magnitude of the entire spectrum roughly proportional to the values displayed in the Welch's PSD (Fig. 5.18). This phenomena was further examined by creating a similar plot using a moving average Fourier transform. In this plot an initial block 1000 measurements of the time series was created.

Subsequent blocks contained 500 measurements from the block before and 500 measurements from the block after. The first 250 measurements and last 750 measurements in the time series were discarded as no complete average could be solved for. A frequency distribution using the Fast Fourier Transform (FFT) was created for each bock of measurements. The Matlab script for the moving average FFT is located in appendix D. With the tractor and implement moving at a speed of 0.44 m/s a frequency spectrum is created for every 0.44 mm of travel. These data were then used to create a mesh plot containing the frequency, magnitude, and time (Fig. 5.23).

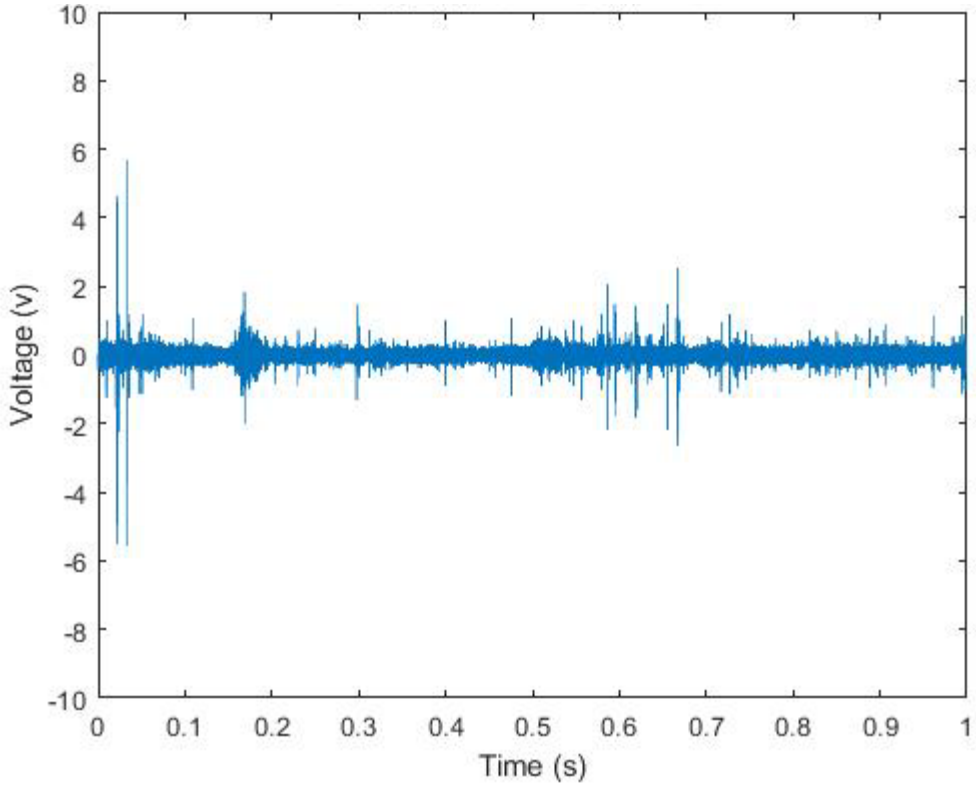

Figure 5.22: Voltage vs. time series of data collected in a loam soil for 1 second at 0.44 m/s. In comparison with Fig. 5.20 it appears the spikes in voltage cause spikes in the magnitude of the frequency spectrum.

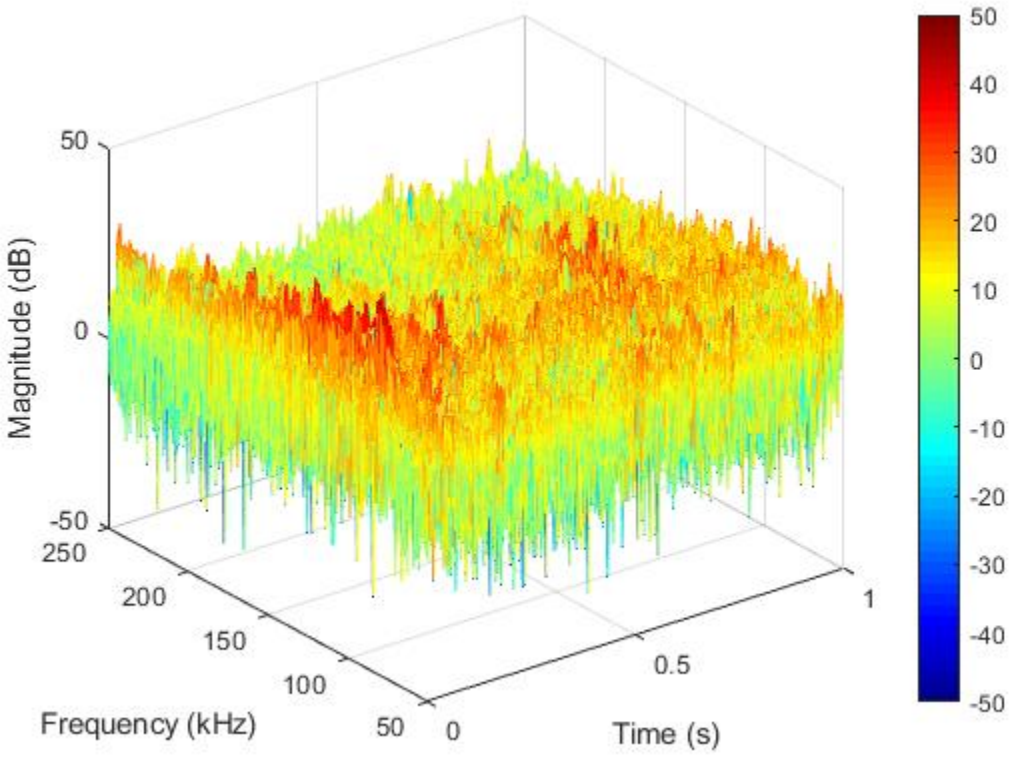

Figure 5.23: Moving average FFT of data taken in loam soil. Similar to the magnitude scaleogram this allows for depiction of how the time series affects the frequency distribution.

Analysis of the moving average FFT in loam also shows the acoustic emission counts causing an offset in the magnitude of the frequency spectrum. Figure 5.23 shows the increased magnitude is roughly proportional to the magnitudes representation in the overall signal. However, there are some time blocks where it appears the frequency spectra differs slightly. The three different sand textures were also analyzed using the methods displayed above. The construction sand will serve as the example in this chapter and all other figures are located in the appendix (E). Figures 5.24, 5.25, and 5.26 represent the moving average FFT, magnitude scaleogram, and voltage vs. time series respectively. The moving average FFT plot appears to represent a very uniform frequency distribution as a function of time. This lends evidence to the root cause of the spikes seen in the

moving average FFT. This is evident as there are very few AE counts in the time series of the construction sand and very few peaks in magnitude of the frequency distribution.

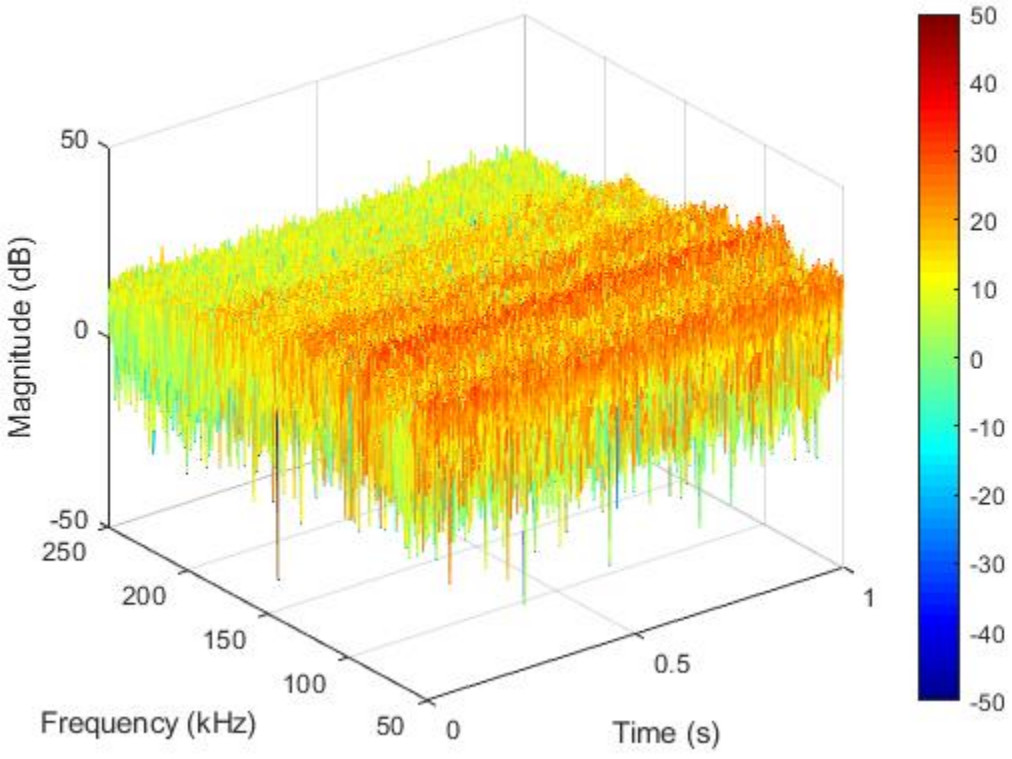

Figure 5.24: Moving average FFT of data taken in construction sand. An important feature of this plot is the lack of variability in magnitude given the lack of variability in the time series (Fig. 5.26).

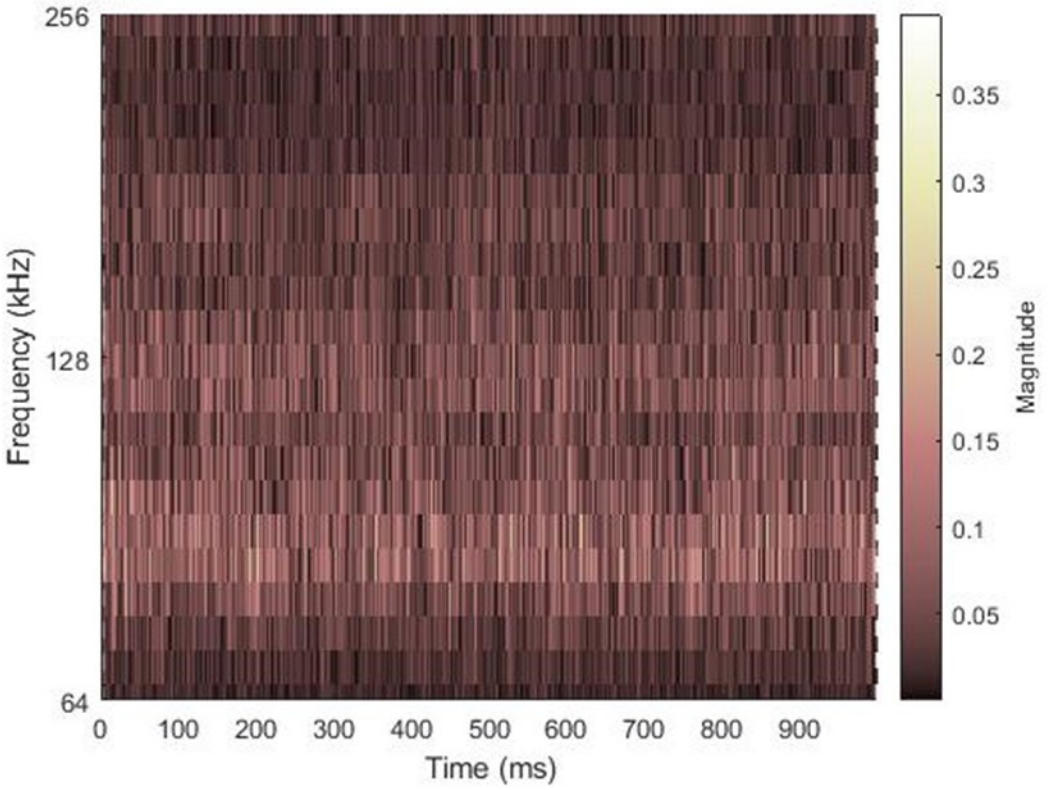

Figure 5.25: The magnitude scaleogram shown used bump wavelets to characterize the frequency spectrum as a function of time for data collected in construction sand.

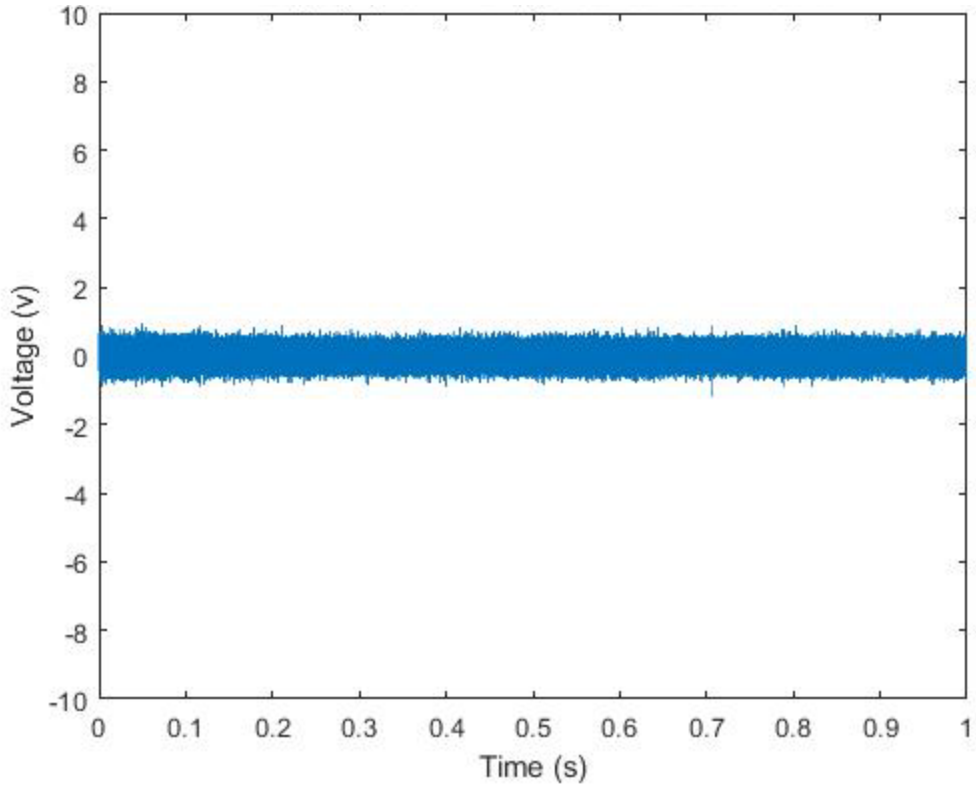

Figure 5.26: This figure shows the voltage vs. time series of data taken in construction sand. In comparison with Fig. 5.24 and 5.25 it appears that a uniform signal in the time domain results in a uniform distribution of magnitude to the frequency spectra as a function of time.

Wavelet coherence using the Morlet wavelet was also analyzed to determine if there were any similarities between the frequency spectra as a function of time. The time series from two replications of construction sand are used to create the coherence plots in Fig. 5.27 and Fig. 5.28 represents loam vs. construction sand. Fig. 5.27 shows that in replications of the same texture, the frequencies of the waveform do not cohere as a function of time. The plot representing the different textures (Fig. 5.28) shows the same results. Despite this lack of coherence as a function of time the frequency spectra of replications in the same texture provide a nearly identical frequency distribution (Fig. 5.29).

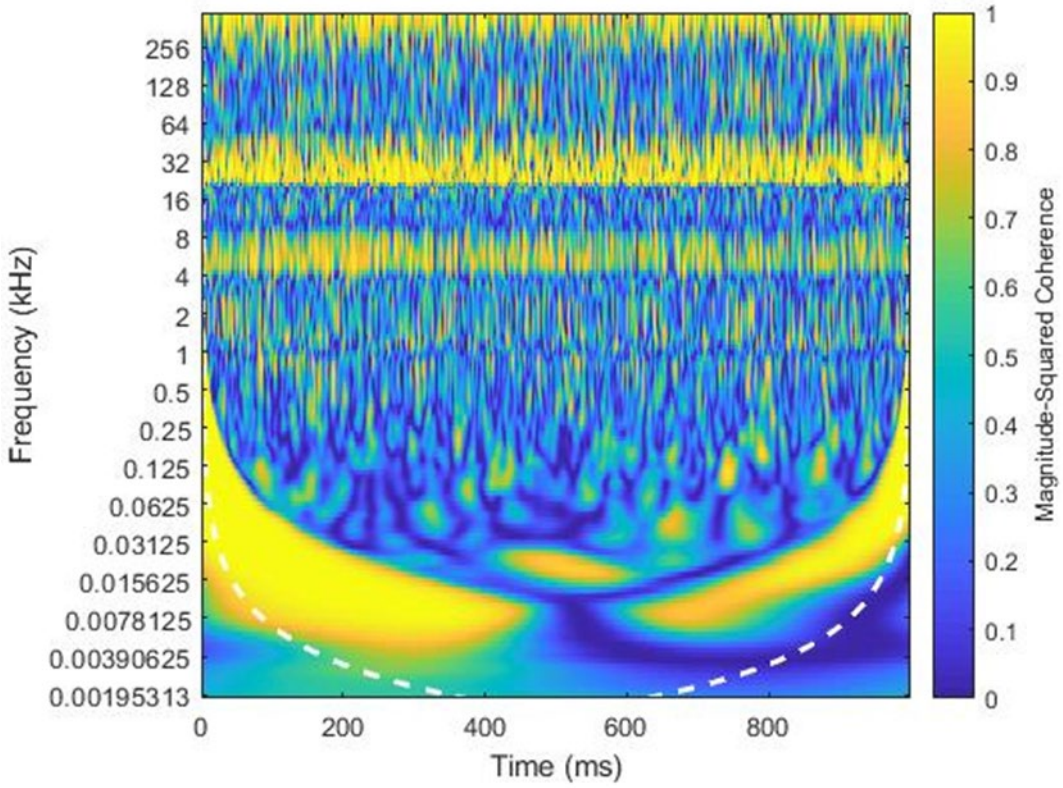

Figure 5.27: This figure shows the wavelet coherence between two replications of construction sand. It can be seen that the two replications have very low frequency domain coherence as a function of time. Note: There is strong coherence above 250 kHz and below 50 kHz due to the bandpass filter.

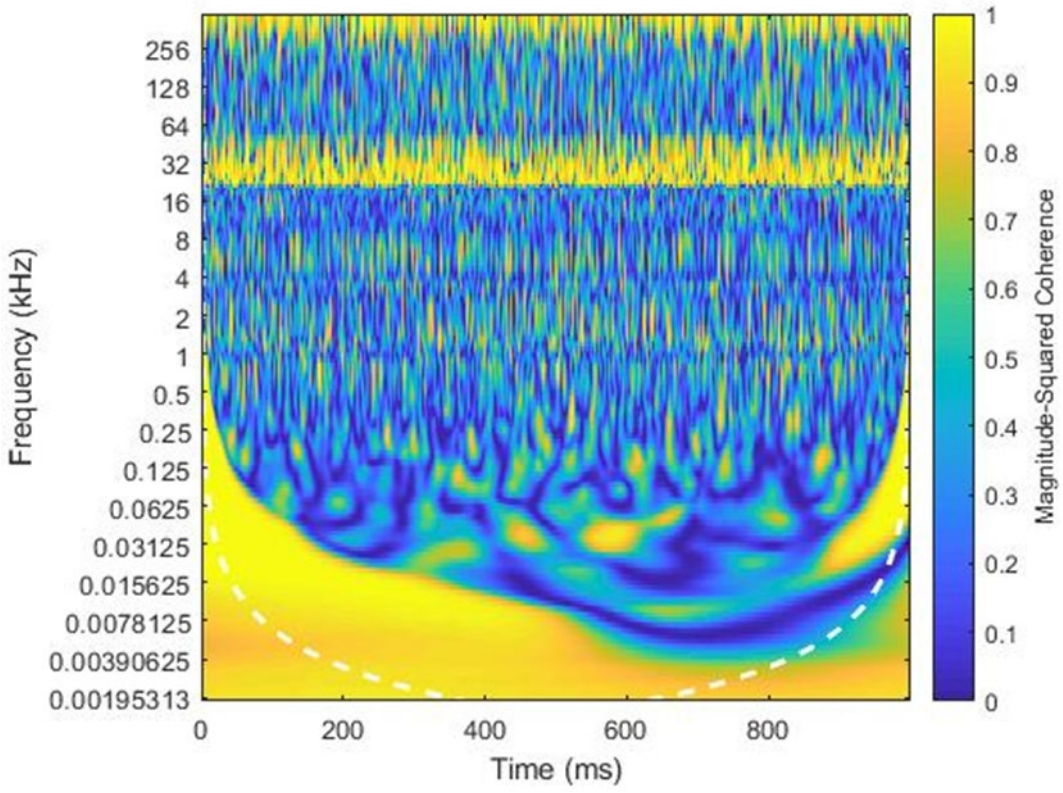

Figure 5.28: This figure shows the wavelet coherence between one replication of construction sand and one of loam soil. It can be seen that the two replications have very low frequency domain coherence as a function of time. Note: There is strong coherence above 250 kHz and below 50 kHz due to the bandpass filter.

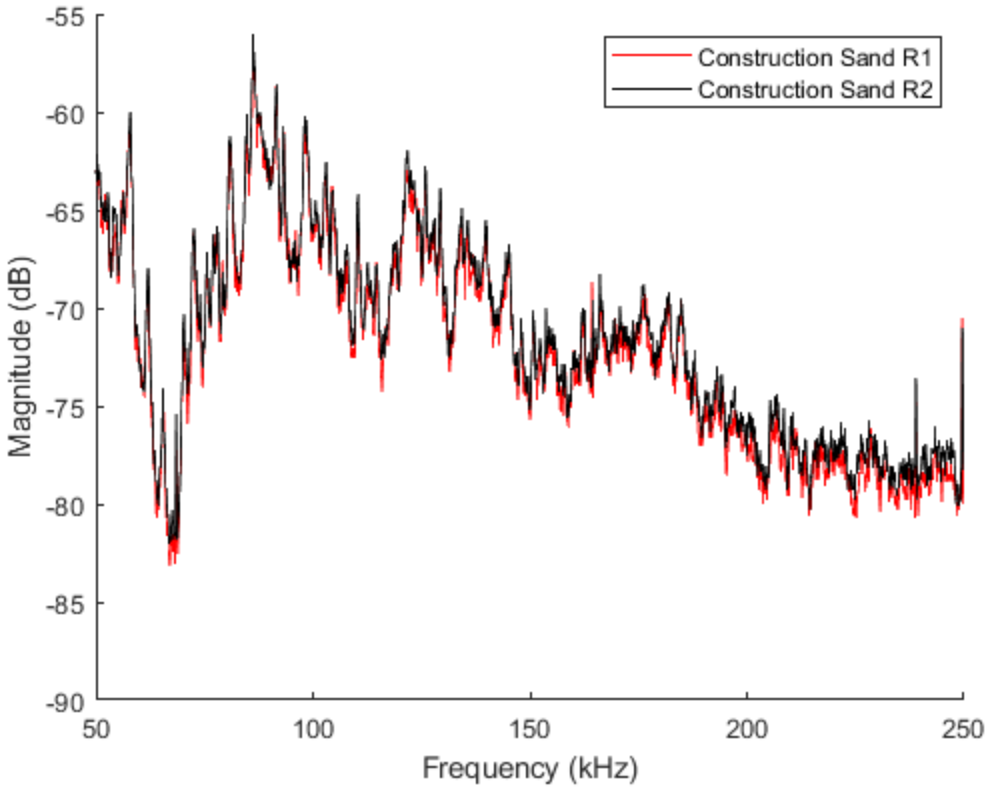

Figure 5.29: This graph shows a magnitude vs. frequency comparison using Welch's PSD method for two replications of construction sand.

However, between different textures, the level of the magnitude offset and general spectrum show some variation (Fig. 30). This variation in magnitude is hypothesized to be caused by the force necessary to drag the AESW through the soil. The force difference is quantified in different aspects of the signal such as average voltage (5.1) and signal energy (5.2). Naderi-Boldaji et al. also displayed that sandy soils had significantly higher levels of counts as the bulk density was increased (Naderi-Boldaji et al., 2018). Therefore, the possibility exists that the acoustic emission counts have some correlation with bulk density despite the results shown in section 5.5. Also, despite the extremely uniform distributions of particle size in the sand experiments, the level of AE counts are changing as a function of time. If the sole root cause of the counts were the particle size the level of AE counts should be constant given a uniform texture throughout the experiment.

This principle also lends evidence against the statistical conclusions of section 5.5. If such a correlation exists between AE counts and bulk density, the AE counts may represent another aspect of the signal related to the force necessary to drag the AESW through the soil. Due to this, if the raw frequency data is analyzed there will be an offset in magnitude stemming from the required force and not the textures (Fig. 5.30). This offset arises as the voltage level in the time series is a coefficient of the basis functions in a Fourier transform (Davis, 1989). To evaluate the frequency spectrum between the different textures, the effects of the required force must be factored out of the frequency spectrum to prevent a multifactor influence. The method proposed to prevent this influence is to use the z-score normalization method on frequency spectrum calculated using Welch's PSD estimate. The z-score represents every measurement as a signed standard deviation from the mean of the observed data (Sullivan, 2010). An excerpt of the frequency spectrum using the z-score normalization method is shown in Fig. 5.31. This figure appears to show a reduced level of overall magnitude between spectra but still displays differences in peaks between the textures. The replications of the same texture also appear to maintain strong levels of self-similarity.

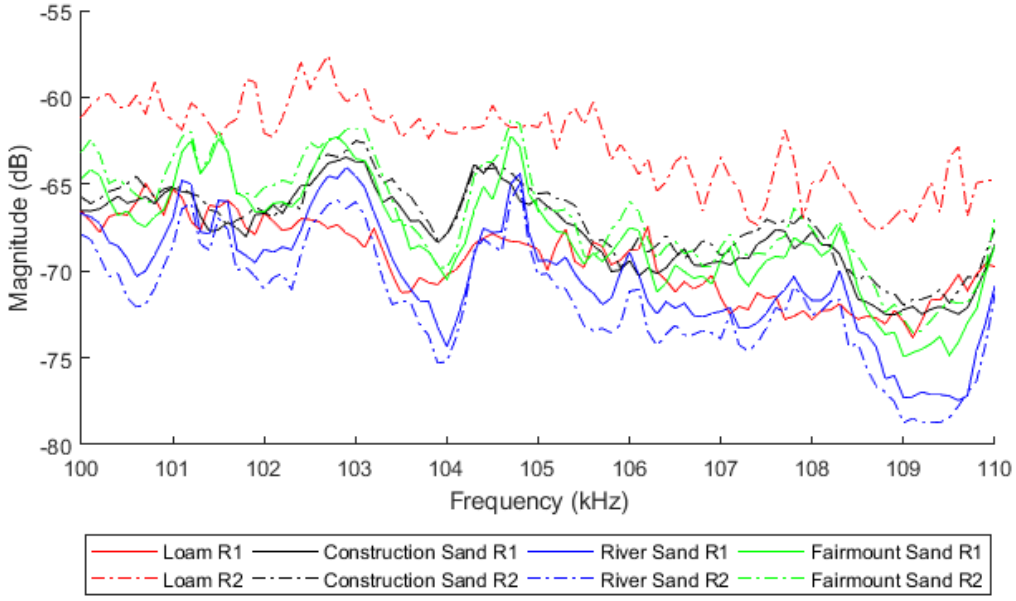

Figure 5.30: This figure shows the Welch's PSD estimate for two replications in each of the four textures. Note: The frequency range is only 100-110 kHz for visual purposes.

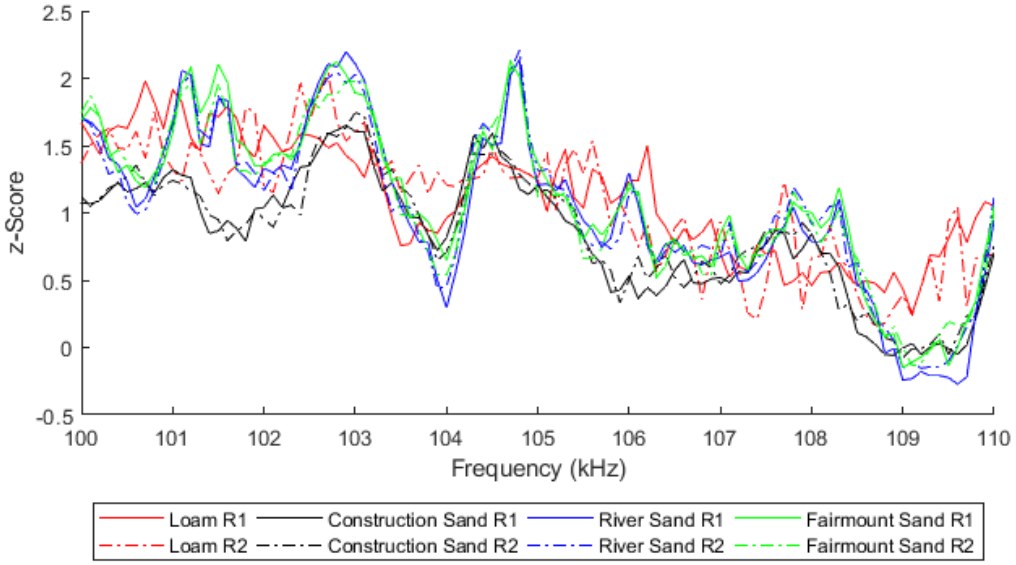

Figure 5.31: This figure shows the z-score of the Welch's PSD estimate for two replications in each of the four textures. Note: The frequency range is only 100-110 kHz for visual purposes.

5.7 Principal Component Analysis

Based upon the filtered Welch's PSD estimates, a principal component analysis (PCA) was used to distinguish soil textures based on their frequency spectra. The PCA was completed using Matlab for data formatting and SAS for analysis (SAS 9.4®: SAS Institute Inc.: Cary, NC). A PCA was chosen due to its ability to reduce the dimensionality of datasets. The method reduces these dimensions through finding a small number of linear orthogonal sets, named principal components, of the original variables with the largest variance. In this technique, the first few principal components (PC's) may account for much of the variation in the data set therefore, PC's past the first two may be disregarded with little loss of information. This dimension reduction makes the PCA a useful technique for characterizing systems represented by large datasets (Johnson, 1998). Two initial analyses were completed using the even frequency bins from the Welch spectrum. The spectra were reduced before the PCA to decrease the computational power required for the test. Five replications of the four textures sampled were used in the analysis creating 20 observations with each frequency bin (1,000) acting as an independent variable. One analysis was completed using the frequency distributions and another with the z-scores of said distributions. It can be seen in Fig. 5.32 that the analysis on the Welch distribution incorrectly classified the textures and also displayed poor self-similarity between the replications of a given texture. In this analysis, 90.6% of the variation was explained in the first two principal components (Table 5.10). In the analysis on the z-scores, all texture classes have a high degree of spatial separation and the sands represent a high level of self-similarity (Fig. 33). The loam shows much less self-similarity but is clearly distinguishable from the other textures. The first two PC's sum to capture 55.89% of the variation in the dataset (Table 5.10). A third PCA was completed on the 200 highest loadings from the z-

score normalization (Fig. 5.34). This analysis yielded similar results to the full analysis with a higher percent explained of 74.52% in the first two principal components (Fig 5.10).

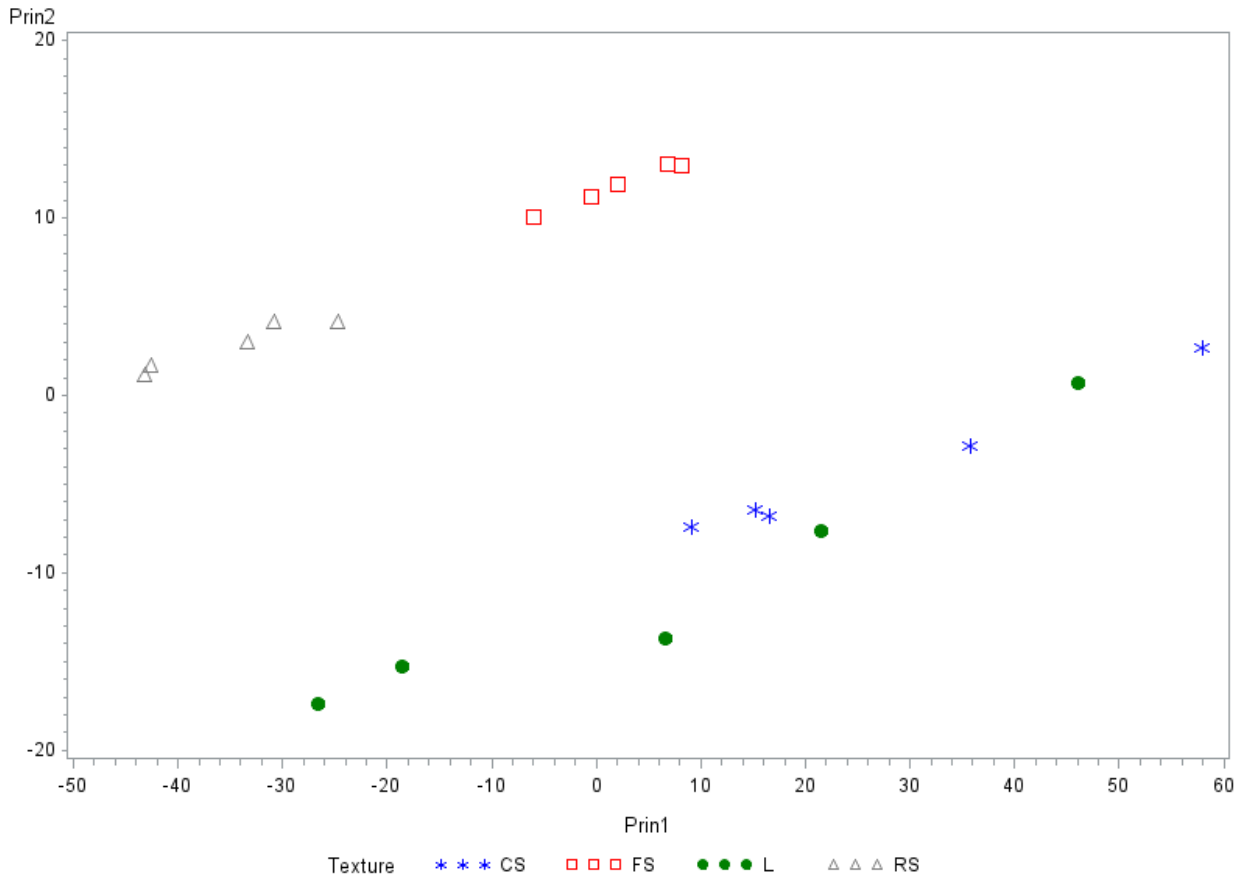

Figure 5.32: The PCA shown used the Welch distribution for five replications of CS, FS, L, and RS. The low spatial proximity between points of the same shape indicates the texture is not the cause of variability in this dataset.

Table 5.11: This table shows the percent of variance explained by the first 5 PC's for each data set analyzed. It can be seen that the first two components of each dataset represent a large amount of the variability.

	Welch	z-Score	Loadings
PC1	81.11%	38.67%	50.73%
PC2	8.95%	17.22%	23.79%
PC3	3.65%	11.63%	5.84%
PC4	1.98%	6.76%	4.43%
PC5	1.15%	6.64%	3.79%

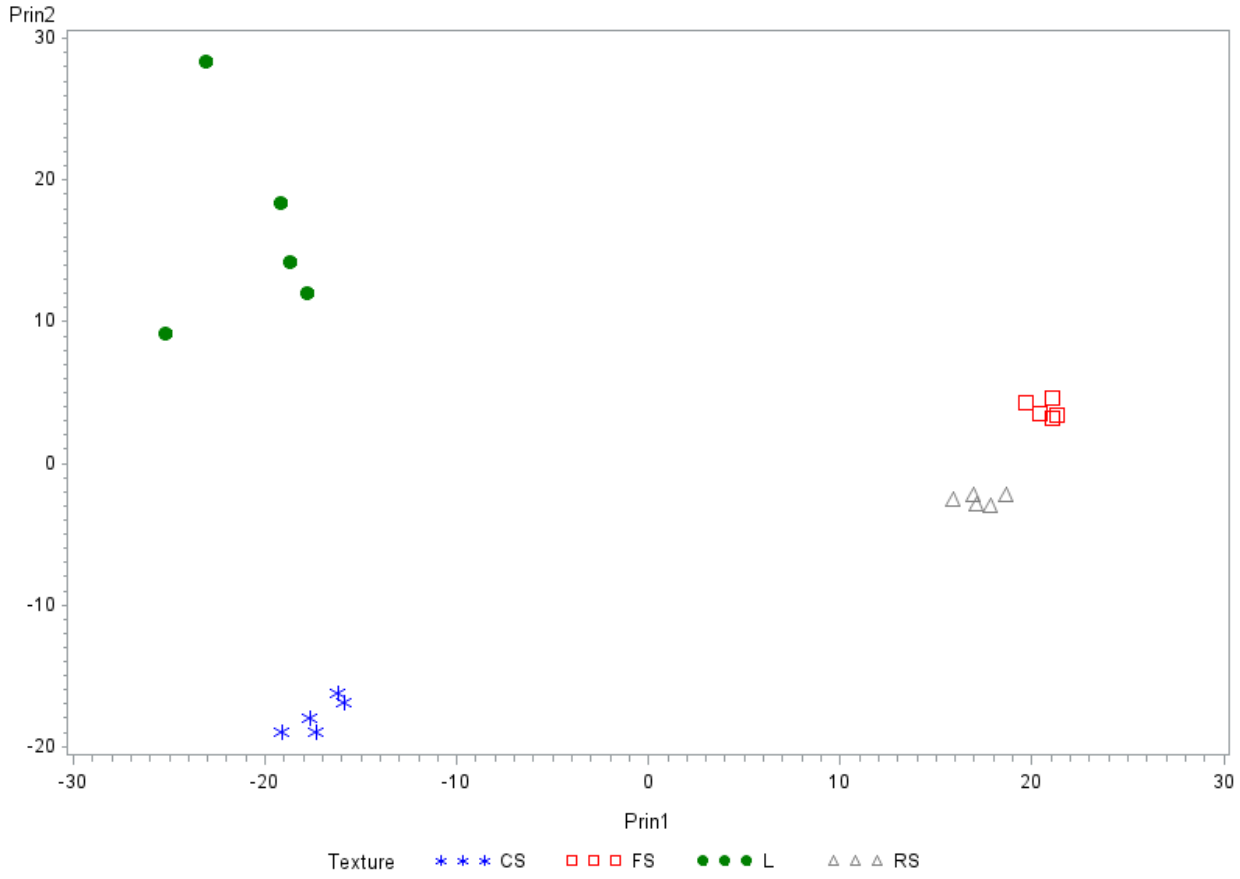

Figure 5.33: The PCA shown used the z-score normalization of the Welch distribution for five replications of CS, FS, L, and RS. The high spatial proximity between points of the same shape indicates the texture may be the cause of variability in this dataset.

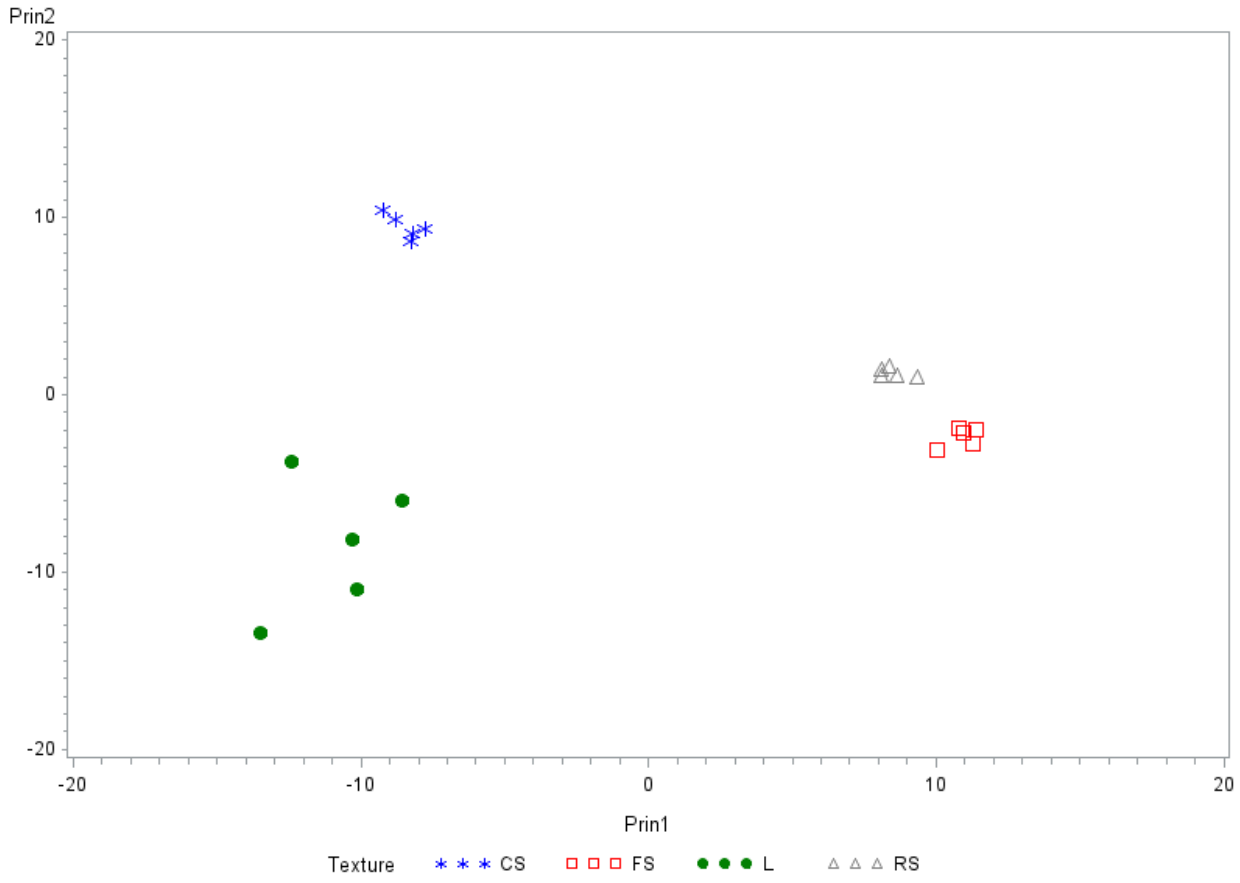

Figure 5.34: The PCA shown used the top 200 loadings from the z-score normalization of the Welch distribution for five replications of CS, FS, L, and RS. This indicates using the top loadings for reduction of the dataset my occur with little information loss.

A one-way analysis of variance (ANOVA) then took place on the first two principal components from the 200 highest loadings. In testing the underlying assumptions of the ANOVA model, it was found that the normality assumption held true, but the equality of population variances (homoscedasticity) was violated due to the loam texture. The normality assumption may be judged through the normal probability plots shown in Fig. 5.35 and 5.36 for PC1 and PC2 respectively. In these plots it appears there are few outliers, but generally the data adhere to the normal distribution line. Homoscedasticity was evaluated using the Brown and Forsythe's

Test for Homogeneity of Variance (BF test) (Brown & Forsythe, 1974) and box plots. The null hypothesis of the BF test states between groups the data have an equal population variance. At an α of 0.05 the null hypothesis is not rejected for PC1 but is rejected for PC2 with p-values of 0.09 and 0.0031 respectively. The box plots in Fig. 5.37 and 5.38 reveal that the variance of the loam texture is far greater than that of the sand textures. The variance of the loam is also far greater with respect to PC2 than PC1.

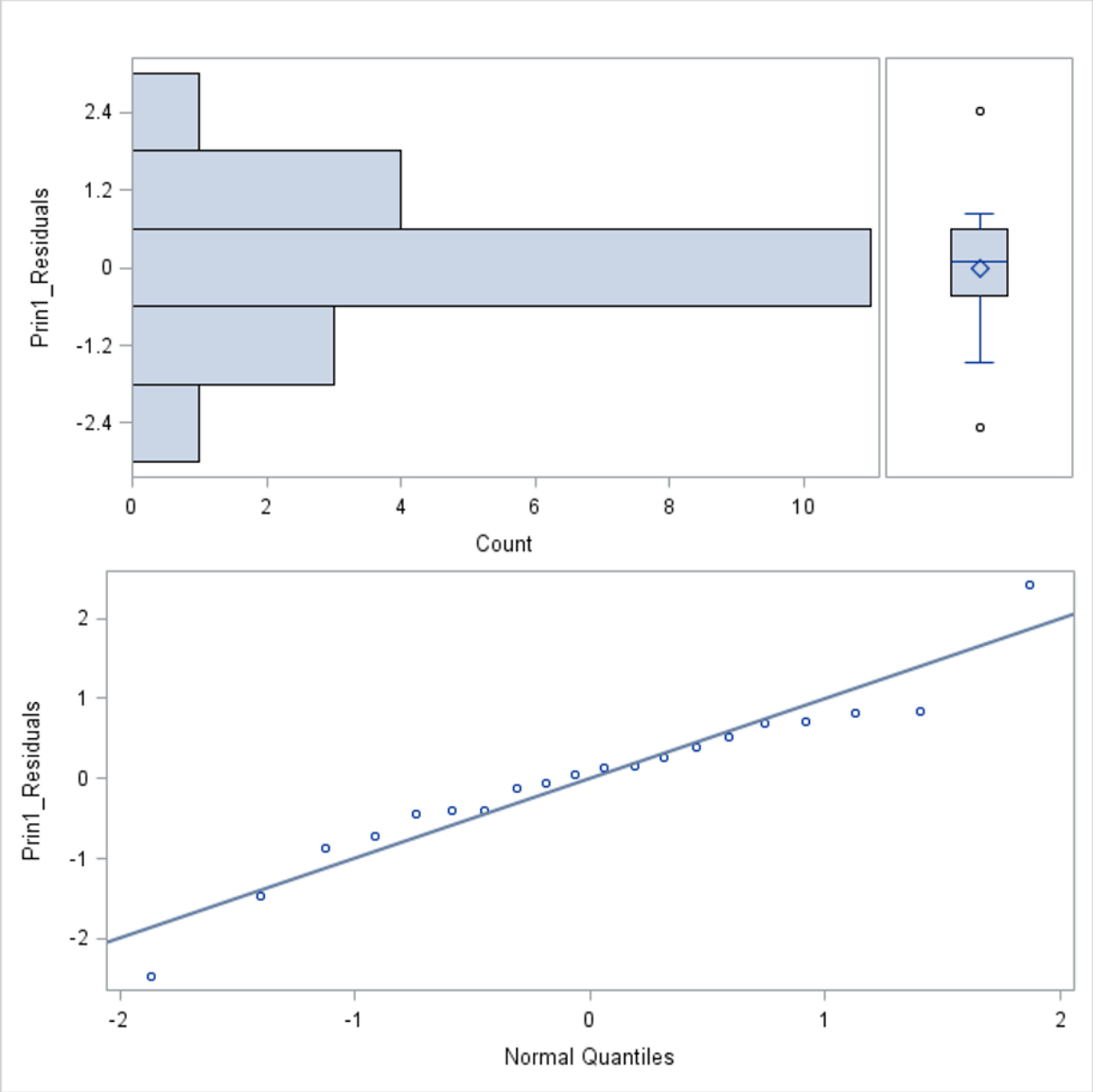

Figure 5.35: This figure shows a residuals histogram (upper) and normal probability plot of residuals (lower) for the first PC of the 200 highest loadings. The degree to which the dots follow the line on the bottom graph shows the level of normality for the residuals.

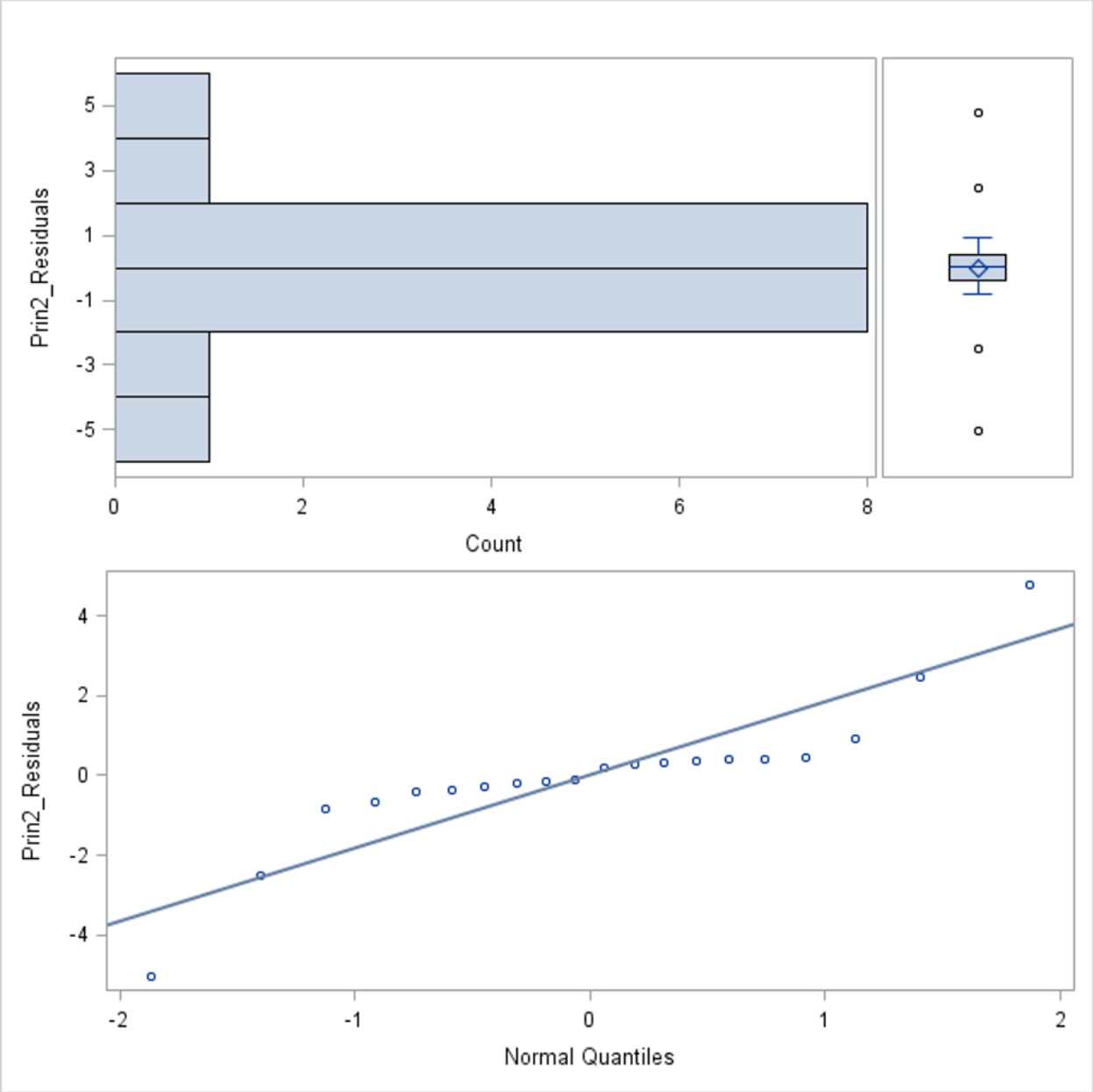

Figure 5.36: This figure shows a residuals histogram (upper) and normal probability plot of residuals (lower) for the second PC of the 200 highest loadings. The degree to which the dots follow the line on the bottom graph shows the level of normality for the residuals.

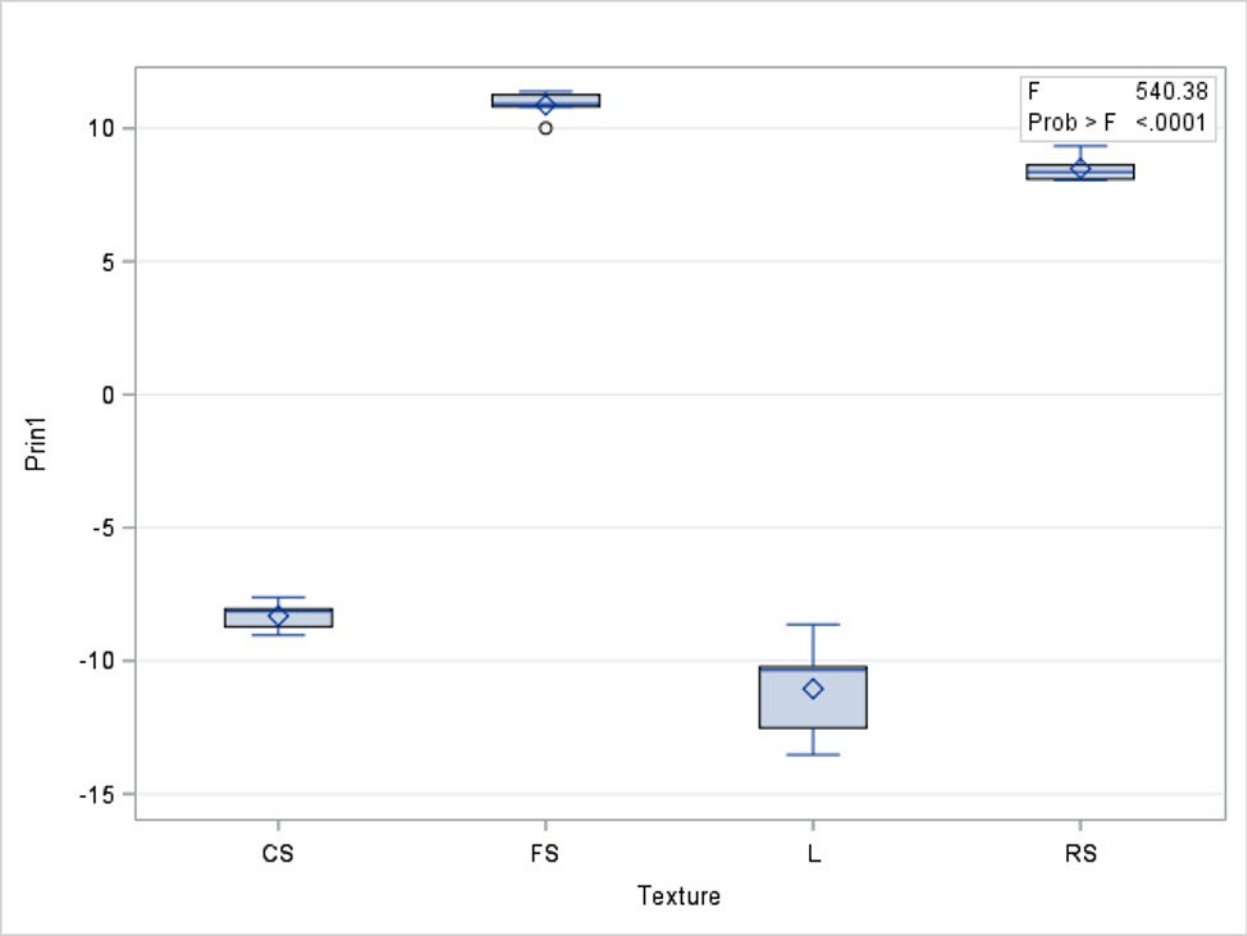

Figure 5.37: This figure shows a box plot of the distribution for the first principal component's scores. Visual comparison of the boxes and tails between the textures is a measure of equality of variance.

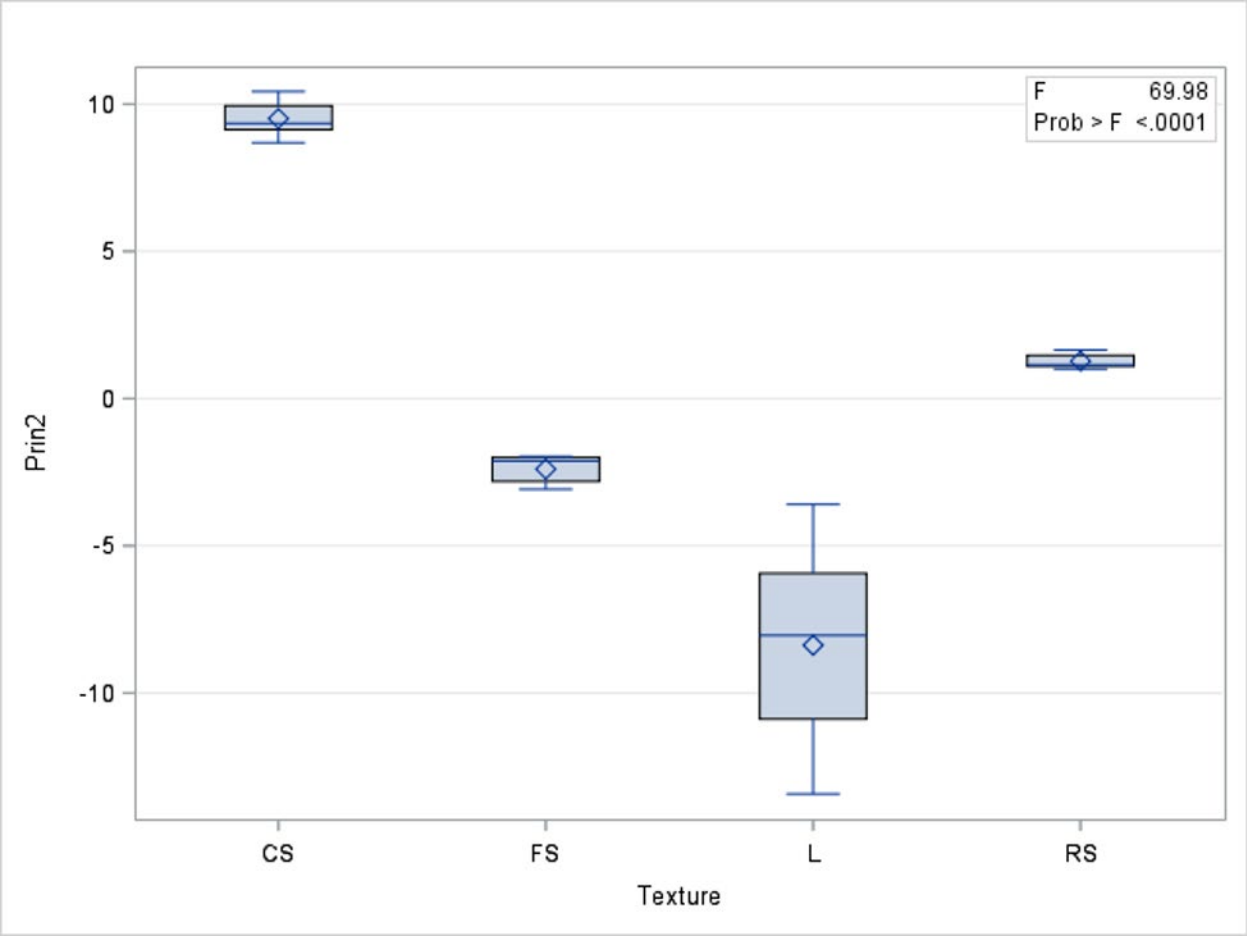

Figure 5.38: This figure shows a box plot of the distribution for the second principal component's scores. Visual comparison of the boxes and tails between the textures is a measure of equality of variance.

Due to the violation in ANOVA model assumptions, the Welch's variance-weighted one-way ANOVA was used. This alternative analysis is robust to violation of unequal variance assumptions (Welch, 1951). The results of this analysis show the null hypothesis that the mean value is the same for all texture groups is rejected at an α of 0.01 for both PC1 and PC2. Both p-values were reported at <0.001. Post-hoc evaluation was completed using the Games-Howell method which is uniquely suited for the violation in assumptions of this model (Games & Howell, 1976). This method revealed at an α of 0.05 that every texture mean value separates with relation to every

differing texture mean value for both PC1 and PC2. A clear depiction of this conclusion and the corresponding p-values are shown in Table 5.12 and 5.13 for PC1 and PC2 respectively.

Table 5.12: This table shows a statistical summary of the post-hoc evaluation using the Games-Howell method for PC1. The textures in the first two columns are declared different if the adjusted p-value is below the acceptable α.

Texture	Texture	Estimate	Standard Error	DF	t Value	Pr > |t|	Adj P
CS	FS	-19.1915	0.6863	16	-27.97	<.0001	<.0001
CS	L	2.7396	0.6863	16	3.99	0.001	0.0052
CS	RS	-16.8058	0.6863	16	-24.49	<.0001	<.0001
FS	L	21.9311	0.6863	16	31.96	<.0001	<.0001
FS	RS	2.3856	0.6863	16	3.48	0.0031	0.0148
L	RS	-19.5455	0.6863	16	-28.48	<.0001	<.0001

Table 5.13: This table shows a statistical summary of the post-hoc evaluation using the Games-Howell method for PC2. The textures in the first two columns are declared different if the adjusted p-value is below the acceptable α.

Texture	Texture	Estimate	Standard Error	DF	t Value	Pr > |t|	Adj P
CS	FS	11.904	1.2647	16	9.41	<.0001	<.0001
CS	L	17.8835	1.2647	16	14.14	<.0001	<.0001
CS	RS	8.2367	1.2647	16	6.51	<.0001	<.0001
FS	L	5.9795	1.2647	16	4.73	0.0002	0.0012
FS	RS	-3.6673	1.2647	16	-2.9	0.0104	0.0464
L	RS	-9.6468	1.2647	16	-7.63	<.0001	<.0001

Chapter 6 : Conclusions

An acoustic emission sensing wedge (AESW) was fabricated and used for on-the-go testing of soil. It was hypothesized that the acoustic data would show correlation with soil physical properties. Evaluation took place in the field, as well as in controlled outdoor and indoor experiments. To facilitate experimentation, outdoor and indoor soil bins were constructed. The acoustic data were analyzed for correlation with speed of the implement, compaction, and soil texture.

Testing in field conditions took place in a research plot treated with varying machine parameters and tillage methods. The first experiment aimed to find an effect of implement speed on the voltage vs. time series data. After analysis of several parameters, an R^2 of 0.79 was found between the speed of the implement and the mean of the absolute value of the sensed voltage. In addition, in a field setting, an experiment to determine the effect of compaction on the signal took place. Results showed that at an α of 0.01 there existed a difference in the median signal energy between a loam soil, which had high compaction levels, versus that of an identical soil with low compaction. The signal to noise ratio was also investigated after field experiments. A 17-25 dB signal energy gain between the measurements taken at idle and low implement speed versus those taken with the wedge in the soil was found.

The next set of experiments took place in soil bins installed both outdoors and indoors. One texture of sand was measured outdoors before inclement weather moved work inside. The inside bin was used to measure two additional soil textures. Based upon the data from varying textures, it was hypothesized that the number of acoustic emission counts may vary both with soil texture and compaction. An index was created to represent the peak levels of variability in the counts and the acoustic emission counts index score between textures and compaction levels were evaluated.

It was found at an α of 0.01, that Fairmount sand and river sand textures displayed a significant difference in median levels of the count index. However, previous literature and frequency domain analysis indicates although AE counts may be correlated with texture the root cause of the counts is not particle size. A relationship between the bulk density and AE count index was evaluated in and, at an α of 0.05, indicated there was no difference in the median for a loam soil. The data were also analyzed to determine whether a meaningful difference in the fractal dimension of the time series existed. It was observed that at nearly all scales the fractal dimension remained 1, which represents no additional dimensionality compared to a straight line.

Initial frequency domain analysis using visual inspection revealed little difference between the spectra of the four different textures. Due to this, advanced techniques such as wavelet analysis and moving average Fourier transforms were used to investigate the spectra as functions of time. This investigation revealed that the acoustic emission counts in the time series were causing spikes in the level of magnitude of the frequency spectrum. Analysis of the wavelet coherence between opposing textures and replications of the same textures revealed that the waveforms exhibit very little coherence as a function of time.

The average voltage, acoustic emission counts, and signal energy will have an effect on the magnitude of the frequency spectrum as they represent changes in voltage. To classify the texture based on the frequency spectrum, the effect of this increase, which was correlated with compaction, must be factored out. The z-score normalization method was used on the Welch's PSD to negate the compaction effect.

The Welch's PSD and z-scores were then used in a principal component analysis where 1000 points of the frequency spectrum were treated as independent variables of 5 replications for 4 textures. The PCA with the Welch's PSD revealed poor separation of the textures and low levels

of self-similarity between the replications. Using the z-score method, high levels of spatial separation were found among the different textures. The sand textures displayed high levels of self-similarity and loam exhibited moderate levels. Analysis of variance was conducted using the Welch correction on the top 200 loadings from the PCA using the z-score method. Following the ANOVA post-hoc evaluation using the Games-Howell method was completed. The results show that, at an α of 0.05, all textures are separable with respect to each other texture in both principal components.

These conclusions indicate the signal from the AESW is subject to a multifactor influence. The signal is sensitive to both the force acting on the AESW while being drawn through soil and the texture of the soil. Despite this multi-sensitivity, the implement speed, compaction, and soil texture may be found using different aspects of the signal.

To further this work, sampling should take place in fields with varying soil textures. The experiments developed for the furthering of the data collection should aim to characterize the measurements in varying textures with respect to moisture and force applied to the AESW as it is drawn through the soil. This should include the addition of sensors to measure the moisture and force in an on-the-go capacity. Investigation should also take place into the root cause of the AE counts and how their added information allows for classification. From these data, a machine learning algorithm may be trained to predict the texture given the signal from the AESW and additional sensors.

This thesis demonstrated that the signal from the AESW is sensitive to multiple aspects of the physical properties of the soil. Due to this multi-sensitivity, instead of attempting to decompose the elements of the signal, it is also suggested studies should also be conducted to determine if a correlation exists between the signal and the yield level. From this, a framework may be developed

to optimize the productivity of the soil given the signal from the AESW and other high spatial resolution soil measurements such as organic matter, cation exchange capacity, pH, etc. This data driven optimization would enable development of management models with more robust recommendations than are currently available. The enhancements will provide a step in the direction of sustainability and simultaneously increase profit for farmers.

References

Adamchuk, V., Skotnikov, A., Speichinger, J., & Kocher, M. (2004). Development of an Instrumented Deep-Tillage Implement for Sensing of Soil Mechanical Resistance. *Transactions of the ASAE*, *47*(2002), 1913–1920. Retrieved from http://digitalcommons.unl.edu/biosysengfacpub/163/

Adamo, F., Andria, G., Attivissimo, F., & Giaquinto, N. (2004). An acoustic method for soil moisture measurement. *IEEE Transactions on Instrumentation and Measurement*, *53*(4), 891–898. https://doi.org/10.1109/TIM.2004.831126

American Soceity for Testing and Materials. (2018). *Standard Guide for Mounting Piezoelectric Acoustic Emission Sensors* (No. ASTM E650/E650M − 17). West Conshohocken, PA. https://doi.org/10.1520/E0650-17.2

American Society of Agricultural and Biological Engineers; (2013). *Procedures for Using and Reporting Data Obtained with the Soil Cone Penetrometer* (No. ASAE EP542). St. Joseph, MI.

American Society of Agricultural and Biological Engineers. (2013). *Soil Cone Penetrometer* (No. ASAE S313.3). St. Joseph, MI.

American Society of Agricultural and Biological Engineers. (2014). *Agricultural wheeled tractors — Rear-mounted three-point linkage — Categories 1N, 1, 2N, 2, 3N, 3, 4N and 4* (No. ANSI/ASABE AD730). St. Joseph, Ml.

Andrade, S., Upadhyaya, S., Jenkins, B., Plouffe, C., & Poutre, B. (2004). Field evaluation of the improved version of the UCDavis compaction profile sensor (UCD-CPS). *Transactions of the American Society of Agricultural Engineers*, *0300*(04).

Brady, N., & Weil, R. (2004). *Elements of the Nature and Properties of Soils* (4th ed.). Upper

Saddle River: Pearson Education Ltd.

Brown, M., & Forsythe, A. (1974). Robust Tests for the Equality of Variances. *Journal of the American Statistical Association*, *69*(346), 346–367. https://doi.org/https://doi.org/10.1080/01621459.1974.10482955

Brutsaert, W. (1964). The Propagation of Elastic Waves in Unconsolidated Unsaturated Granular Mediums. *JOURNAL OF GEOPHYSICAL RESEARCH*, *69*(2).

Chan, K. (2017). *Understanding Signal to Noise Ratio and Noise Spectral Density in High Speed Data Converters*.

Chang, H.-W., Chang, T.-H., Nguyen, V.-T., & Wang, C.-W. (2010). Determination of Interfaces in Soil Layers By Sound Wave Analysis With Cone Penetration Tests. *Journal of Marine Science and Technology-Taiwan*, *18*(5), 664–673.

Chiann, C., & Morettin, P. (1998). A wavelet analysis for time series. *Journal of Nonparametric Statistics*, *10*(1), 1–46. https://doi.org/10.1080/10485259808832752

Chui, C. (1992). *Acoustic Signal Compression with Wavelet Packets*. San Diego: Academic Press, Inc. https://doi.org/10.1016/b978-0-12-174590-5.50026-5

Church, R. M. (1979). How to look at data: A review of John W. Tukey's Exploratory Data Analysis. *Journal of the Experimental Analysis of Behavior*, *31*(3), 433–440. https://doi.org/10.1901/jeab.1979.31-433

Das, B. (2002). *Soil Mechanics Laboratory Manual* (6th ed.). New York, New York: Oxford University Press.

Das, B., & Sobhan, K. (2009). *Principles of Geotechnical Engineering*. (H. Gowans, Ed.) (8th ed.). Stamford: Cengage Learning.

Davis, H. (1989). *Fourier Series and Orthogonal Functions*. New York, New York: Dover

Publications, Inc.

Dinkins, C., Jones, C., & Olson-Rutz, K. (2017). *Soil Sampling Strategies*. Bozeman.

Games, P., & Howell, J. (1976). PAIRWISE MULTIPLE COMPARISON PROCEDURES WITH UNEQUAL N's AND/OR VARIANCES: A MONTE CARLO STUDY. *Journal of Educational Statistics*, *1*(2), 113–125.

García-gaines, R., & Frankenstein, S. (2015). *USCS and the USDA Soil Classification System*.

Gonzato, G., Mulargia, F., & Marzocchi, W. (1998). Practical application of fractal analysis: Problems and solutions. *Geophysical Journal International*, *132*(2), 275–282. https://doi.org/10.1046/j.1365-246x.1998.00461.x

Grift, T. ;, Tekeste, M., & Raper, R. (2005). ACOUSTIC COMPACTION LAYER DETECTION. *Transactions of the ASAE*, *48*(5), 1–8.

Hall, H. E., & Raper, R. L. (2005). DEVELOPMENT AND CONCEPT EVALUATION OF AN ON-THE-GO SOIL STRENGTH MEASUREMENT SYSTEM. *Transactions of the ASAE*, *48*(2), 469–477.

Hemmat, A., Rahnama, T., & Vahabi, Z. (2014). A horizontal multiple-tip penetrometer for on-the-go soil mechanical resistance and acoustic failure mode detection. *Soil and Tillage Research*, *138*, 413–415. https://doi.org/10.1016/j.still.2013.12.003

Horowitz, P., & Winfield, H. (2015). *Art of Electronics* (3rd ed., Vol. 25). New York: Cambridge University Press.

Houlsby, G. T., & Ruck, B. M. (1998). *Interpretation of Signals from an Acoustic Cone Penetrometer*. (P. Robertson & P. Mayne, Eds.), *Geotechnical Site Characterization*. Balkema: A.A. Balkema Publishers.

Johnson, D. (1998). *Applied Multivariate Methods for Data Analysts*. (C. Crockett, Ed.). Pacific

Grove: b.

Kirham, M. B. (2014). *Principles of Soil and Plant Water Relations* (Second). Kidlington: Elsevier Inc. https://doi.org/10.1016/B978-0-12-420022-7.00008-2

Kruskal, W., & Wallis, A. (1952). Use of ranks in one-criterion variance analysis. *Journal of the American Statistical Association*, *47*(260), 583–621. https://doi.org/10.1080/01621459.1952.10483441

Lathi, B. (1998). *Modern Digital and Analog Communication Systems* (Third). Oxford: Oxford University Press.

Liu, C., & Evett, J. (1997). *Soil Properties - Testing, Testing, Measurement, and Evaluation* (3rd ed.). Upper Saddle River: Inc, Prentice-Hall.

Lu, Z., Hickey, C. J., & Sabatier, J. M. (2004). Effects of Compaction on the Acoustic Velocity in Soils. *Soil Science Society of America Journal*, *68*(1), 7. https://doi.org/10.2136/sssaj2004.0007

Lui, W., Gaulteny, L. D., & Morgan, M. (1993). Soil Texture Detection Using Acoustic Methods. In *Transactions of the ASAE* (pp. 1–14). Spokane.

Marks II, R. (1993). *Advanced Topics in Shannon Sampling and Interpolation Theory*. New York, New York: Springer-Verlag.

Meisami-asl, E., Sharifi, A., Mobli, H., Eyvani, A., & Alimardani, R. (2013). On-site measurement of soil moisture content using an acoustic system. *Agricultural Engineering International: CIGR Journal*, *15*(4), 1–8. Retrieved from http://cigrjournal.org/index.php/Ejounral/article/view/2571

Naderi-Boldaji, M., Tekeste, M. Z., Nordstorm, R. A., Barnard, D. J., & Birrell, S. (2018). A mechanical-dielectric-high frequency acoustic sensor fusion for soil physical

characterization. *Computers and Electronics in Agriculture*, *156*(December 2017), 10–23. https://doi.org/10.1016/j.compag.2018.11.006

National Resource Conservation Service. (2012). *Geology National Engineering Handbook*.

Olson, R., & Lai, J. (2004). *Direct Shear Testing*.

Sharma, R., & Gupta, A. (2010). Continuous wave acoustic method for determination of moisture content in agricultural soil. *Computers and Electronics in Agriculture*, *73*(2), 105–111. https://doi.org/10.1016/j.compag.2010.06.002

Shin, H., Watts, C. W., Whalley, W., Attenborough, K., & Taherzadeh, S. (2017). Non-invasive estimation of the depth profile of soil strength with acoustic-to-seismic coupling measurement in the presence of crops. *European Journal of Soil Science*, *68*(5), 758–768. https://doi.org/10.1111/ejss.12462

Solomon Jr., O. (1991). *PSD computations using Welch's method*. Albuquerque. https://doi.org/10.2172/5688766

Sullivan, M. (2010). *Statistics - Informed Decisions Using Data*. (C. Crockett, Ed.) (Third). Upper Saddle River: Brooks/Cole Publishing Company.

Tate, B. L. (2016). *SOIL TEXTURE DETERMINATION BY AN ACOUSTIC CONE PENETROMETER METHOD*. University of Illinois at Urbana-Champaign.

Topp, G., & Davis, J. (1985). Measurement of Soil Water Content using Time-domain Reflectometry (TDR): *Soil Science Society of America Journal*, *48*, 19–24. https://doi.org/10.2136/sssaj1985.03615995004900010003x

Towner, M. C., Zarnecki, J. C., & Marcou, G. (2000). THE ACOUSTIC SIGNALS GENERATED DURING PENETROMETER IMPACTS INTO GRANULAR MATERIALS: IMPLICATIONS FOR HUYGENS. In *Lunar and Planetary Science XXXI*. Lunar and

Planetary Institute.

Tringale, P. (1983). *Soil identification in-situ using and acoustic cone penetrometer*. University of California, Berkeley.

United Nations Food and Agriculture Organization. (2009). *How to Feed the World in 2050*. Rome. Retrieved from http://www.fao.org/fileadmin/templates/wsfs/docs/expert_paper/How_to_Feed_the_World_in_2050.pdf

United Nations Food and Agriculture Organization. (2015). *Status of the World's Soil Resources*.

Villet, W., Mitchell, C., & Tringale, P. (1981). *Acoustic Emissions in Geotechnical Engineering Practice*. (V. Drnevich & R. Gray, Eds.). Philadelphia: American Society for Testing and Materials. Retrieved from http://books.google.com/books?hl=en&lr=&id=AnsEk6ES9mIC&oi=fnd&pg=PA1&dq=Acoustic+emissions+in+geotechnical+engineering+practice:+a+symposium&ots=IxEYxXk3tc&sig=SiAIEat6ZsoOtvjbiQmSm-mpt3I

Welch, B. (1951). On the Comparison of Several Mean Values: An Alternative Approach. *Biometrika*, *38*(3/4), 330–336. https://doi.org/10.2307/2332579

Wesley, L. (2010). *Fundamentals of Soil Mechanics for Sedimentary and Residual Soils*. Hoboken: John Wiley and Sons Inc.

Appendix A: Acoustic Emission Sensing Wedge Engineering Drawings

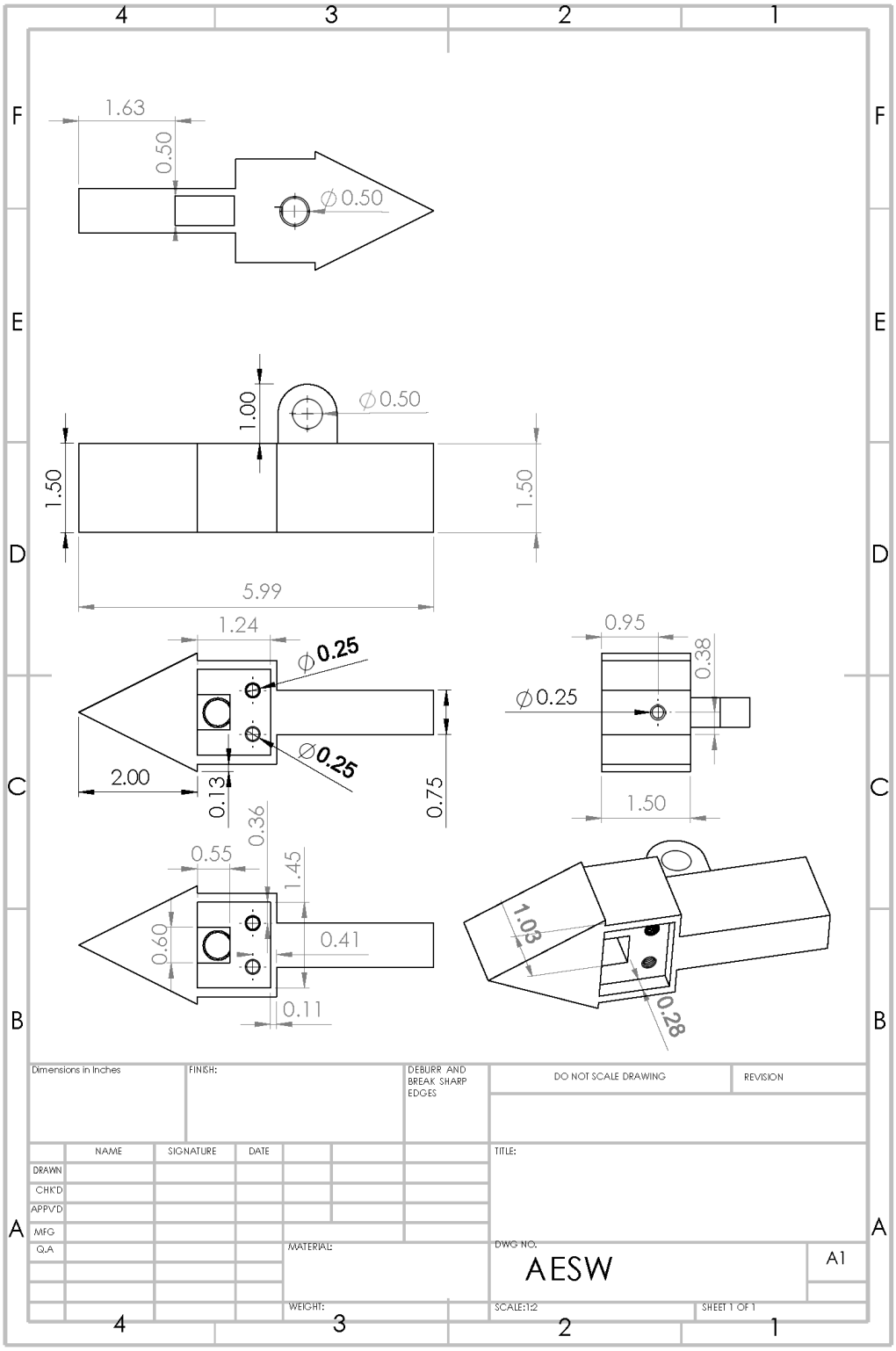

Figure A.1: This figure shows an engineering drawing of the AESW.

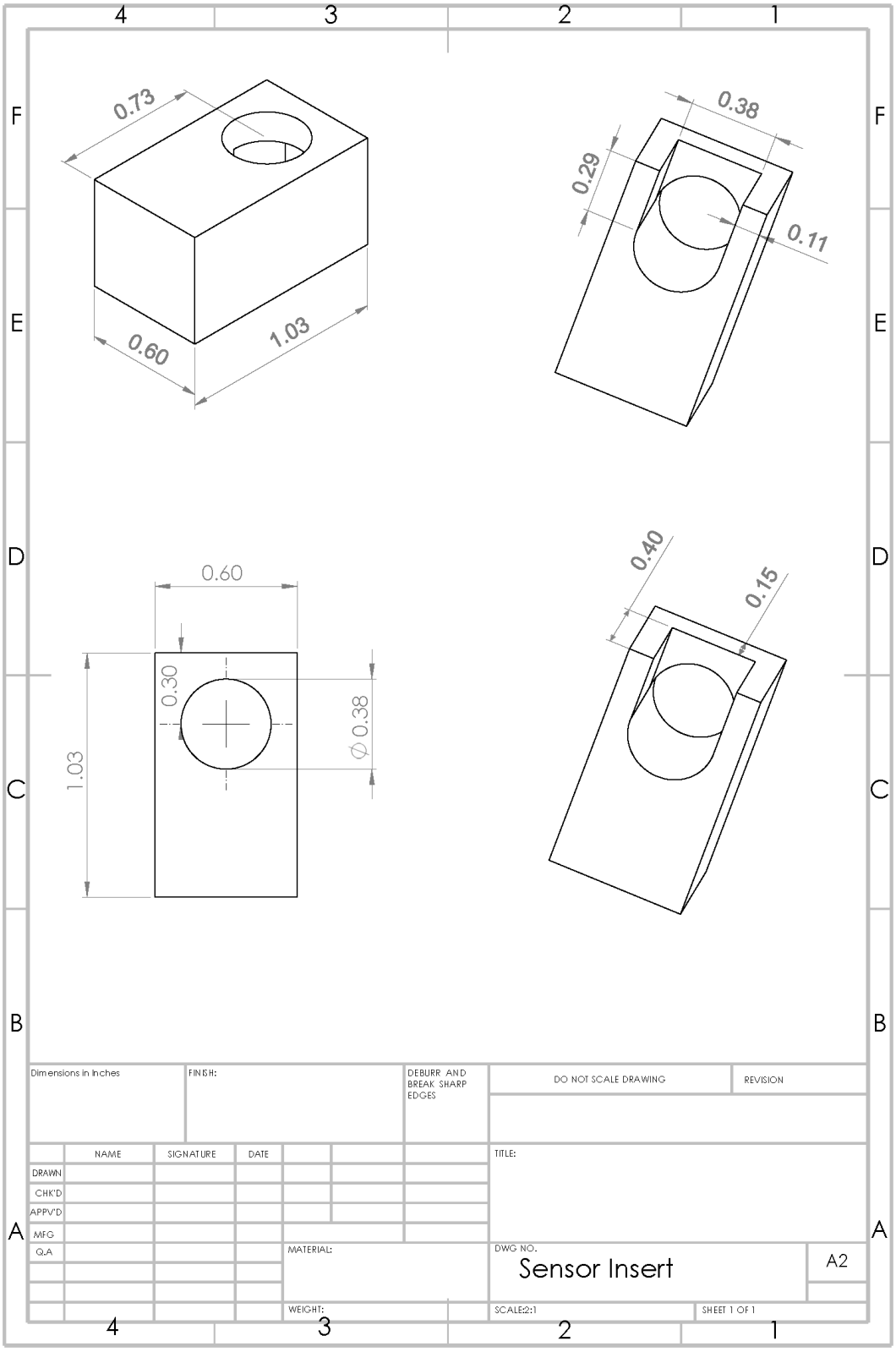

Figure A.2: This figure shows an engineering drawing of the sensor insert for the AESW.

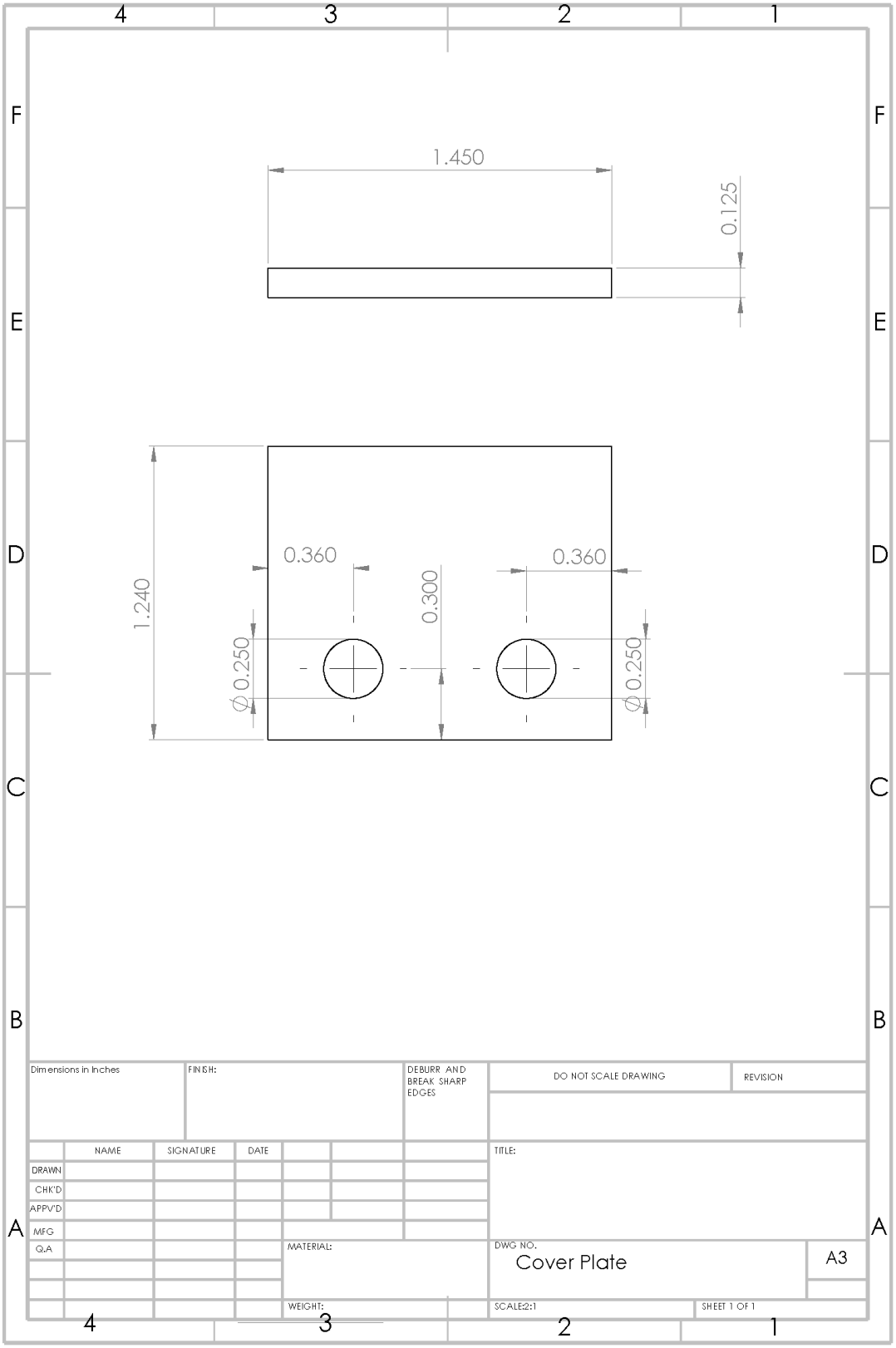

Figure A.3: This figure shows an engineering drawing of the cover plate for the AESW.

Appendix B: Frequency Domain Signal-to-Noise Plots

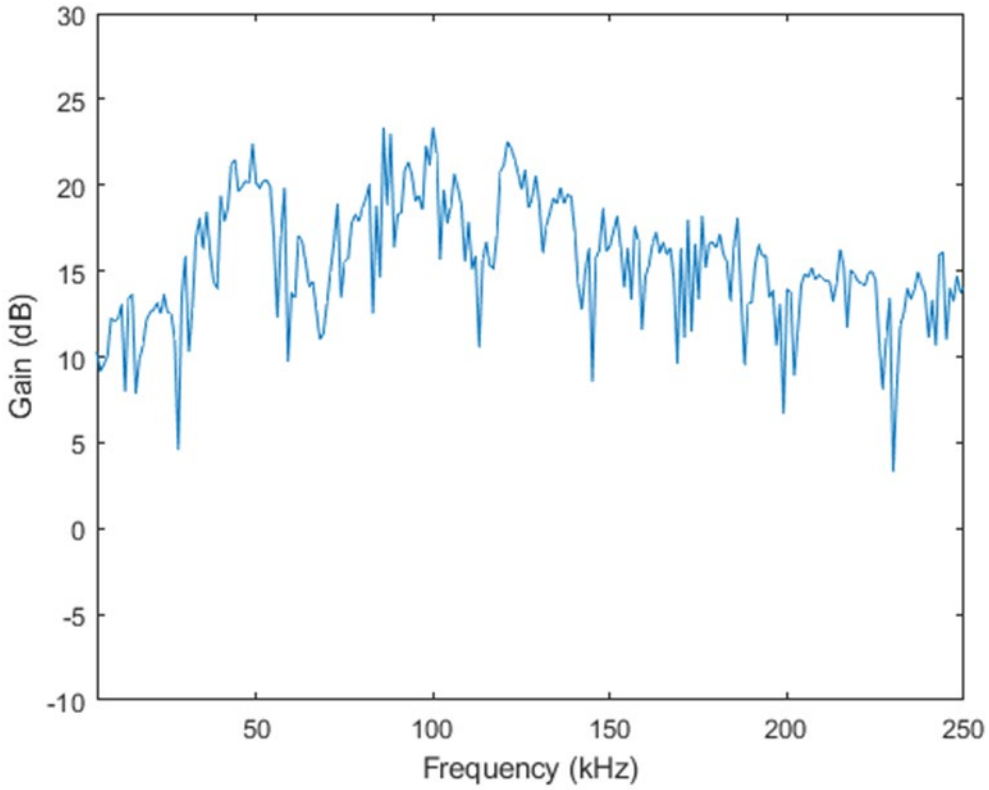

Figure B.1: This figure shows the power spectrum signal-to-noise ratio across the frequency domain between the high compaction run and the dynamic calibration.

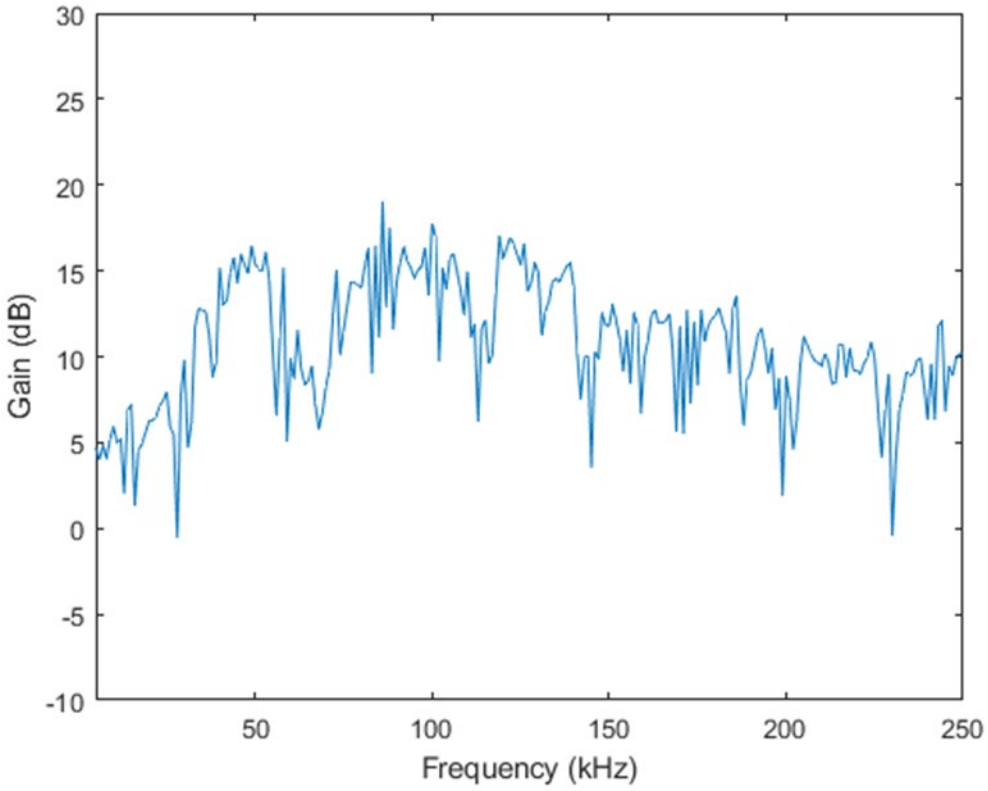

Figure B.2: This figure shows the power spectrum signal-to-noise ratio across the frequency domain between the low compaction run and the dynamic calibration.

Appendix C: Acoustic Emission Counts Index Program

```
%%= AECI Program =%%
%%= Brendan Kuhns (3/15/19) =%%

%%============== Variable Declaration =============%%

i=1;
j=1;
Data = table2array(Data);
SQRTSTORE = zeros([1e6 1]);
Time = .25;
Rate = (1e6);

%%============== Summary Statistics =============%%

SQRT = sqrt(Data.*Data); % Turn B positive
MEAN = mean(SQRT);
STD1 = std(SQRT); % Find the standard deviation of B
MAX = max(SQRT)/STD1; % Finds how many STD's furthest point is from the mean
FINALMAX = ceil(MAX); % Rounds up to next integer
TOTALHITS = zeros(FINALMAX,2); % Create a vector for the total hits per
standard deviation

%%============== Find # of STD's For Each Point =============%%

for i=1:FINALMAX % Start a for loop from 1 to the largest standard deviation
containing a hit

    if i<=FINALMAX % Create a separation between 1 STD range
        STDLEVEL = (STD1 * i);
        STDLEVEL2 = (STD1 * (i + 1));

        for j=1:(Rate*Time) %% Check entire series see if point in range
            if SQRT(j,:)>=STDLEVEL & SQRT(j,:) <=STDLEVEL2
                SQRTSTORE(j,:) = 1; % If yes assign 1
                j = j+1;
            else
                SQRTSTORE(j,:) = -1; % If no assign -1
                j = j + 1;
            end
        end
        SIGN = sign(SQRTSTORE); % Sign everything - or +
        HITS = find(SIGN>0); % Count number of +'s
        TOTALHITS(i,:) = [i,length(HITS)]; % Store number of +'s
        i = i+1; % Go to next STD range

    else
        i = i+1; % When above largest STD kick out of loop

    end

end
```

```
TOPLIST = sort(SQRT,'descend'); % Sort voltage largest to smallest
TOPLISTSTD = TOPLIST(1:10)/STD1; % Take top 10 and find STD's from mean
AECI = mean(TOPLISTSTD(:)) % Calculate mean and find score
```

Appendix D: Moving Average FFT Program

```
%%= Moving Average FFT Program =%%
%%= Brendan Kuhns (3/15/19) =%%

%============== Variable Entry ==============%%

MFFTDATA = DATASET; % Time data to be analyzed place on right on in 1C array
Ss = 48e3; % Enter the sampling frequency
BLOCKSZ = 1000; % Enter block size
OVERLAP = 250; % one sided overlap, must be no more then 1/2 BLOCKSZ

%%============== Variable Calculations ==============%%

Sp = 1/Ss; % Sampling period
SL = length(MFFTDATA); % Determine # of measurements
BLOCKNUMB = floor((SL/BLOCKSZ)); % Calculate the # of blocks
MAXT = ((-OVERLAP+(BLOCKSZ*BLOCKNUMB))*Sp); % Last time block for x limit

j=1; % loop counter
i=1; % loop counter

%%============== Initialize Matrices by FFT Length ==============%%

FFTCHECK = 2^nextpow2(BLOCKSZ)/2;

runtimematrix = zeros([FFTCHECK BLOCKNUMB]); % Create Matrices
mfftfreq = zeros([FFTCHECK BLOCKNUMB]); % Create Matrices
mfftmag = zeros([FFTCHECK BLOCKNUMB]); % Create Matrices
%%============== FFT Loop ==============%%

for i=1:BLOCKNUMB

D = MFFTDATA((((BLOCKSZ/2)*i)-OVERLAP):(((BLOCKSZ/2)*(i+1))+OVERLAP),1); %
Separate voltage into blocks
Sp = 1/Ss; % Sampling Period
Ddt=0:Sp:Sp-Sp;% Signal duration must match time used when data taken
Dfft=length(D); % Fourier transform using power 2
Dfft2 = 2^nextpow2(Dfft);
Dff=fft(D,Dfft2);
Dfff=Dff(1:Dfft2/2);
Dqfft=Ss*(0:Dfft2/2-1)/Dfft2;
DDqfft = transpose(Dqfft./1000);
DDfff = 10*log10((abs(Dfff).^2)); % Make magnitude logarithmic
mfftfreq(:,(i)) = DDqfft(:,1); % Store frequencies
mfftmag(:,(i)) = DDfff(:,1); % Store magnitudes
i=i+1;

end

%%============== Increment time according to FFT blocks ==============%%

for j=1:BLOCKNUMB
```

```
    runnumber = (((-OVERLAP)+(BLOCKSZ*j))*Sp);
    runtimematrix(:,j) = (runnumber);
    j+1;
end

%%============== Plot Moving Average FFT =============%%
figure
mesh(runtimematrix,mfftfreq,mfftmag);
colormap(jet);
colorbar;
xlabel('Time (s)')
xlim([0 MAXT])
ylabel('Frequency (kHz)');
zlabel('Magnitude (dB)');
title('Moving Average FFT);
```

Appendix E: Frequency Domain Analysis Plots

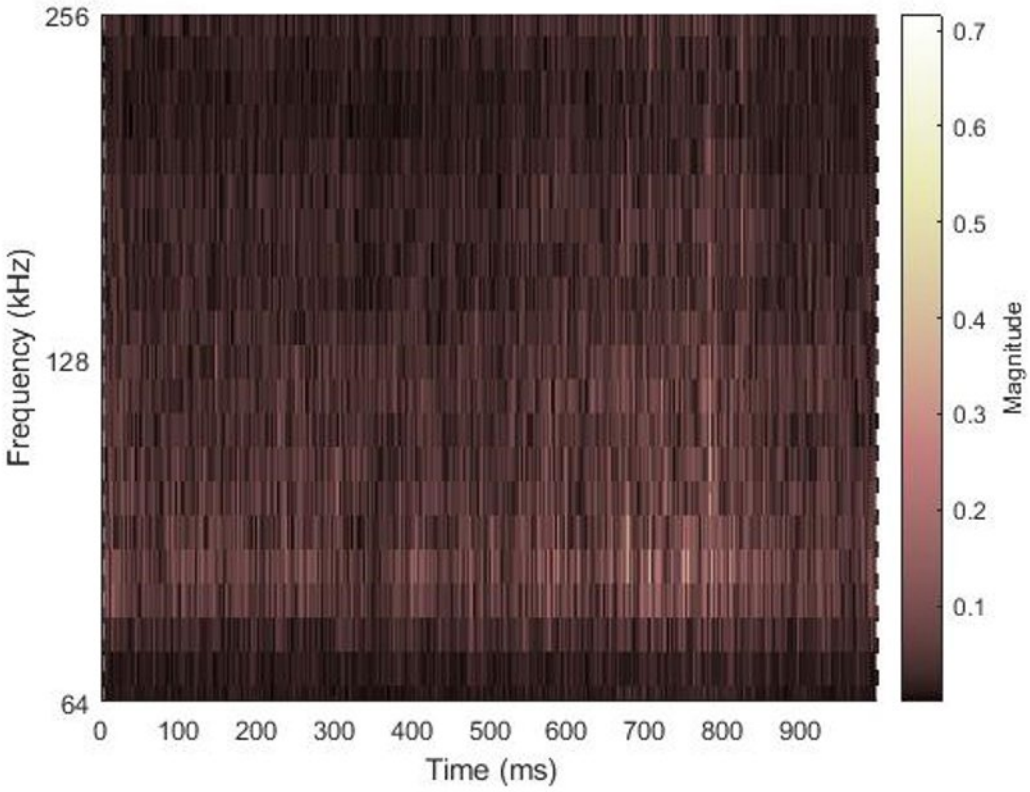

Figure E.1: The magnitude scaleogram shown used bump wavelets to characterize the frequency spectrum as a function of time for data collected in river sand.

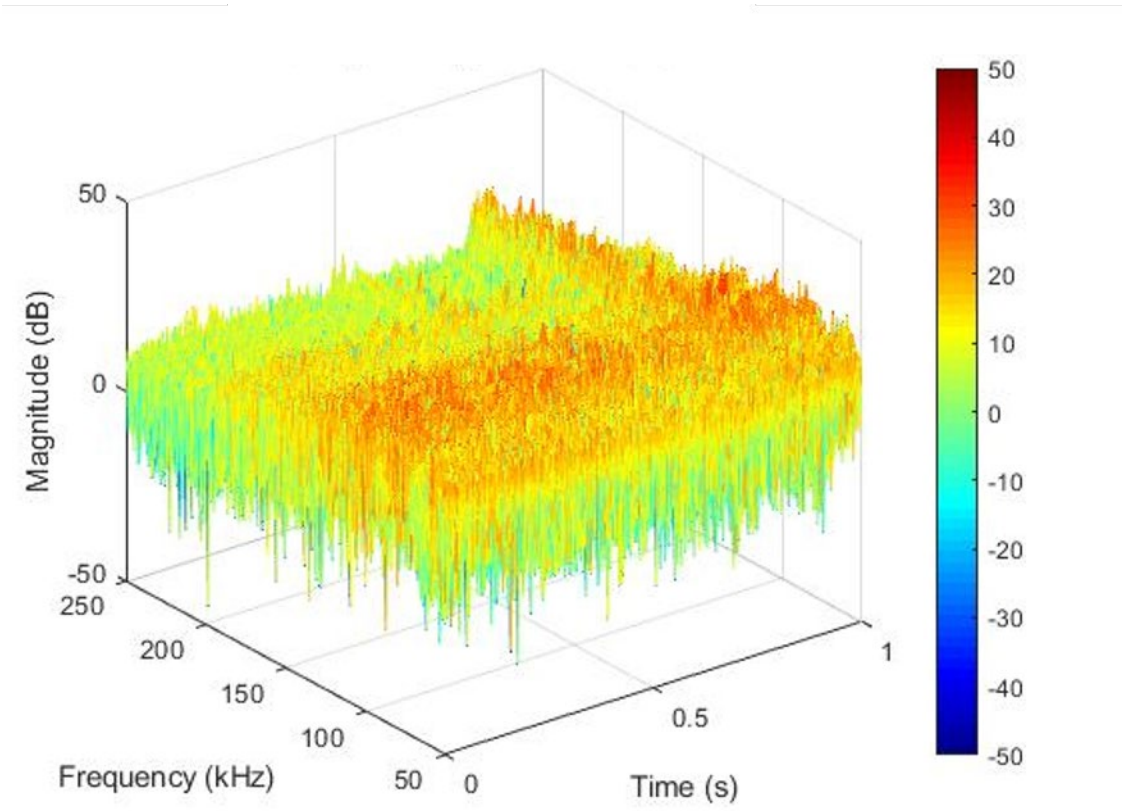

Figure E.2: Moving Average FFT of data taken in river sand. Similar to the magnitude scaleogram this allows for depiction of how the time series affects the frequency distribution.

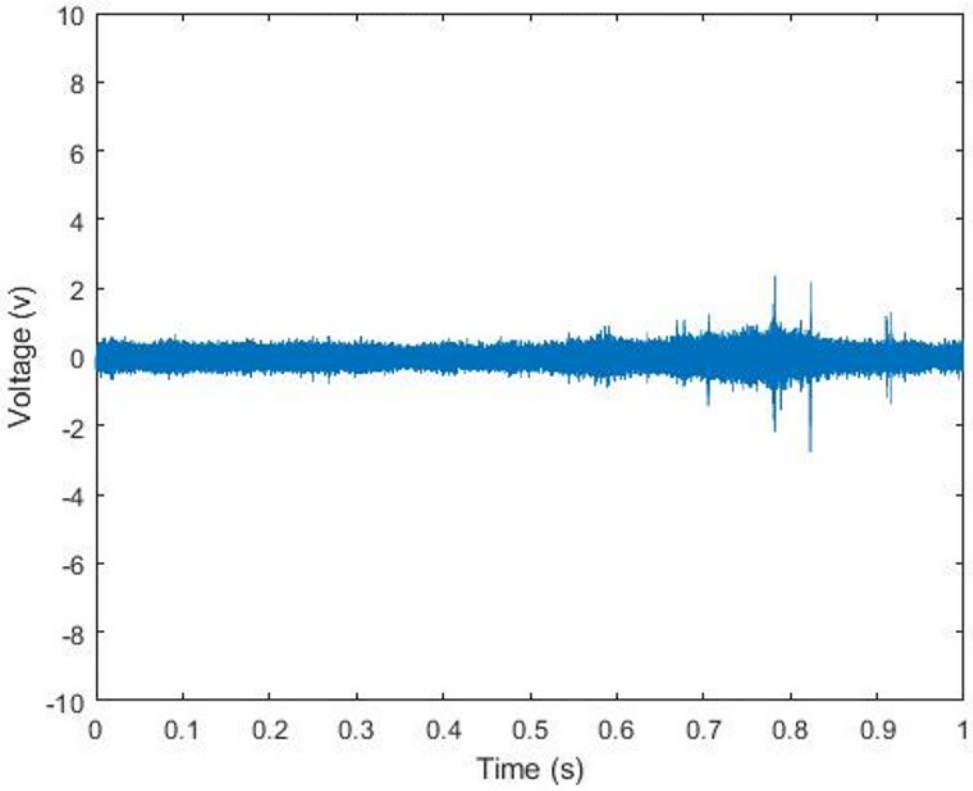

Figure E3: Voltage vs. time series of data collected in river sand for 1 second at 0.44 m/s.

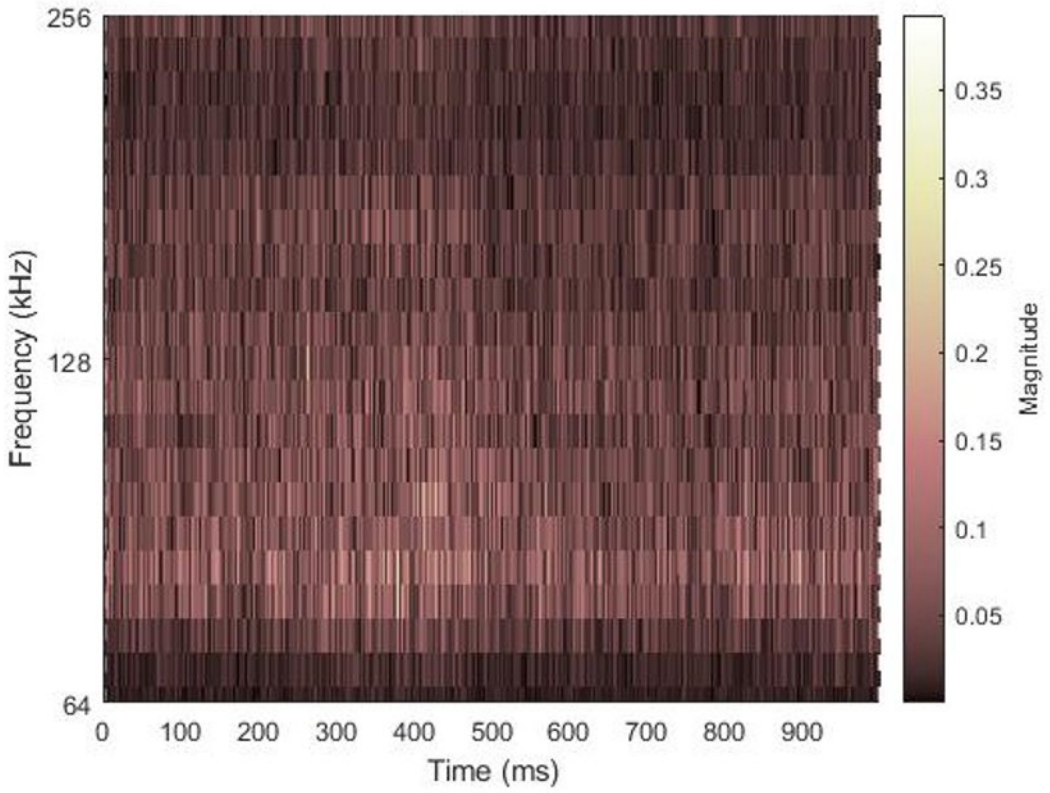

Figure E.4: The magnitude scaleogram shown used bump wavelets to characterize the frequency spectrum as a function of time for data collected in Fairmount sand.

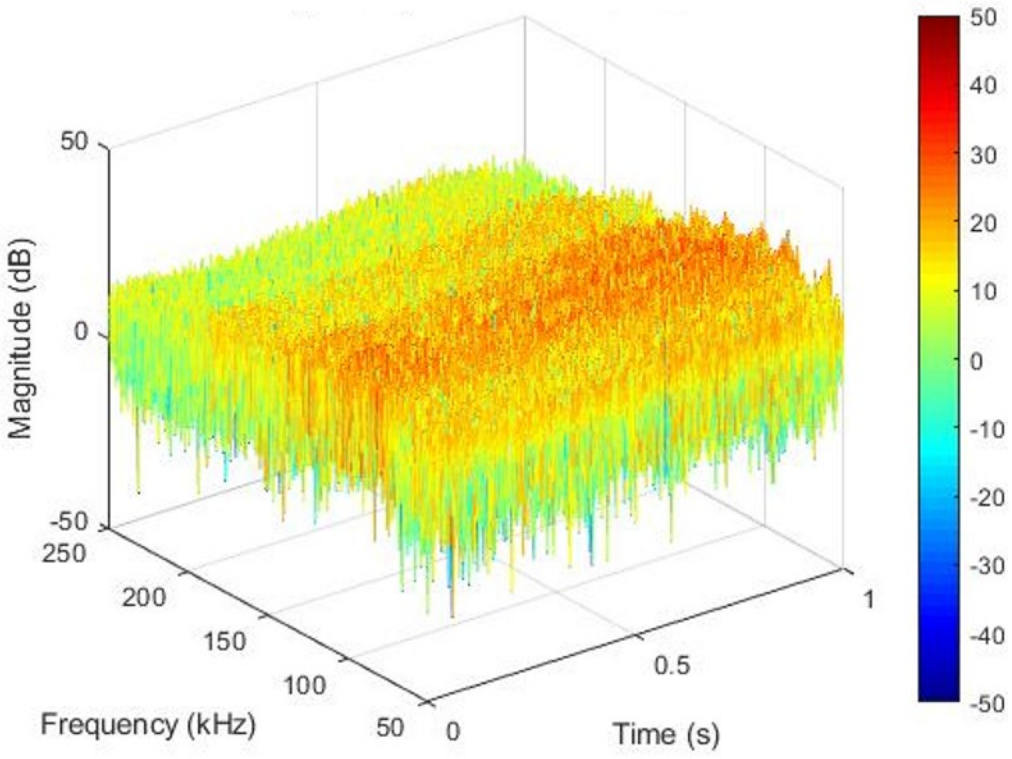

Figure E.5: Moving average FFT of data taken in Fairmount sand. Similar to the magnitude scaleogram this allows for depiction of how the time series affects the frequency distribution.

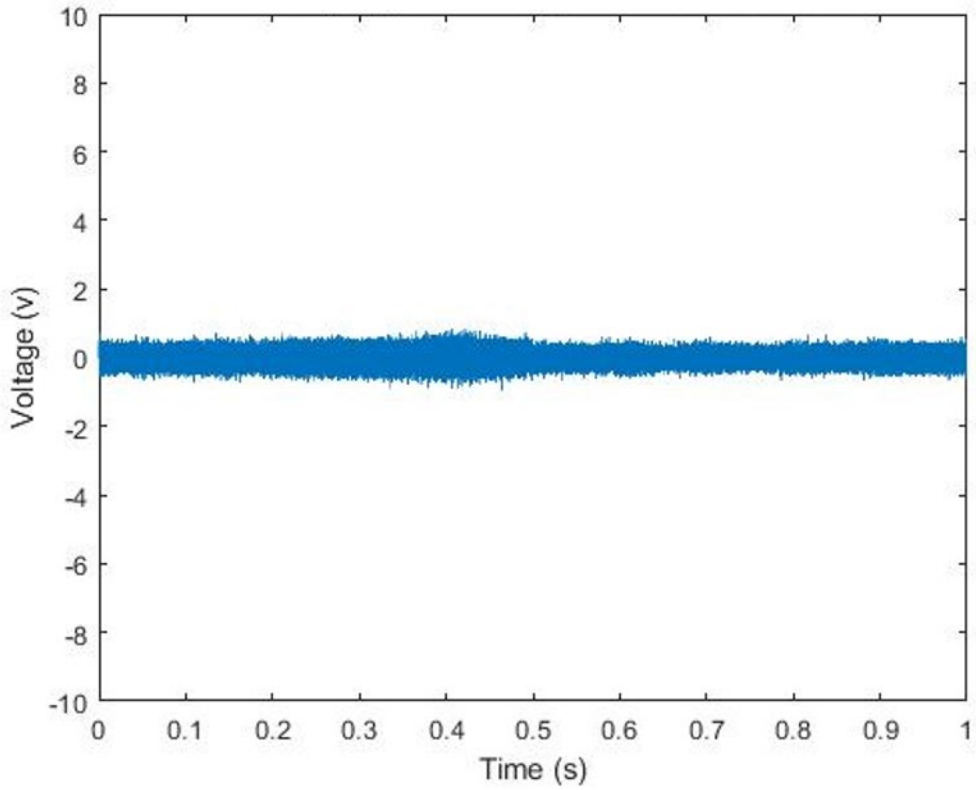

Figure E.6: Voltage vs. time series of data collected in Fairmount sand for 1 second at 0.44 m/s.